BOSTON UNIVERSITY

COLLEGE OF ENGINEERING

Dissertation

FREQUENCY-DOMAIN DIFFUSE OPTICAL SPECTROSCOPY FOR CARDIOVASCULAR AND RESPIRATORY APPLICATIONS

by

RAEEF ERIC ISTFAN

B.S., Boston University, 2012
M.S., Boston University, 2018

Submitted in partial fulfillment of the

requirements for the degree of

Doctor of Philosophy

2021

Approved by

First Reader

Darren M. Roblyer, Ph.D.
Associate Professor of Biomedical Engineering
Associate Professor of Electrical and Computer Engineering

Second Reader

Irving J. Bigio, Ph.D.
Professor of Biomedical Engineering
Professor of Electrical and Computer Engineering
Professor of Physics
Professor of Medicine

Third Reader

Sergio Fantini, Ph.D.
Professor of Biomedical Engineering
Tufts University

Fourth Reader

Katherine Yanhang Zhang, Ph.D.
Professor of Mechanical Engineering
Professor of Biomedical Engineering
Professor of Materials Science and Engineering

Fifth Reader

Cara E. Stepp, Ph.D.
Professor of Speech, Language, and Hearing Sciences
Professor of Biomedical Engineering
Professor of Otolaryngology – Head & Neck Surgery

DEDICATION

To all my friends and family.

ACKNOWLEDGMENTS

To Darren Roblyer, my advisor, for all of your guidance and support during the last decade. I have had the pleasure of joining the lab at its inception in 2012 and it was a pleasure to be able to witness the start of the lab and many of the various projects during the last 9 years in the lab. Thank you for taking me on first as a lab technician and then as a PhD student and most of all for helping me become both a better person and better scientist.

To Irving Bigio for all of your wisdom and support especially with all of your knowledge of the fundamental physics of optics.

To the rest of my committee for your valuable input and guidance into the project.

To Ousama A'amar for your valuable assistance in helping me understand engineering and instrumentation concepts.

To Eric Hazen and the BU Electronics Design Facility for all of your help designing, developing and troubleshooting the custom electronics that was the focal point of this dissertation.

To all of the collaborators that helped including Matthew Brenner, Sari Mahon, Tanya Burney, and David Mukai from the University of California, Irvine for your help with the

Rabbit Study (chapter 3) and Darlene Reid from the University of Toronto for your help with the inspiratory muscle project (chapter 4).

To all of the healthy volunteers for their time and patience helping me collect data.

To the BU BME community for fostering a good environment especially Christen Bailey and Allie Gustin.

To all of my fellow BOT Lab members and senior project groups, both past and present for all of your help and support. I would like to give special thanks to Matthew Applegate ad Carlos Gómez for helping directly with various parts of this dissertation.

To all of my fellow graduate students for all of your support and all of the great memories that were shared.

Most of all, to my family for your unconditional and unwavering support.

FREQUENCY-DOMAIN DIFFUSE OPTICAL SPECTROSCOPY FOR CARDIOVASCULAR AND RESPIRATORY APPLICATIONS

RAEEF ERIC ISTFAN

Boston University College of Engineering, 2021

Major Professor: Darren M. Roblyer, Ph.D., Associate Professor of Biomedical Engineering, Associate Professor of Electrical and Computer Engineering

ABSTRACT

Frequency Domain Diffuse Optical Spectroscopy (FD-DOS) is an emerging optical technique that uses near infrared light to probe the hemodynamics of biological tissue. Compared to more common Continuous Wave (CW) methods, FD-DOS uses light that is temporally modulated on the order of MHz to quantify the absorption and scattering of tissue. FD-DOS can also be used to obtain absolute concentration of tissue chromophores such as oxy- and deoxy-hemoglobin, which allow for quantitative measurements of tissue hemodynamics. This dissertation focuses on the evolution of our lab's custom digital FD-DOS as a platform for taking optical measurement of biological tissue for respiratory and cardiovascular applications. Several important instrumentation improvements will be reviewed that have enhanced the performance of the system while making it more portable and clinic ready. Two translational applications will be described in detail: 1) the use of high-speed FD-DOS for the non-invasive extraction of venous oxygen saturation (SvO_2) and 2) the use of FD-DOS to monitor the hemodynamics of the sternocleidomastoid (SCM) muscle towards the non-invasive monitoring of patients on mechanical ventilation. The custom FD-DOS system parameters were adjusted for each application, with a focus on

high speed to extract the cardiac signal for the SvO_2 project, and a focus on high SNR to measure the highly absorbing SCM. Measurements on healthy volunteers and rabbits were used to assess the feasibility of using FD-DOS for these applications. Finally, preliminary work was conducted to characterize a miniature FD-DOS source and detector with the goal of moving towards a wearable version of FD-DOS.

TABLE OF CONTENTS

LIST OF TABLES

LIST OF FIGURES

LIST OF ABBREVIATIONS

AC ..... Alternating Current

ADC ..... Analog to Digital Converter

APD ..... Avalanche Photodiode

BU ..... Boston University

CO ..... Cardiac Output

CS ..... Constant Scattering

CW ..... Constant Wave

DC ..... Direct Current (0 frequency)

DDS ..... Direct Digital Synthesizer

DOS ..... Diffuse Optical Spectroscopy

DPF ..... Differential Pathlength Factor

FD ..... Frequency Domain

FD-DOS ..... Frequency Domain Diffuse Optical Spectroscopy

FD-NIRS ..... Frequency Domain Near Infrared Spectroscopy

FFT ..... Fast-Fourier Transform

FPGA ..... Field-Programmable Gain Array

Hb ..... Hemoglobin

LUT ..... Look Up Table

Mb ..... Myoglobin

MV ..... Mechanical Ventilation

NIR ..... Near Infrared

NIRS ..... Near Infrared Spectroscopy

PAC ..... Pulmonary Artery Catheter

PCB ..... Printed Circuit Board

PhD ..... Doctor of Philosophy

PMT ..... Photomultiplier Tube

PPG ..... Photoplethysmography

RF ..... Radio Frequencies

SaO_2 ..... Arterial Oxygen Saturation

SCM ..... Sternocleidomastoid

SNR ..... Signal to Noise Ratio

SO_2 ..... Oxygen Saturation

SpO_2 ..... Peripheral (Pulse Oximeter) Oxygen Saturation

StO_2 ..... Tissue Oxygen Saturation

SvO_2 ..... Venous Oxygen Saturation

TD ..... Time Domain

TEC ..... Thermoelectric Cooler

VCSEL ..... Vertical Cavity Surface Emitting Laser

μ_a ..... Coefficient of Absorption

μ_s' ..... Reduced Coefficient of Scattering

CHAPTER 1: INTRODUCTION

1.1: Background

One of the main functions of the cardiovascular and respiratory systems is to transport oxygen throughout the body. Oxygen is primarily transported while bound to hemoglobin (Hb), a protein with 4 heme groups that binds up to 4 oxygen molecules and is a primary component in blood. Hb is an optically-active molecule with different absorption characteristics in visible and near infrared wavelengths depending on how much oxygen is bound to it. This property has led to the development of optical measurement systems to probe the oxygenation of different regions of the body. A major advantage of using light to measure tissue oxygenation is that it is non-invasive and therefore does not require drawing blood or taking tissue samples and can be performed continuously without harming the subject.

Over the past several decades, there have been many technologies and devices that have used light to extract oxygenation information from tissue. These devices range from pulse oximeters, which are used in clinical settings to determine peripheral oxygen saturation (SpO_2), a surrogate for arterial oxygen saturation (SaO_2), to more recently, wearable devices such as the Fitbit or Apple Watch which are used for personal use and fitness monitoring [1]–[3]. Many of these devices use Continuous Wave (CW) light and are unable to separate the effects of optical absorption from scattering, limiting the amount of information that can be determined. Frequency Domain Diffuse Optical Spectroscopy (FD-DOS) is a more complex technique that is able to isolate the effects of absorption and scattering, allowing the calculation of absolute concentrations of chromophores, which

enables more quantitative measurements of tissue hemodynamics. FD-DOS has been widely explored in applications in breast cancer [4]–[7], brain hemodynamics [8], and exercise physiology [9]. This work focuses on potential cardiovascular and respiratory applications, which are two lesser explored areas.

1.2: Structure of the Thesis

This thesis will be separated into four sections contained in chapters 2-5. Chapter 2 will focus on the evolution of the digital FD-DOS platform, which was the primary instrument used to take the following measurements. There are a number of considerations that needed to be taken into account when improving, iterating, and testing versions of the system, and these considerations will be discussed in this chapter. Chapters 3 and 4 will showcase two applications of the system: 1) non-invasive extraction of venous oxygen saturation and 2) monitoring the oxygenation of the sternocleidomastoid. In both chapters, I will discuss the instrumentation and specific design changes that were made for each application as well as the specific experiments that utilized the system. The final chapter will discuss preliminary testing that was done towards miniaturizing components of an FD-DOS system with an eventual goal of developing a completely wearable FD-DOS device.

1.3: Specific Aims

The Specific Aims of the project are as follows:

1. Improve and quantify the performance of a clinic ready high-speed FD-DOS system

1.1. Improve the FD-DOS system towards a high-speed clinic ready system

1.2. Integrate a large area detector for fiber coupled FD-DOS measurements

1.3. Characterize the performance of a clinic-ready FD-DOS system

2. Evaluate the feasibility of using FD-DOS for non-invasive venous oxygen saturation (SvO_2) measurements

2.1. Develop processing pipeline for fast FD-DOS measurements

2.2. Healthy Volunteer Study

2.3. Rabbit Study

3. Evaluate the feasibility of using FD-DOS for measurements on the sternocleidomastoid (SCM)

3.1. Demonstrate that FD-DOS measurements are sensitive to changes of SCM oxygenation in simulation

3.2. Measure changes in SCM oxygenation in healthy volunteers

CHAPTER 2: Improve and Quantify the Performance of a High-speed Clinic Ready FD-DOS System

2.1: Background

This chapter will focus on a technique called Diffuse Optical Spectroscopy (DOS). DOS is an emerging optical technique that uses red and near infrared light (600 -1000 nm) to measure the optical properties in localized tissue. As light travels through tissue, the photons may scatter (change direction) due to changes in refractive index between components of the tissue or get absorbed by molecules in the tissue and release heat. DOS measures light in the diffuse regime, which means that photons scatter multiple times before they reach a detector that is placed at least several millimeters away from the light source [10]. As a result, the detector collects only as small percentage of the photons emitted by the source. Figure 2-1 shows an example of a diffuse optical system illuminating a human finger.

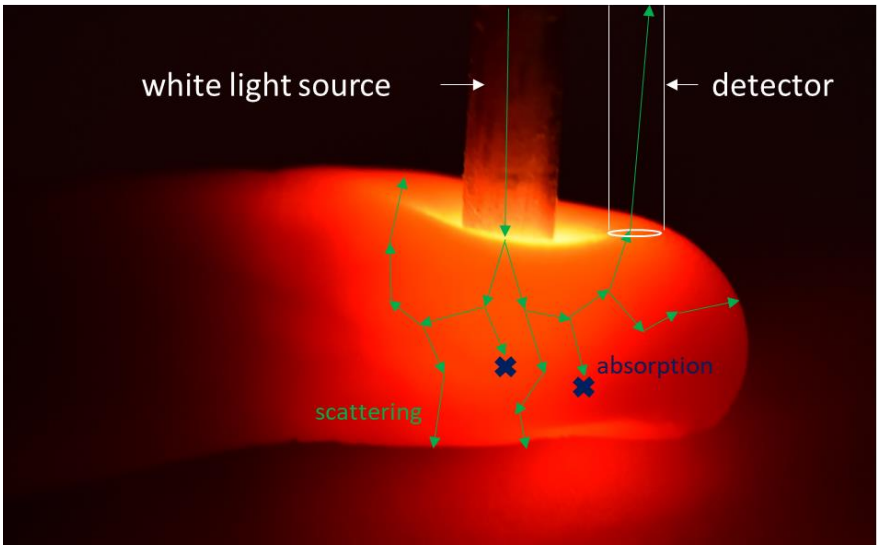

Figure 2-1. An example of light as it interacts with a finger. As light enters tissue, it is scattered in many directions and absorbed by molecules in the tissue. A small percentage of light is able to reach a detector place some distance away from the source

There are three branches of DOS that are currently under use and development: Frequency Domain (FD), Time Domain (TD), and Continuous Wave (CW) [11]. CW-DOS, also known as Near Infrared Spectroscopy (NIRS), uses a continuous source of light at several wavelengths to calculate changes in attenuation of light through tissue. CW-DOS is unable to isolate optical absorption and scattering and therefore only able to measure relative changes of chromophores rather than absolute concentrations [12]. CW-DOS is the least expensive and least complex of the three methods, and it is commonly used in research and medicine, with the most widespread example being the commercial pulse oximeter. TD and FD-DOS are able to isolate absorption and scattering and are therefore able to provide more information such as the absorption and scattering coefficient of the tissue, and consequently the absolute concentration of chromophores. Several research groups around the world have explored the use of both TD and FD-DOS for research and clinical applications. Our lab primarily develops and uses FD-DOS because unlike TD-DOS it does not require time gated detection, thus decreasing the overall complexity and cost of the system.

In FD-DOS, light is modulated in a sinusoidal manner in time, typically in the RF frequency range (50 MHz- 1 GHz) [11]. When light modulated in time travels through tissue, it can be modeled as a photon density wave, which is the time and space dependence of energy density (photons) in the medium [10]. As this wave travels through tissue, its amplitude is reduced and its phase is shifted (delayed) as compared to the source illumination. Both analytic and Monte-Carlo based models that relate amplitude and phase measurements to tissue optical properties are well described in the literature [13], [14]. A

commonly used analytic solution to the P1 approximation to the radiative transfer equation in semi-infinite homogenous medium is shown as a set of equations (equations 2-1 through 2-9). These equations relate the optical properties (coefficient of absorption, μ_a and the reduced coefficient of scattering, μ_s') to the changes in amplitude and phase (A_{att} and θ_{lag}) [13]. In equations 2-1 through 2-9, the parameters ρ and ω refer to source-detector separation and modulation frequency respectively, A_{ir} is the amplitude response of the instrument, and R_{eff} is the effective reflection coefficient, typically 0.431 and 0.493 for air-water and air-tissue interfaces respectively [13].

$$\theta_{lag}(\rho,\omega) = k_{imag}(\omega)r_0 - \arctan(\frac{IMAG}{REAL}) \quad \textbf{(2-1)}$$

$$A_{att}(\rho,\omega) = \frac{A_{ir}}{4\pi D}(REAL^2 + IMAG^2)^{1/2} \quad \textbf{(2-2)}$$

where,

$$REAL = \frac{\exp[-k_{real}(\omega)r_0]}{r_0} - \cos\left[k_{imag}(\omega)(r_{0b} - r_0)\right]\frac{\exp[-k_{real}(\omega)r_{ob}]}{r_{0b}} \quad \textbf{(2-3)}$$

$$IMAG = \sin[k_{imag}(\omega)(r_{0b} - r_0)]\frac{\exp[-k_{real}(\omega)r_{ob}]}{r_{0b}} \quad \textbf{(2-4)}$$

$$r_0 = [(\mu_s')^{-2} + \rho^2]^{1/2} \quad \textbf{(2-5)}$$

$$r_{0b} = \left[\left(\frac{4}{3\mu_s'}\frac{1+R_{eff}}{1-R_{eff}} + \frac{1}{\mu_s'}\right)^2 + \rho^2\right]^{1/2} \quad \textbf{(2-6)}$$

$$k_{real} = \sqrt{\frac{3}{2}\mu_a\mu_s'}\left\{\left[1 + \left(\frac{\omega}{c\mu_a}\right)^2\right]^{\frac{1}{2}} + 1\right\}^{1/2} \quad \textbf{(2-7)}$$

$$k_{imag} = \sqrt{\frac{3}{2}\mu_a\mu_s'}\left\{\left[1+\left(\frac{\omega}{c\mu_a}\right)^2\right]^{\frac{1}{2}}-1\right\}^{1/2} \quad \textbf{(2-8)}$$

$$D = \frac{1}{3(\mu_a+\mu_s')} \quad \textbf{(2-9)}$$

Typically, the solution above is used alongside a calibration technique, often consisting of a measurements of a silicone tissue-simulating phantom with known optical properties, to calibrate the system and remove the instrument response. An iterative least square fitting algorithm is then used to solve the inverse problem and calculate the optical properties from the changes of raw amplitude and phase. An alternative method is a computational technique that uses Monte Carlo (MC) simulation results to create a Look Up Table (LUT) or Neural Network which can be used to estimate the optical properties. Beer's Law is then used to calculate the concentrations of the major chromophores present in tissue at the wavelengths of interest. For wavelengths in the near infrared, between 600 nm and 1000 nm, the most prominent chromophores are oxyhemoglobin, deoxyhemoglobin, water, and lipids. In muscle tissue, myoglobin is another major absorber of light that has a very similar absorption spectrum to hemoglobin. Since the absorption of hemoglobin and myoglobin cannot easily be decoupled, optical measurements on muscle often combine the concentration and saturation of myoglobin and hemoglobin [10]. Myoglobin has one heme group compared to hemoglobin's four, so it is important to note that the absorption spectrum of myoglobin is 1/4th the magnitude of hemoglobin, but is still a significant contributor to absorption in muscle [10]. Other chromophores such as methemoglobin, melanin, and collagen have some absorption in the near infrared, but are

either specific to certain regions of tissue (the epidermis in the case of melanin), or have very low absorption in the NIR wavelengths, and therefore do not contribute significantly to the overall absorption of light.

There are several applications for DOS that are being investigated by various research groups. Widespread work is being done to look at responses to chemotherapy treatments, especially for breast cancer [5], [7], [15], and there is work monitoring the hemodynamics of the brain [8]. Additionally, some groups have been probing the oxygenation of various muscles to learn more about muscle and exercise physiology [9]. In this work, I have used a custom FD-DOS system to investigate two important applications in cardiovascular and respiratory dynamics, which are two lesser explored application areas with FD-DOS.

2.2: Benchtop Gold Standard FD-DOS System

The benchtop gold standard FD-DOS system in our lab uses a network analyzer (Agilent Series E5061B) to modulate the light in time to collect data in the frequency domain. The system design is modeled after a system developed and described in the early and important work by the Tromberg research group [13]. The benchtop DOS system in our lab contains 6 different laser diodes with wavelengths of 658, 690, 785, 808, 830, and 850 nm coupled into one fiber bundle. Each laser is self-contained with its own Thorlabs laser module (Thorlabs LDM9T), which contains a Bias-Tee that combines the DC signal provided by a current controller (ILX, LDC-3908), and the AC signal provided by the network analyzer. Each laser is modulated in a sweep of frequencies from 50 - 500 MHz,

and an RF switch (101673-HMC252QS24, Hittite Microwave Corp., Chelmford, MA) controls the modulated power coming from the network analyzer to each of the lasers sequentially. Both the source and detector paths are fiber coupled by 400 µm and 1 mm optical fibers respectively (Fiberoptic Systems, Inc). The detector is an avalanche photodiode (APD) (Hamamatsu S11519-30) with an active area of 3 mm. The APD collects the light, which is then amplified by a preamplifier (see Appendix A-8 for the circuit), and routed back to the network analyzer to compute the changes in amplitude and phase of the input vs output signals. Additionally, the system contains a broadband halogen light source (Ocean Optics) and a spectrometer (Avantes Avaspec-HS2048) which when combined with the FD-DOS measurements is used to determine the absorption and scattering coefficients at all wavelengths between 600-1000 nm [16]. A block diagram of the benchtop gold standard system is shown in Figure 2-2. During my time as a research assistant, prior to starting my doctoral program, I was involved with fabricating this instrument by designing the Labview code that communicates with each component of the system to take a measurement.

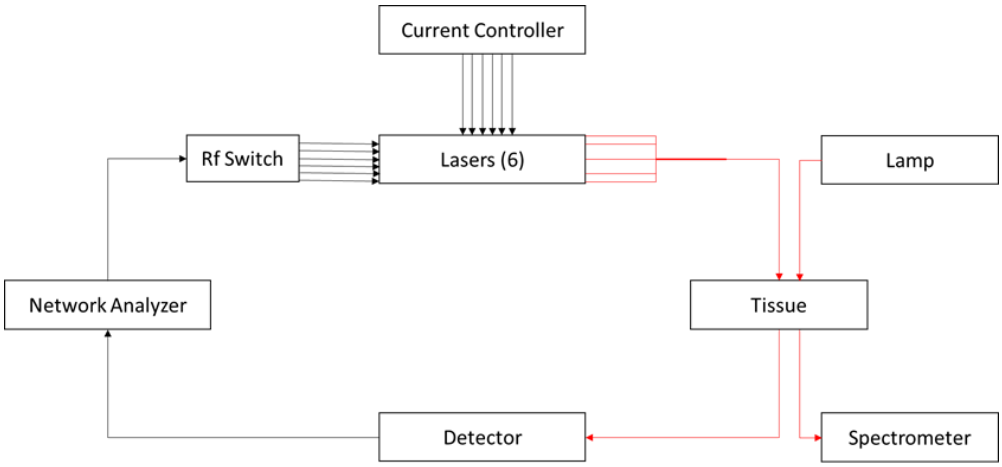

Figure 2-2. Block diagram for the gold standard benchtop FD-DOS system in the lab.

2.3: Our Custom Digital FD-DOS Platform

A custom FD-DOS platform has been developed over the last several years in our research group and has been referred to by different names for different projects, including digital FD-DOS, dDOS, FD-DOS, and FD-NIRS. Several members of the Roblyer group (Torjesen, Applegate, Gómez, and various senior project groups) as well as the Electronics Design Facility at BU were involved with designing, developing, and testing various iterations of the system.

The custom FD-DOS system replaces the network analyzer with Direct Digital Synthesizers (DDS) to generate fast (MHz) sinusoidal signals, which are used to modulate the lasers. An Analog to Digital Converter (ADC) is used to collect and digitize the detected signal. This signal is compared to a reference signal sent out directly from the DDS boards to calculate the changes in amplitude and phase [17], [18]. Additionally, the dDOS system modulates the lasers simultaneously by multiplexing the lasers (each laser starts the sweep at a different frequency in the frequency range) to further increase the measurement rate. Recently, other group members have implemented a Goertzel algorithm to compute amplitude and phase on a field-programmable gain array (FPGA) and have implemented a deep neural network to calculate and view chromophore changes in real time [19]. As a result, the dDOS system takes measurements at a much faster rate than the gold standard system over a wide range of modulation frequencies. A measurement consisting of a sweep of 36 frequencies from 50 MHz to 295 MHz can be repeated at a repetition rate of almost 30 Hz [18]. In comparison, the network analyzer-based benchtop DOS system takes measurements every 10 seconds or 0.1 Hz. The increased speed provided by dDOS allows

for the capture and investigation of faster physiological dynamics.

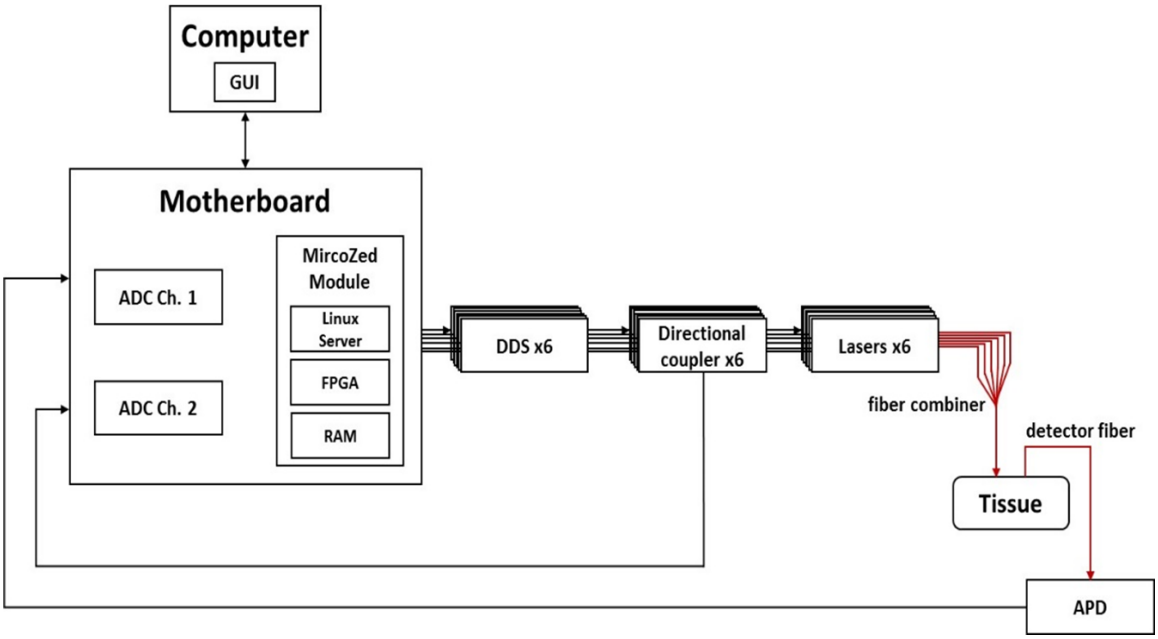

Figure 2-3. Block diagram for the first iteration of the custom fast FD-DOS system [18]**.**

2.4: Towards a high-speed clinic ready FD-DOS system

A major limitation of the initial versions of the digital FD-DOS system was that the system was not portable and could not be transported to be used for clinical measurements. Later iterations of the system focused on miniaturizing the system to make it more portable. A first step was to place the system on a cart that can be transported. This task involved placing and aligning the lasers on a small optical breadboard which was performed mostly by a fellow lab member (Gómez). This design was fully tested when we successfully transported the cart system to the Beckman Laser Institute at the University of California, Irvine (UCI) to collect data on rabbits (presented in chapter 3). An image of the cart system is shown in Figure 2-4. The next version of the system involved miniaturizing the components even further with the goal of housing the system into an instrument box. For

this step, the benchtop laser modules were replaced with fiber coupled pigtail lasers (Blue Sky FMXL730-030YFGA, Thorlabs LP852-SF30), and the large ILX DC current controller was replaced with much smaller DC current modules. I performed much of the preliminary design and testing, but the final designs were implemented by a fellow lab member (Gómez). A preliminary version of this box system was used to collect data on the healthy volunteers (presented in chapter 4).

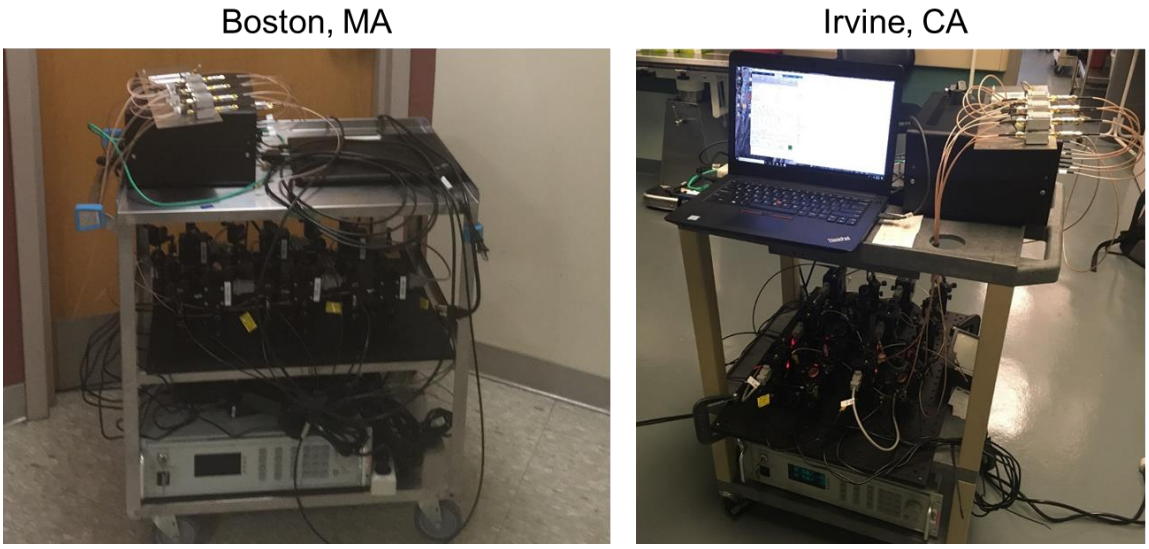

Figure 2-4. An image of the cart system assembled in our lab in Boston (left), and then the taken apart and reassembled in the University of California, Irvine to be used during a rabbit study (right).

2.5: Integrating a high-speed detector for fiber coupled measurements

Several detectors were investigated and tested to find the most appropriate detector for fiber coupled measurements. APDs were selected as the detectors of choice because of their relatively high dynamic range and high degree of linearity compared to other detectors such as photomultiplier tubes (PMT) that we have tested previously. The three APDs that

we tested were: a 0.5 mm active area (Hamamatsu C5658 with detector S-6045), a commercial APD module with a 1 mm active area and built-in temperature control (Hamamatsu C12702), and an APD with a 3 mm active area (Hamamatsu S11519-30) with a custom module designed and built by a combination of the Beckman Laser Institute at UCI and our lab at BU. Signal to Noise Ratio (SNR) was used as the primary metric of comparison. The SNR for each detector was calculated by comparing the signal from a silicone optical phantom to the signal (noise) measured from a dark absorbing rubber piece. The results are presented in Figure 2-5. The 0.5 mm APD was originally part of a breast probe designed to be used in direct contact with tissue. When it was used as a fiber coupled detector, it had lower SNR than the alternatives. The commercial module had temperature control and a high signal at lower modulation frequencies; at higher modulation frequencies, the signal dropped off considerably. The 3 mm APD had the highest SNR across the entire range of modulation frequencies that were tested (50-500 MHz). However, this APD was highly temperature sensitive and therefore required proper temperature control using a thermoelectric cooler (TEC). The 3 mm APD was actively temperature controlled using a PID Controller (Laird) and once a proper TEC and TEC controller was integrated into the module, it was determined to be the best of these detectors for use in our FD-DOS system.

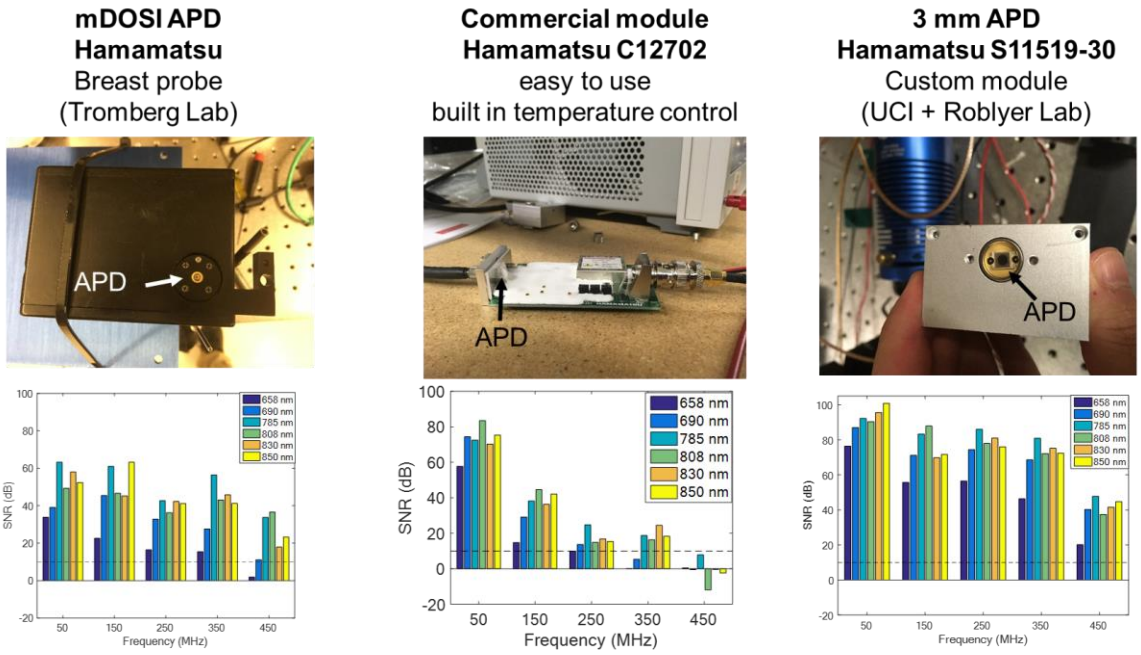

Figure 2-5. A comparison of three different detectors that were investigated for the FD-DOS system. An image of each detector is shown in the top row, while the relative SNR for each detector is shown in the bottom row.

2.6: Characterizing the performance of the custom FD-DOS system

One of my primary contributions in building a clinic ready FD-DOS system was to characterize the performance of each iteration of the system. There have been multiple iterations of the system over the past several years and in this work I will present the tests of the two systems that were used to collect data in chapters 3 and 4. In order to differentiate between the two versions, the system used in chapter 3 will be called the "cart system" while the system used in chapter 4 will be called the "box system". These two versions were used for different applications and therefore use separate wavelengths and modulation frequencies. The cart system used six wavelengths (658, 690, 785, 808, 830 850 nm) and 36 modulation frequencies (50- 295 MHz in steps of 7 MHz). The box system used two

wavelengths (730 nm and 850 nm) and one modulation frequency for each wavelength (145 MHz and 155 MHz respectively). The three major performance metrics used to characterize the systems were Signal to Noise Ratio (SNR), accuracy, and precision/drift.

2.6.1: SNR

An SNR test compares the optical signal of the system with the noise level. Several methods to calculate the SNR were used, which will be described here. For the cart system, the relative SNR was calculated by measuring an optical phantom with the following optical properties: μ_a = 0.019 mm^{-1}, μ_s' = 0.77 mm^{-1}, at 658 nm in comparison to a measurements of the noise dark signal taken from a black absorbing piece of rubber. Note that the lasers, detector, and electronics were on during the dark measurement, but light was unable to travel from the source fiber to the detector fiber because of the absorbing back rubber piece. SNR was calculated in decibels as $20*\log_{10}$(signal/noise). The SNR results at a selection of modulation frequencies are shown in Figure 2-6. This method of calculating SNR only included electronic or dark noise and was updated in future measurements to also include shot noise. The SNR from the box system was calculated using this updated method by calculating the standard deviation of repeat measurements divided by the mean of the measurements on an optical phantom with the following optical properties, which are similar to neck tissue (μ_a = 0.034, 0.017 mm^{-1} and μ_s' = 0.51, 0.50 mm^{-1} at 730, 850 nm) subtracted by a dark measurement from a black absorbing piece of rubber. SNR was calculated in decibels as $20*\log_{10}$((signal-dark)/std (signal)). The resulting SNR was 42.0 dB and 42.3 dB for 730 nm and 850 nm respectively (at a modulation frequency of 145 and 155 MHz respectively).

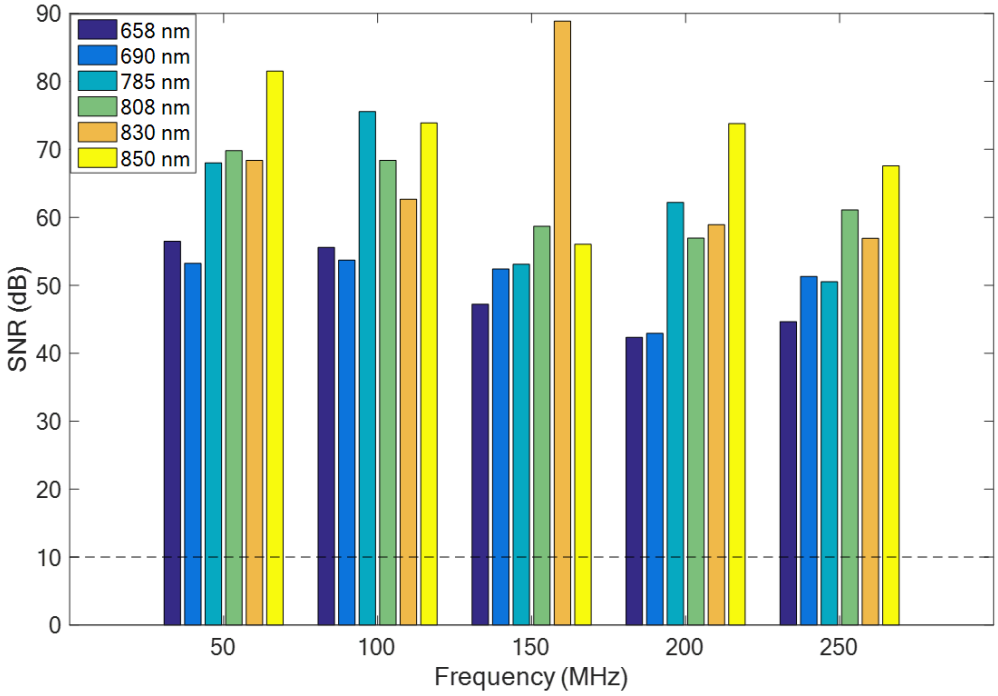

Figure 2-6. Relative SNR values for the cart system at 6 wavelengths and 5 modulation frequencies

2.6.2: Accuracy

An accuracy test was used to compare the measured optical properties (μ_a and μ_s') of the digital FD-DOS system to those measured with the gold standard system. This test was typically performed on a set of silicone optical phantoms mimicking the optical properties of the tissue of interest. The gold standard system was a benchtop network analyzer (NA) based FD-DOS described previously. Figure 2-7 shows a correlation plot of the cart system compared to the benchtop system. The average difference between the two measurements (accuracy) was 0.0037 mm^{-1} (19.6 %) for μ_a and 0.11 mm^{-1} (16.5 %) for μ_s'. Figure 2-8 shows a correlation plot of the box system compared to the benchtop system. The average difference between the two measurements (accuracy) was 0.00074 mm^{-1} (5.2

%) for μ_a and 0.039 mm^{-1} (4.9 %) for μ_s'. The improvement in accuracy for the box system was due to several factors, including an overall improvement of the SNR of the system. Additionally, a smaller set of phantoms was used that better mimicked the tissue of interest, and there may have been less crosstalk between the lasers due to only 2 lasers being modulated simultaneously.

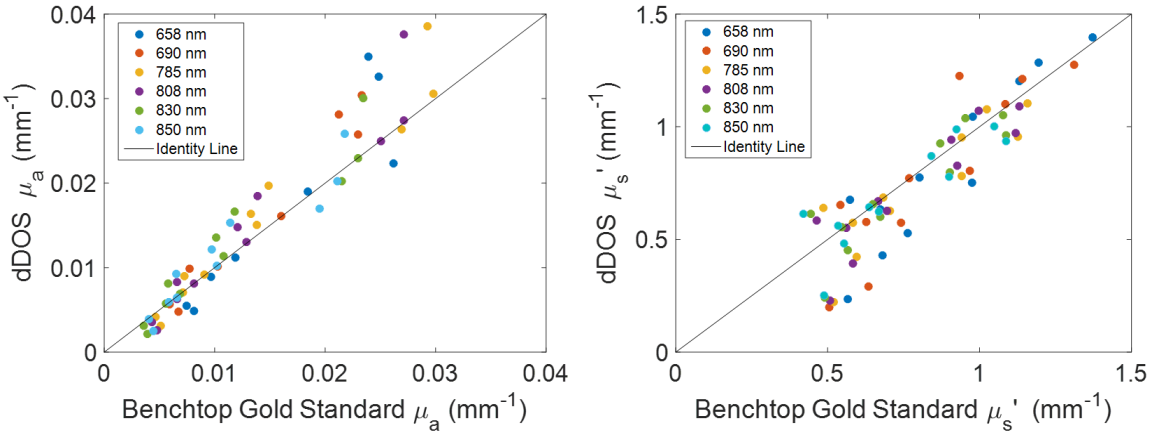

Figure 2-7. μ_a and μ_s' correlation plots between the cart system and the benchtop NA gold standard system. The average difference between the two measurements (accuracy) was 0.0037 mm^{-1} (19.6 %) for μ_a and 0.11 mm^{-1} (16.5 %) for μ_s'.

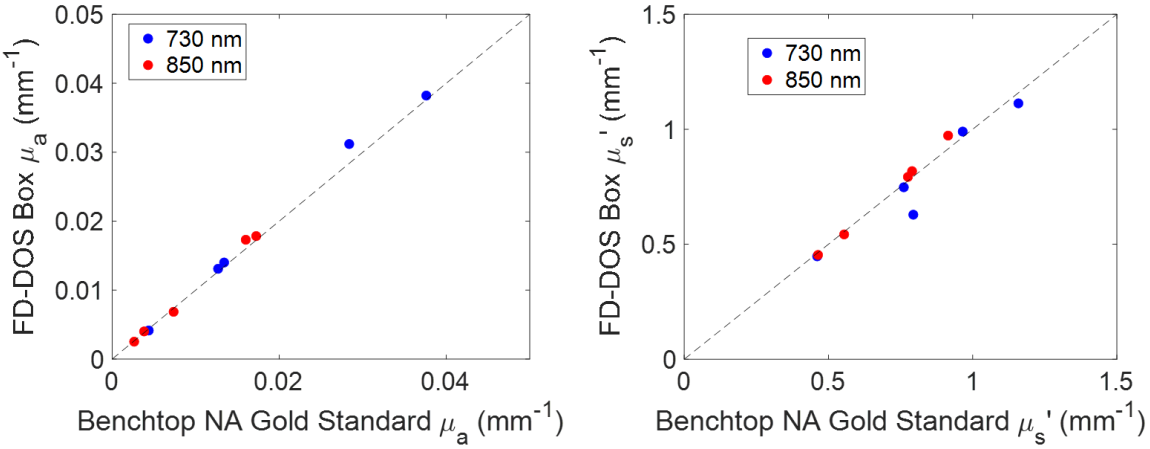

Figure 2-8: μ_a and μ_s' correlation plots between the box system and the benchtop NA gold standard system. The average difference between the two measurements (accuracy) was 0.00074 mm^{-1} (5.2 %) for μ_a and 0.039 mm^{-1} (4.9 %) for μ_s'.

2.6.3: Precision/Drift

A drift test, in which repeat measurements were taken on the same static phantom over time, was used to calculate measurement precision as well as the longer-term instrument drift of a system. Characterizing changes over time helps to ensure that the instrument produces consistent results over different timescales (e.g., over minutes, hours, days, etc.). The metrics used here to calculate precision were the coefficient of variation (%) for amplitude and standard deviation (°) for phase. Measurements were taken every minute for an hour for the cart system, and 10 times per second for 10 minutes for the box system. Figure 2-9 summarizes the results for the cart system. A precision of 1.15% in amplitude and 0.626° in phase averaged across all wavelengths and modulation frequencies with minimal drift was observed over the time period. Similar results were reported for the box system; the precision was 1.73%, 1.72% amplitude and 0.37°, 0.17° phase at 730, 850 nm, respectively, with minimal drift. Generally, our in-house benchmark for precision is less than 1% in amplitude and 1° in phase over the course of a few hours. For these systems, the phase precision exceeded our target while the amplitude target fell just short, but still had a minimal effect on the resulting optical property measurements confirming that the consistency of the system over minutes and hours was sufficient to take physiological measurements.

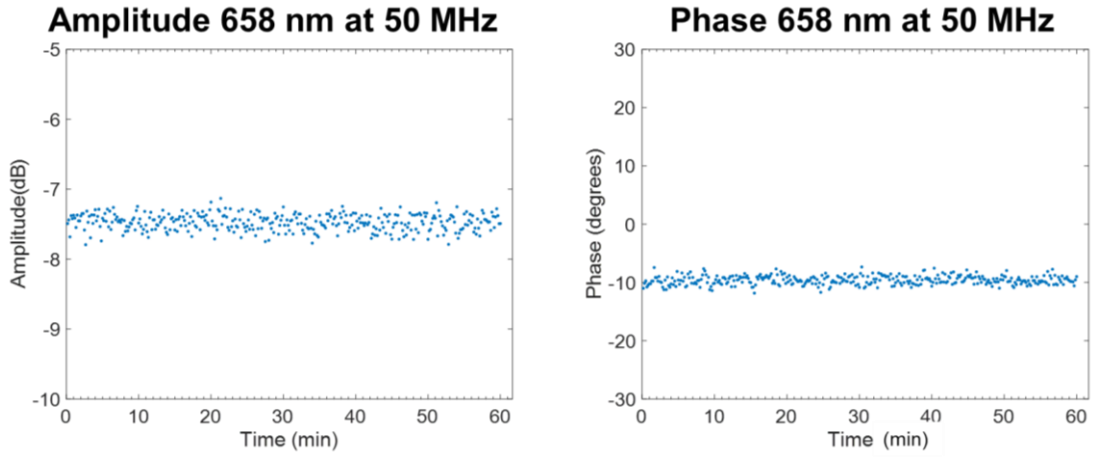

Figure 2-9. Results of a drift test taken on the cart system. The precision was 1.15% in amplitude and 0.626° in phase averaged across all the wavelengths and modulation frequencies. Minimal drift was observed over the course of an hour.

2.6.4: Performance Tables

A summary of the most important parameters and performance metrics of each system is shown in Table 2-1 (cart system) and Table 2-2 (box system).

Table 2-1. The measurment parameters and performance metrics for the cart system used in chapter 3.

Cart System Parameters and Performance	
Wavelengths	658/690/785/808/830/850 nm
Modulation Frequencies	50:7:295 MHz
Source-Detector Separation	10 mm
SNR**	57.6 dB*
μ_a Accuracy	0.0037 mm^{-1} [19.6 %]
μ_s' Accuracy	0.11 mm^{-1} [16.5 %]
Amplitude Precision	1.15%*
Phase Precision	0.626°*
Measurement Rate	27 repetitions/sec

*average across all wavelengths and modulation frequencies
**Measured on an optical phantom with the following optical properties:
μ_a = 0.019 mm^{-1}, μ_s' = 0.77 mm^{-1}, at 658 nm
50:7:295 MHz means from 50 to 295 MHz in steps of 7 MHz

Table 2-2. The measurment parameters and performance meterics for the box system used in chapter 4.

Box System Parameters and Performance	
Wavelengths	730/850 nm
Modulation Frequencies	145/155 MHz
Source-Detector Separation	25 mm
SNR**	42.2 dB*
μ_a Accuracy	0.00074 mm^{-1} [4.9%]*
μ_s' Accuracy	0.039 mm^{-1} [5.2 %]*
Amplitude Precision	1.73%*
Phase Precision	0.27°*
Measurement Rate	~10 repetitions/sec

*average across all wavelengths
**Measured on an optical phantom with the following optical properties:
μ_a = 0.034,0.017 mm^{-1} and μ_s' = 0.51,0.50 mm^{-1} at 730,850 nm

2.7: Physiological Example

The increased speed of the FD-DOS system allows for unexplored physiological measurements, potentially capturing rapid physiological changes such as those that occur during the cardiac or respiratory cycles. In order to show an example of physiological signals that could not be measured by previous FD-DOS systems, a cuff occlusion was performed, and optical measurements were taken at high speed on the finger of a healthy volunteer. Figure 2-10 shows the results of the occlusion. The cuff was inflated to a pressure of 200 mmHg on the upper arm, likely occluding both arteries and veins. Fast FD-DOS measurements were taken at a speed of 20 Hz for a total of 7.5 minutes starting from 2.5 minutes before the occlusion and ending 2.5 minutes after the occlusion. As expected, there is a noticeable drop in oxyhemoglobin (oxy[Hb]) and a noticeable increase in deoxyhemoglobin (deoxy[Hb]) during the occlusion, with both reverting back to baseline after the end of occlusion. Additionally, fast oscillations in oxyhemoglobin and total

hemoglobin were present during baseline, disappeared during the occlusion, and reappeared afterwards (Figure 2-10b, c, and d). These oscillations were due to changes within the cardiac cycle, relating to increases and decreases in the volume of blood in the arterial blood. The systolic peak, diastolic peak, and dichroitic notch can be identified in these oscillations (see inset) and are similar to those same features observed in photoplethysmography (PPG) [19]. There was also a noticeable drop in total hemoglobin (total[Hb]) during the occlusion, which may be due to gravity. The fingers were raised during the measurement, and since there was no influx of new blood, it is possible that the blood pooled in the arm which was lower than the fingers during the occlusion.

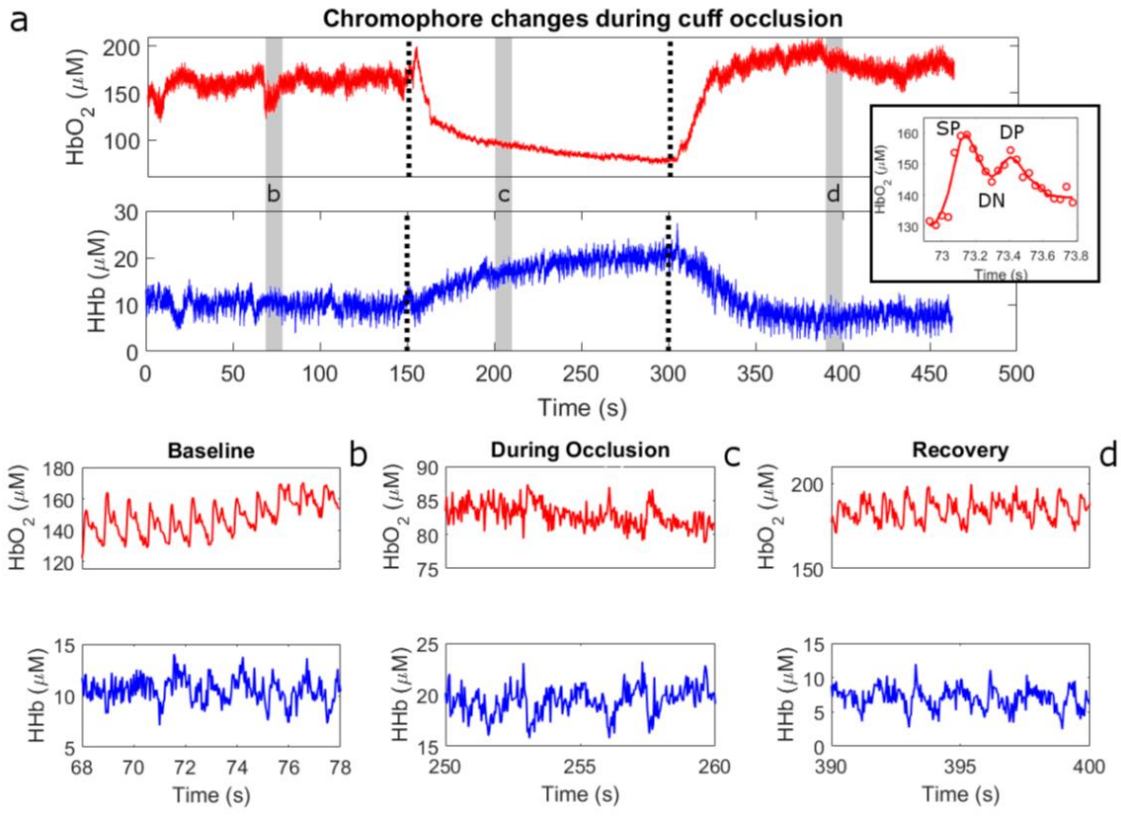

Figure 2-10. A cuff occlusion was performed while FD-DOS measurements were collected at 20 Hz on a finger. (a) The entire cuff occlusion measurement. (b - d) snapshots of the occlusion before, during and after the occlusion. SP = systolic peak, DP = diastolic peak, DN = dichroic notch [19].

2.8: Conclusion

A custom digital FD-DOS system was designed and fabricated. One major advantage of this system is the increased measurement rate allowing for the measurement of faster physiological signals. This system went through several iterations during the last several years with the goal of making a high-performance, portable, and clinic-ready FD-DOS system. For each of these updates, the system was performance tested to ensure that it is provides accurate measurements consistently over minutes and hours (the amount of time needed to take a series of measurements). The two versions of the system highlighted in this chapter (cart and box) were used to take the physiological measurements described in chapters 3 and 4, respectively.

CHAPTER 3: Evaluating the Feasibility of using FD-DOS for Non-invasive Venous Oxygen Saturation Measurements

3.1: Background

In order for cells to survive, they need to receive a near constant supply of oxygen. The vast majority of this oxygen is transported throughout the body through the circulatory system and is bound to hemoglobin, a protein whose primary function is to bind oxygen. Additionally, there is a small amount of oxygen dissolved in blood, but that amount (~ 2% of total O_2) is negligible compared to the amount bound to hemoglobin (~ 98% of total O_2) [20]. Therefore, the tissue regional oxygen saturation, the percentage of hemoglobin that is bound by oxygen, is an important parameter related to the efficacy of oxygen delivery as well as the utilization of oxygen by metabolically active tissues.

The level of oxygen saturation varies as blood travels throughout the body. The left side of the heart pumps blood coming from the lungs that is almost completely oxygenated (approximately 97% [21]). The oxygen saturation level of the blood as it flows though the arteries to the rest of the body is called arterial oxygen saturation (SaO_2). The blood then travels through capillaries and delivers oxygen to the body. As the blood leaves the capillaries, hemoglobin becomes less oxygenated (approximately 70%) [22], however there is a still a significant amount of oxyhemoglobin to act as a surplus when the body requires exertion (e.g. during exercise). Venous oxygen saturation (SvO_2) is the oxygen saturation of the blood traveling in the venous circulation to the right side of the heart and back to the lungs. SvO_2 is important because it relates oxygen delivery (supply) to oxygen consumption (demand). If SvO_2 is too high, either the supply is too high, or the demand is

too low. For example, cyanide poisoning causes the mitochondria to stop functioning, lowering the oxygen demand of the body [23]. If SvO_2 is too low, either the supply is too low, which can happen if there is clogged artery or a respiratory problem, or the demand is too high, which happens during metabolic stress, trauma, infection or exercise [24]. In the case of exercise, the body compensates for the higher demand by increasing oxygen supply (i.e., dilating blood vessels, increasing heart rate), or by increasing oxygen extraction (i.e., increasing the removal of oxygen from the blood in tissue). In comparison, SaO_2 only provides knowledge about oxygen delivery and is therefore unable to provide a complete picture of the cardiopulmonary state.

Pulse oximetry is widely used in the clinic to measure peripheral oxygen saturation (SpO_2), a surrogate for SaO_2. A pulse oximeter clips onto a finger, ear, or nose. On one side of the clip, two wavelengths of light are emitted, typically above and below 800 nm, the isosbestic point of hemoglobin, and a photodiode (detector) on the other side of the tissue detects the light that passes through. Absorption of light at these wavelengths is mostly due to hemoglobin in tissue. Since the absorption spectrum of oxyhemoglobin and deoxyhemoglobin differ in this wavelength range (600-1000 nm), the use of two or more wavelengths within this range can be used to distinguish their relative concentrations. During the cardiac cycle, it is believed that the volume of arterial blood changes within each pulse, while the volume of venous and capillary blood remains relatively constant [1], [25]. Therefore, the pulse oximeter can isolate arterial oxygen saturation from total oxygen saturation because the pulsatile changes of absorption over time are primarily due to pulsatile nature of arterial blood. However, pulse oximetry has several limitations. Blood

in the capillaries and veins likely do not pulse at the cardiac frequency and therefore SvO_2 cannot be measured with pulse oximetry. Additionally, pulse oximetry is unable to measure absolute concentrations of oxyhemoglobin and deoxyhemoglobin because current systems use CW light.

To measure SvO_2, typically, a pulmonary artery catheter (PAC) is inserted into the superior vena cava and advanced through the right side of the heart into the pulmonary artery as shown in figure 3-1. This type of measurement is invasive and can lead to complications such as infection, bleeding, and thrombosis. Typically, a fiber optic probe is used to take measurements of SvO_2 every hour [personal correspondence with Dr. Ashvin Pande, director of invasive cardiology at Boston Medical Center].

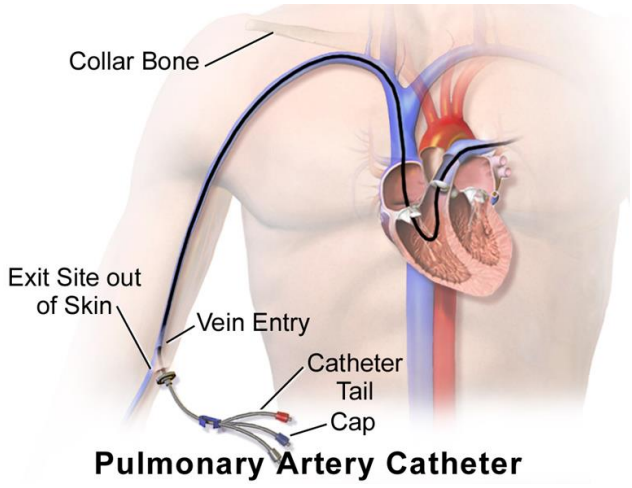

Figure 3-1. Diagram of a pulmonary artery catheter as it is being inserted into a vein and through the right side of the heart into the pulmonary artery. Image from https://commons.wikimedia.org/wiki/File:Pulmonary_Artery_Catheter.png (BruceBlaus Own Work)

While there have been multiple studies investigating the utility of SvO_2 in prognosticating various disease conditions [8,9], currently, the main clinical use for measuring SvO_2 is to use it to estimate cardiac output (CO) using Fick's principle. CO is a

measurement of the efficiency of the heart and is an important parameter that doctors use to diagnose and monitor various cardiovascular diseases including sepsis, hypertension, and heart failure [26]. Fick's principle is considered the gold standard for estimating CO [27]. The equation for Fick's principle (equation 3-1) relates cardiac output to oxygen consumption and the arterio-venous oxygen difference, where CO is cardiac output typically in units of L/min, VO_2 is oxygen consumption measured in units of ml O_2/min, C_a is the oxygen concentration of arterial blood, and C_v is the oxygen concentration of venous blood, both of which are typically in units of ml O_2/L blood:

$$CO = \frac{VO_2}{C_a - C_v} \qquad \textbf{(3-1)}$$

Since the vast majority of oxygen in the blood is bound to hemoglobin, the arterio-venous oxygen difference C_a-C_v can be calculated by taking two samples of blood (arterial and venous) and comparing SaO_2 with SvO_2. Oxygen consumption is commonly estimated using a variety of different formulas that often include body surface area, age, and/or sex. The mean oxygen consumption rate for an average human is approximately 250 ml O_2/min at rest [28]–[30].

There is not yet a widely accepted technique for measuring SvO_2 non-invasively in the clinic. Some groups have attempted to noninvasively measure SvO_2 with NIR light using both CW-DOS and FD-DOS modalities. A variety of different methods have been attempted, each having their own advantages and disadvantages. Some groups were able to correlate oscillations in venous blood volume with breathing, and used those changes at the respiratory frequencies to provide an estimate of SvO_2 [31]–[33]. Similarly, other groups have performed venous occlusions in order to increase venous blood volume, which

allowed them to estimate SvO_2 [34], [35]. However, the inducement of external perturbations cannot be performed indefinitely and is too cumbersome to use in the clinic for some applications. Alternatively, other groups have measured tissue oxygen saturation (StO_2) in specific anatomic locations rich in venous blood to try to correlate StO_2 with SvO_2. Examples of these locations include regional cerebral SO_2 (SrO_2)[36] as well as the internal jugular vein in the neck [37]–[39]. However, many of these groups were only able to measure trends and not absolute values of SvO_2 [36]. Finally, there have also been initial attempts at extracting SvO_2 using a linear combination of SaO_2 and StO_2. StO_2 is an optically derived measurement on a region of tissue. Its value is some linear combination of SaO_2 and SvO_2 depending on the location of the tissue that is being measured [40], [41]. We will call this method the x-factor method as it relies on a parameter, x, (see equation 3-2) which weights the relative amount of arterial and venous blood present in specific tissue regions.

In this chapter, we will test the hypothesis that fast FD-DOS measurements can be used to accurately estimate SvO_2. To test this hypothesis, we have used and elaborated on several of the methods for optically measuring SvO_2 described above using the custom FD-DOS described in chapter 2. The fast measurement speed of the digital FD-DOS allows us to isolate both cardiac and respiratory hemodynamics. Use of the respiratory frequencies (i.e. hemodynamic oscillations at the respiration rate) allow us to explore respiratory blood volume oscillations while cardiac frequencies allow us to extract SaO_2. The linear combination (x-factor) method allowed for extraction of both StO_2 and SaO_2 to yield SvO_2 [40]. The specific version of the x-factor method used in this work is shown in Equation 3-

2 below.

$$SvO_2 = \frac{1}{x}StO_2 - \left(\frac{1}{x} - 1\right)SaO_2, \;\; x = \frac{Thbv}{Thb} \approx 0.75 \qquad \textbf{(3-2)}$$

However, in order to calculate SvO_2 with the x-factor method, an important assumption needs to be made relating the relative volumes of arterial and venous blood probed by light. This variable, x, is defined as the venous blood volume fraction, that is, the percentage of total blood in venous circulation (venules and veins). Since veins are much more compliant than arteries, and tissue is heterogeneous, x is variable and likely depends on the location in the body probed by light. This parameter may also depend on other parameters and may change within the breathing or cardiac cycles. Previous studies have estimated this value to be approximately 60-80% depending on the anatomic location investigated. Table 3-1 summarizes x estimates in various anatomic locations from prior literature [42]–[47]. Realizing a good estimate of this ratio for different locations is critical for achieving accurate SvO_2 measurements as well as tracking trends in SvO_2.

Table 3.1. A summary of the venous blood volume estimates from several groups in different locations around the body.

Authors	Tissue Type	Percentage of Blood in Venous Circulation
Blakemore et al.	Whole Body	70%
Elad et al.	Whole Body	64%
Boushel et. al.	Skin	70%
Pollard et. al	Cerebral	75%
Watzman et al.	Cerebral	84%
Mchedlishvili et al	Cerebral	75%

Accurate, non-invasive SvO_2 measurements would enable diagnosis and continuous monitoring of various cardiovascular diseases such as peripheral vascular disease and shock, and bring us one step closer to non-invasive determinations of CO. We

describe here how we utilized our custom FD-DOS system to attempt to achieve non-invasive SvO_2 measurements in tissue.

3.2: Methods

3.2.1: Developing a Processing Pipeline for Fast FD-DOS Measurements

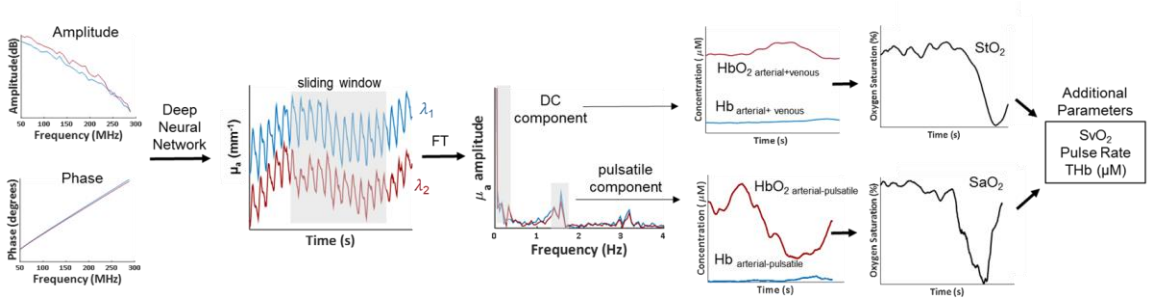

Figure 3-2. A summary of the processing pipeline that was used to process fast FD-DOS measurements. A DNN was used to calculate μ_a and μ_s' from changes in amplitude and phase. An FFT was taken of the μ_a data and chromophores were calculated using different frequency components of the μ_a signal.

A workflow was developed to extract oxygen saturation data from fast FD-DOS measurements. This workflow is summarized in Figure 3-2. The optical properties (μ_a and μ_s') were calculated in real-time using a deep neural network developed by a fellow lab member (Zhao) [19]. Then, the frequency components of μ_a were evaluated using an FFT taken over the course of the measurement. In the cases where SO_2 values are expected to change over time, such as during a breath hold, this process was performed over the last several samples using a sliding window in a backwards looking algorithm (future points were not considered). The resulting data from a set of frequencies were used to calculate chromophores using Beer's Law. There were three frequencies (or bands of frequencies) of interest: the DC frequency, cardiac frequencies, and respiratory frequencies. The DC

frequency (the DC bin) was used to calculate StO_2. This frequency bin includes values that do not change over time and therefore represents StO_2, which is the average tissue oxygen saturation. The cardiac frequencies were used to calculate SaO_2, and the changes at the respiratory frequencies were used to get an estimate for SvO_2 using the respiratory method previously described [31]–[33]. While FD data was collected for all measurements, phase data tended to be noisy compared to amplitude data. In order to improve signal integrity, FD data was only used to determine the initial tissue μ_a and μ_s'. Then, the modified beer-lambert law was used to calculate the changes in μ_a at all subsequent points from amplitude data, resulting in $\Delta\mu_a$ values at subsequent time points. This combined FD+CW method has previously been described in the literature [31], [48]. Equations 3-3 and 3-4 were used for this combined method where r represents the source-detector separation and the amplitudes for each wavelength were taken at a modulation frequency of 50 MHz.

$$\Delta\mu_a(\lambda, t) = \frac{1}{L_{eff}} * \ln\left(\frac{amp(\lambda,0)}{amp(\lambda,t)}\right) \quad \textbf{(3-3)}$$

$$L_{eff} = \frac{3\mu_s' r^2}{2\left(r\sqrt{3\mu_a\mu_s'}+1\right)} \quad \textbf{(3-4)}$$

In many cases, the peaks in the FFT occurring at the cardiac and respiratory frequencies were difficult to discern, especially at shorter wavelengths (658 and 690 nm) where deoxyhemoglobin is highly absorbing. Several techniques were used to try to isolate the signal from the noise. A simple noise subtraction algorithm was implemented by subtracting the average of the last 50 data points in the FFT (the flat portion of the FFT) to reduce noise in the absorption spectrum at each wavelength. Additionally, the decision of which frequency bins to consider for the cardiac and respiratory frequencies was

challenging and especially important in longer measurements where the cardiac and respiratory rates vary slightly over time, and therefore multiple frequency bins are needed to more fully capture the signal. The half max method was used to select all frequencies within a specified bandwidth (~0.2 Hz for cardiac frequencies and ~0.1 Hz for respiratory frequencies) that had greater than half of the maximum value in that range. The frequencies were selected using the μ_a signal at 850 nm (which had the highest signal level) and was applied to all other wavelengths. An example of this method is shown in Figure 3-3.

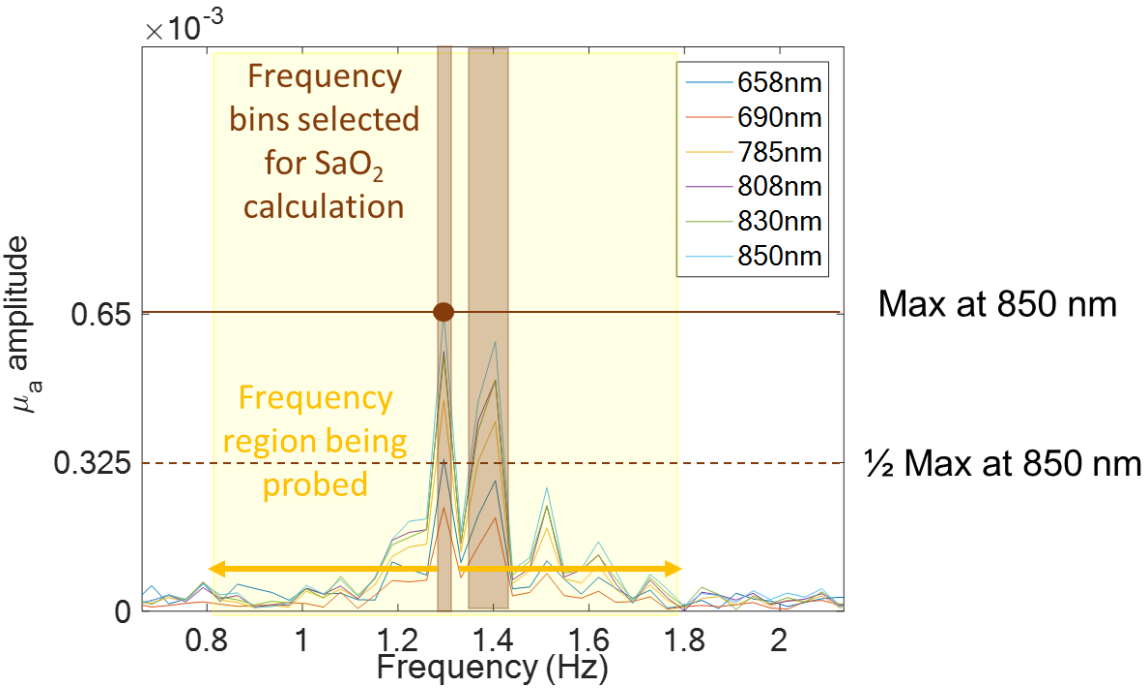

Figure 3-3. A description of the Half-Maximum method used to select frequency bins. The maximum amplitude value at 850 nm was determined, and all frequency bins within a specified range that were greater than half of the maximum amplitude were considered.

Finally, in cases where the FD-DOS data was compared to pulse oximeter (Masimo Radical 7) data, smoothing of the FD-DOS data was needed to better match the pulse oximeter measurements. Two rounds of smoothing were performed in attempt to match the

FD-DOS data with the pulse oximeter data, for which the full details of smoothing information for the latter are proprietary and not fully known. The pulse oximeter was set to average the last 2-4 seconds. In order to attempt to replicate this smoothing, a 3 second backwards looking moving average was implemented on the FD-DOS SaO_2 data. Additionally, since the FD-DOS data used an FFT with a 20 second window, an additional 20 second backwards looking moving average was applied to the pulse oximeter data.

3.2.2: System Settings

All measurements in this chapter were taken using the cart version of the digital FD-DOS system introduced in chapter 2. This version of the system uses 6 wavelengths (658, 690,785, 808, 830, 850) nm and 36 modulation frequencies from 50 MHz to 295 MHz with a step size of 7 MHz. The lasers were modulated simultaneously with a 21 MHz offset between each laser and 8192 samples were taken per frequency step. Both the source and the detector were fiber coupled and a 3 mm APD module (Hamamatsu S11519-30) was used as the detector, which was temperature controlled using a TEC. Measurements were taken with a source-detector separation of 10 mm, which was ideal for measuring superficial tissue on the fingers. With these settings, the sampling rate of the system was approximately 17 Hz, which was fast enough to extract signals at both the respiratory and cardiac frequencies. The same system was used for the both the rabbit and the healthy volunteer studies described below, with the only difference being the custom probe that held the source and detector fibers. The probe for healthy volunteer measurements included a force sensor (Interlinks Electronics 30-49649) to measure the probe pressure on the subject's finger. Figure 3-4 shows the two probe designs that were used for the

experiments.

Figure 3-4. Probe designs for the two studies using the cart system. The source fiber is on the left while the detector fiber is on the right. A force sensor (not shown) was used for the healthy volunteer study and was placed in between the source and detector fibers.

3.2.3: Healthy Volunteer Study

Achieving an accurate measurement of SaO_2 is an important step towards extracting SvO_2 using the x-factor method. We first tested SaO_2 values extracted from FD-DOS against a commercial pulse oximeter. A group of healthy volunteers (N= 9), aged 25-70 years old, were measured to compare FD-DOS derived SaO_2 to those obtained by oximetry (as a gold standard). All measurements were conducted under an institutionally approved protocol at BU (IRB 3367). We collected three types of measurements on each subject: 1) baseline, 2) breath holds to track SaO_2 dynamics, and 3) paced breathing to get an estimate for SvO_2. These measurements were taken on the right thumb of the healthy volunteers

with a commercial pulse oximeter (Masimo Radical 7) attached to the contralateral (left) thumb, which collected SaO_2 data continuously. For the breath hold, the healthy volunteers were instructed to hold their breath for 30 seconds or as long as possible following expiration. For paced breathing, the healthy volunteers were given an auditory cue to inhale and exhale at a rate of 5 seconds inhale and 5 seconds exhale (0.1 repetitions/second) for the duration of the 2-minute measurement.

Several anatomic locations were investigated to attempt to find the best location for these fast measurements. The thumb was chosen for its relatively large cardiac signal, which could often be felt with palpation. This signal is attributed in part to a fairly large arteriole in this tissue region. Other locations where a strong cardiac pulse was observed include the other four fingers, the radial and ulnar regions of the wrist, the brachial region near the elbow, and the forehead. All of these locations are relatively close to larger arterioles or arteries that likely produce the oscillations at the cardiac frequency.

3.2.4: Rabbit Study

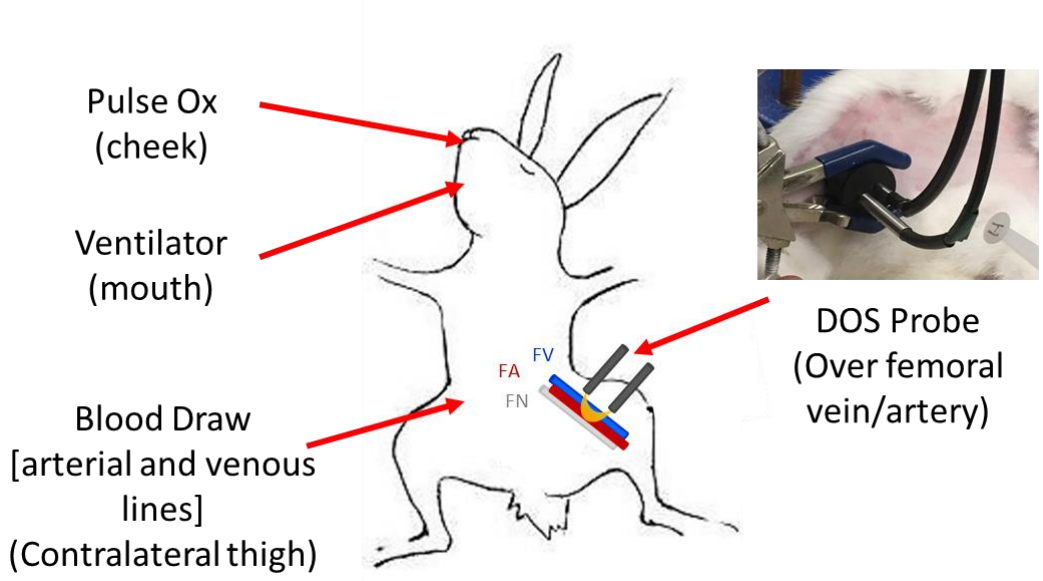

Figure 3-5. A diagram of the setup used for the rabbit study

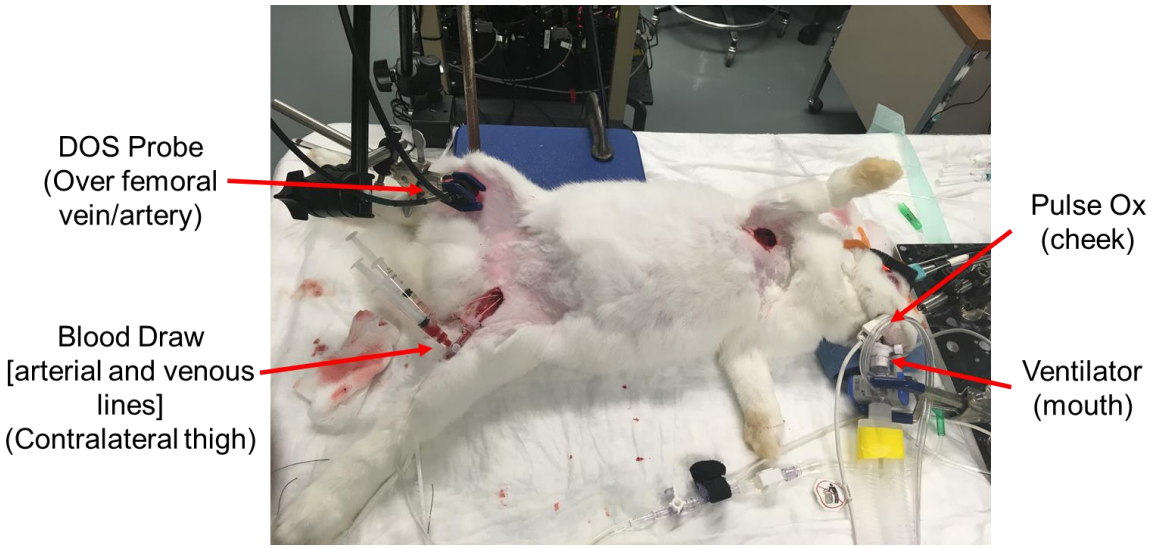

Figure 3-6. An image of the setup used for the rabbit study

A rabbit study (n=3) was conducted to compare our FD-DOS SvO_2 values to an invasive gold standard. This study was a group effort that included fellow lab members

(Applegate, Roblyer) alongside collaborators from the University of California, Irvine. Figure 3-5 shows a diagram of the system setup while Figure 3-6 shows a photograph of the system setup. The rabbits were placed face up and the optical probe was placed over the right thigh of the rabbit over the right femoral vein and artery. Blood was drawn from both arterial and venous lines from the contralateral (left) thigh. A ventilator was attached to the mouth of the rabbit to control the breathing rate and a pulse oximeter was attached to the cheek of the rabbit to provide a separate measurement of SaO_2. A series of oxygen steps, controlled by varying the inspired oxygen (FiO_2), were conducted on each rabbit. Three different levels of oxygen were used, 100% O_2, 21% O_2 (room air), and 16% O_2. For each measurement point, both arterial and venous blood samples were drawn and a 2000-point (~2 minute) FD-DOS measurement was taken immediately following the blood draw. Each measurement (blood draws + FD-DOS measurement) took around 10 minutes with most of the time used to ensure that the rabbit reached a steady-state after each change of inspired oxygen. A summarized schematic of the rabbit study timeline is shown in Figure 3-7.

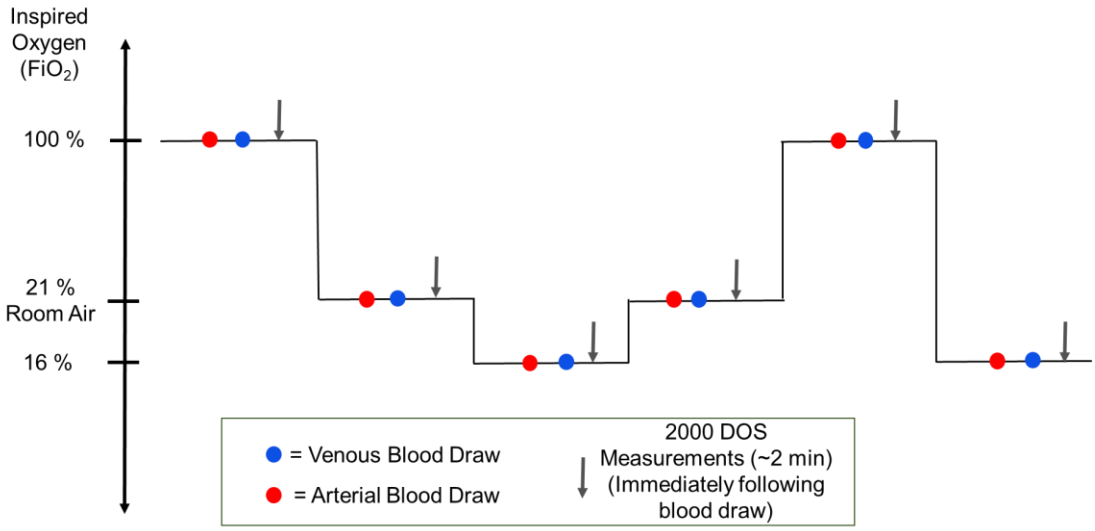

Figure 3-7. A diagram of the rabbit study timeline used during FiO_2 sweeps. At each FiO_2 level, an arterial and venous blood draw was taken followed by a two minute FD-DOS measurement.

3.3: Results

3.3.1: Healthy Volunteer Study

Breath holds were used to compare SaO_2 to pulse oximetry**.** These breath holds were often difficult to perform for the subjects, and only those that were performed in a particular manner successfully reduced SaO_2. For a breath hold to be considered successful, the subject needed to hold their breath, after expiration, for a sufficiently long time for the gold standard pulse oximeter SaO_2 to drop below 90%. Figure 3-8 shows an example of a successful breath hold. The FD-DOS and pulse oximeter SaO_2 values tracked fairly well together; at baseline, SaO_2 was between 95 - 100%, dropping to ~80 - 85% following the breath hold. StO_2 followed a similar trend, but the values were lower because the StO_2 measurement likely incorporates both arterial and venous blood. A summary of the data

from all of volunteers, with and without noise subtraction, is shown in Figure 3-9. There was a decent correlation between pulse oximeter and FD-DOS with an r^2 of 0.78 and 0.88 with and without noise correction respectively. However, the absolute values differed slightly. Without noise correction, the slope differs from the identity line with a slope of 1.37. With noise correction, the slope was 1.05. However, the FD-DOS values were almost all higher than the corresponding pulse oximeter values.

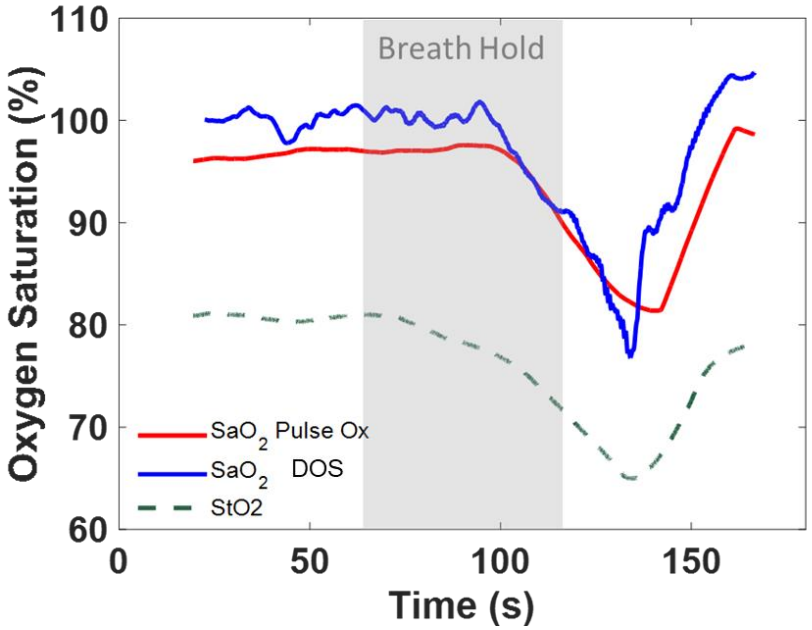

Figure 3-8. A sample breath hold measurement taken on a healthy volunteer. The breath hold duration was approximately 30 seconds and highlighted in grey. FD-DOS derived SaO_2 (blue) values are taken from the cardiac frequencies and compared to pulse oximeter SaO_2 (red). The FD-DOS StO_2 values are taken from the DC frequency on shown in green.

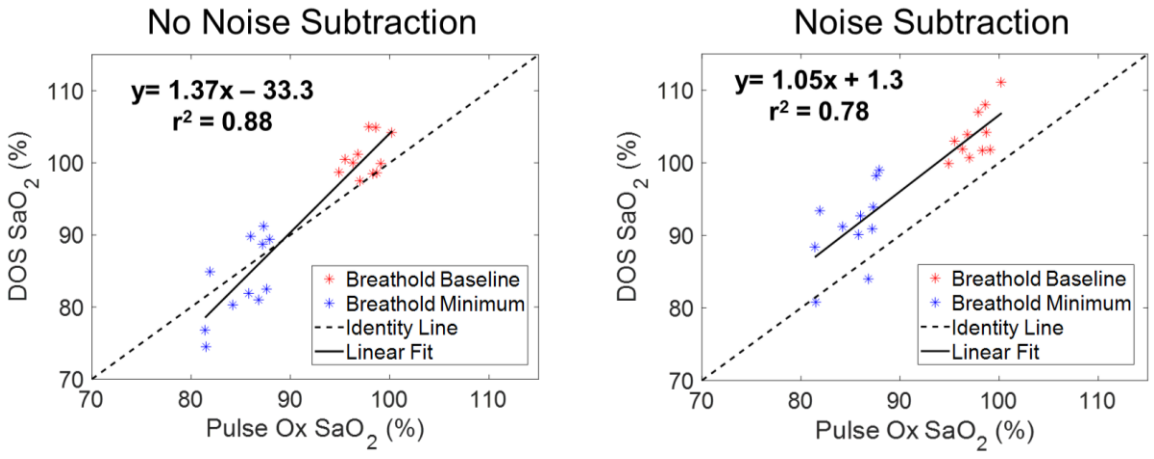

Figure 3-9. SaO_2 correlation plots for the healthy volunteers performing breath holds. Values at baseline (red) and the breath hold minimum (blue) are shown.

Paced breathing was used to enhance the amplitude of the respiratory signal. Figure 3-10 shows sample $\Delta\mu_a$ FFTs. The FFT of the paced breathing experiment had much higher amplitudes at the fixed respiratory frequency (0.1 Hz).

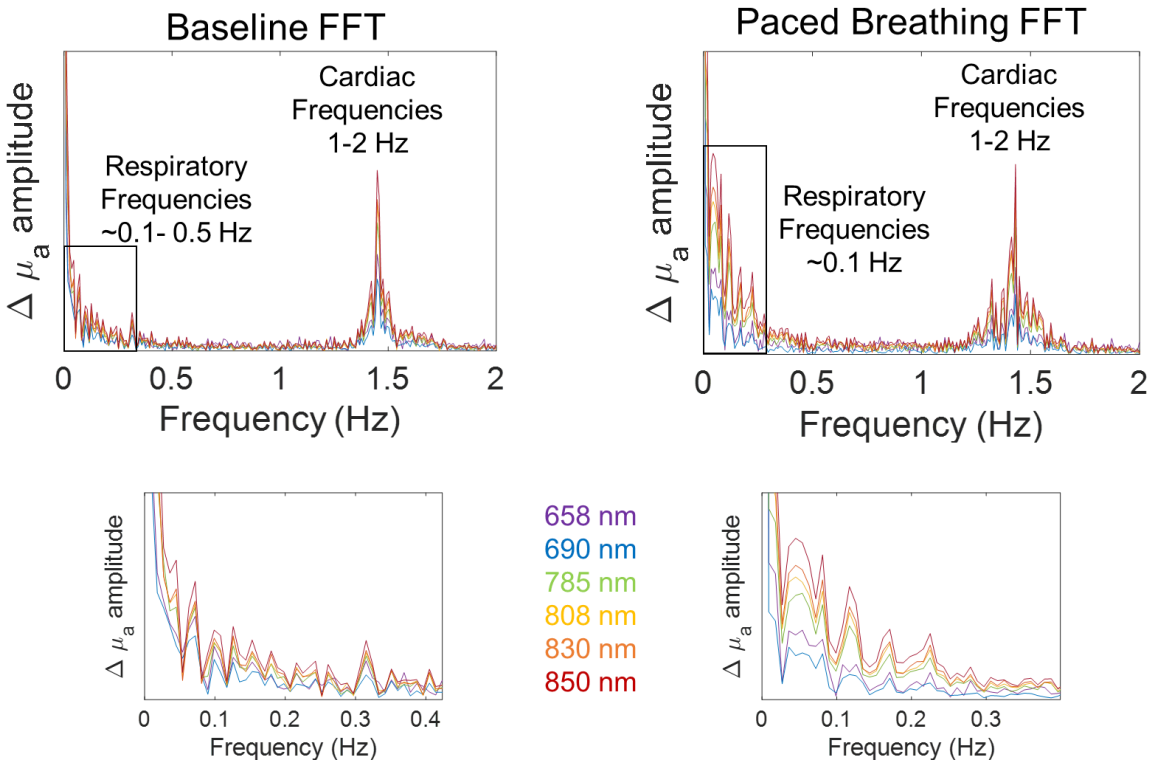

Figure 3-10. Sample $\Delta\mu_a$ FFTs measured on a healthy volunteer with and without paced

breathing. Paced breathing greatly increases the signal at the respiratory frequencies. The bottom plots show a zoomed-in version of the square regions in the top plots.

The relative FFT phase of μ_a at different wavelengths as well as the relative phase of oxy[Hb] and deoxy[Hb] was also investigated. Figure 3-11 shows another paced breathing measurement example on a healthy volunteer. In this example, the μ_a traces at each wavelength are shown to be in phase (Figure 3-11a), while oxy and deoxy are approximately 180° out of phase (Figure 3-11d and 3-11f). The other healthy volunteer data evaluated in this manner showed oscillations in deoxy[Hb] that were typically too small to allow the evaluation of the relative phase.

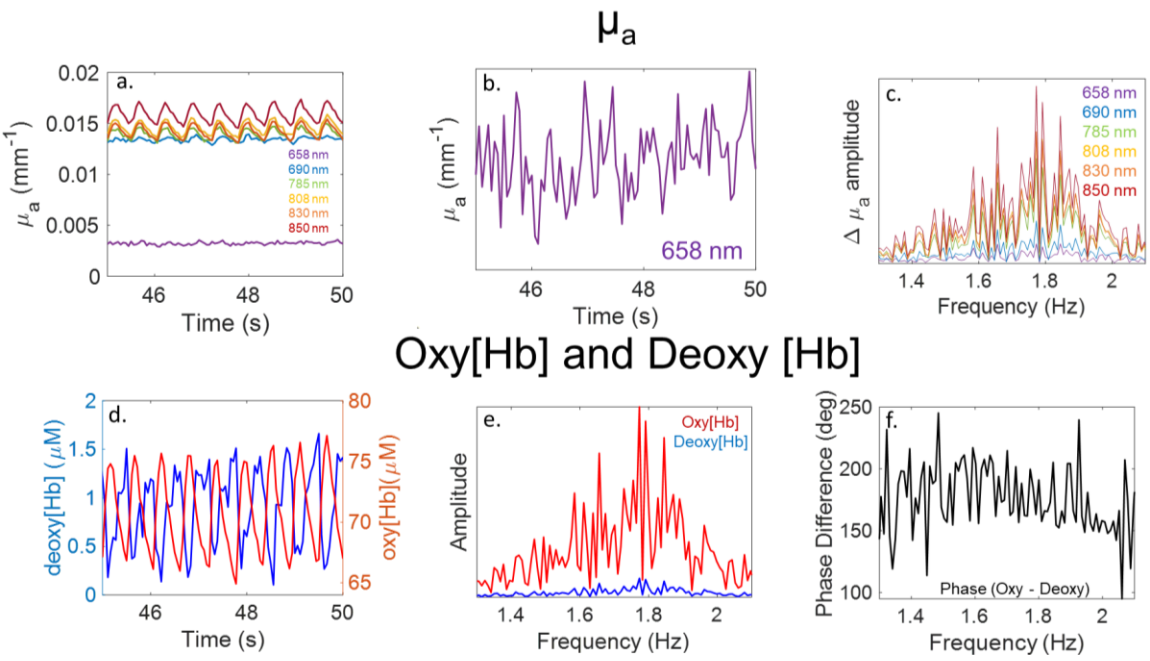

Figure 3-11. Sample μ_a, oxy[Hb], and deoxy[Hb] traces during a paced breathing experiment performed by a healthy volunteer. (a) μ_a time traces. (b) A zoomed in version of the μ_a trace at 658 nm. (c) FFT ampitude of μ_a at the cardiac frequencies. (d) oxy[Hb] and deoxy[Hb] time traces. (e) The ampitude of oxy[Hb] and deoxy[Hb] at the cardiac frequencies. (f) The phase difference between oxy[Hb] and deoxy[Hb] at the cardiac frequencies.

A summary of the estimated oxygen saturations from paced breathing measurements is shown in Figure 3-12. The DC signal has an StO_2 of 79.9% ± 7.7% while the cardiac and respiratory signals yielded saturations of 104.4% ± 3.3% and 102.2% ± 4.8% respectively.

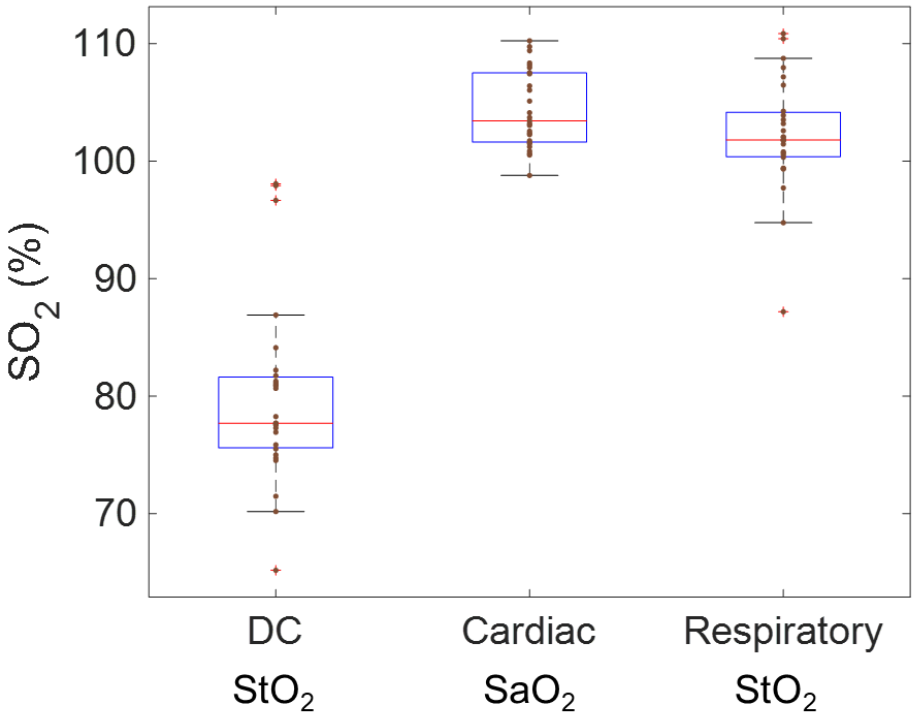

Figure 3-12. A summary of the resulting oxygenation saturation values measured using different frequencies of the paced breathing experiment.

3.3.2: Rabbit Study

StO_2 was first tested as a surrogate for SvO_2. The FD-DOS derived StO_2 was calculated by using the DC frequency (0 Hz) of the $\Delta\mu_a$ FFT and was compared to the venous blood draw measurements. The resulting correlation is shown in Figure 3-13. The values show a decent linear correlation with an r^2 of 0.70, but a worse correlation to the

identity line with an r^2 of 0.27. The next comparison used the x-factor method, which combines FD-DOS derived StO_2 from the DC frequency with the SaO_2 values from the cardiac frequencies using a linear relationship (Equation 3-2) to estimate SvO_2. x-values from 0.5 to 2 were evaluated to find values that gave the best linear correlation and the best correlation to the identity line. Several illustrative examples of correlations are shown in Figure 3-14, and Table 3-2 shows the correlation parameters for a wide range of x-values.

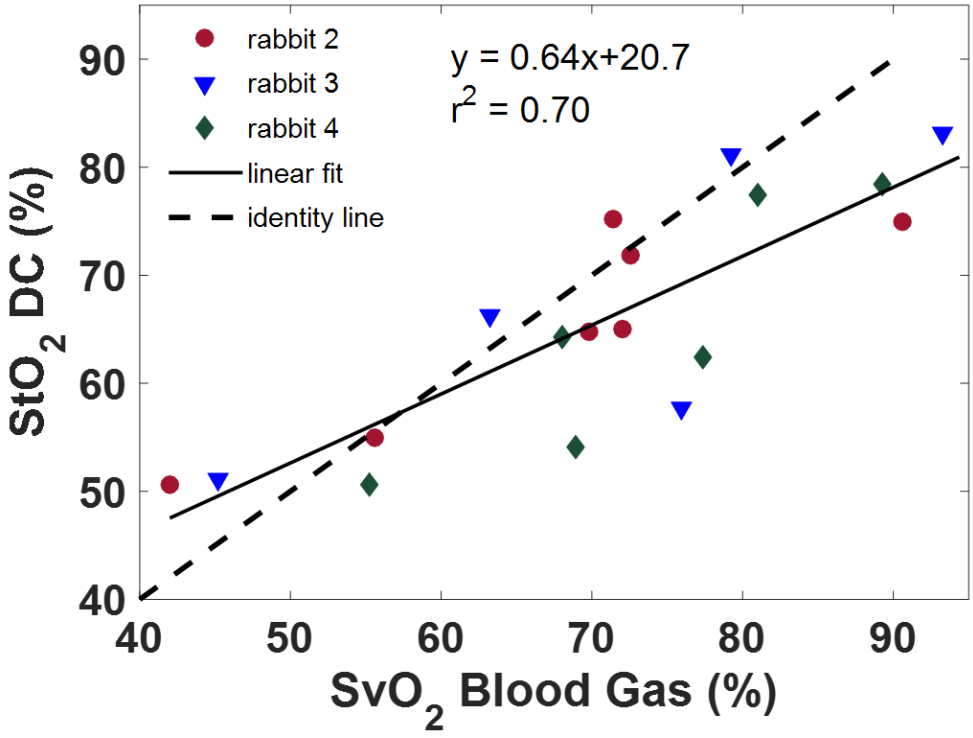

Figure 3-13. The correlation plot for DOS derived StO_2 calculated from DC compared to blood gas SvO_2 measured from invasive blood draws.

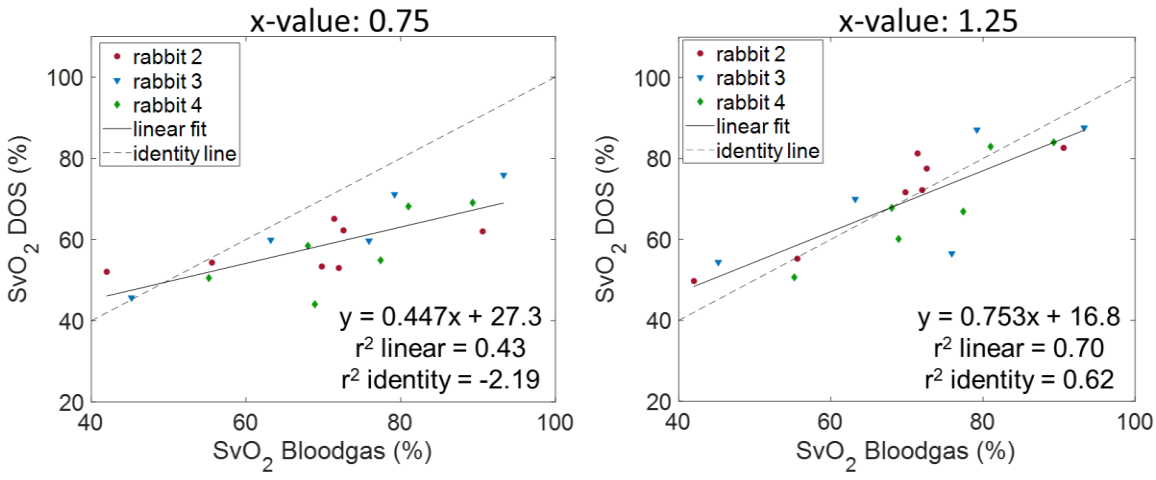

Figure 3-14. Correlation plots for DOS derived SvO_2 values calculating using the x-factor method compared to blood gas SvO_2 measured from invasive blood draws. Correlations are shown for two x-values: 0.75 and 1.25.

Table 3-2. Correlation information for a wide range of x-values comparing FD-DOS derived SvO_2 using the x-factor method to invasive venous blood draws. The numbers in red are the optimal values (e.g., highest r^2 value, lowest sum of residuals, etc.) for each column.

x-value	r^2	slope	intercept	sum of residuals to identity line	r^2 identity
0.5	0.007	0.064	40.6	485	-7.32
0.75	0.428	0.447	27.3	232	-2.19
1	0.698	0.638	20.7	131	0.269
1.1	0.702	0.690	18.9	120	0.495
1.24	0.698	0.749	16.9	112.7	0.615
1.25	0.698	0.753	16.8	113	0.619
1.38	0.690	0.797	15.3	120	0.640
1.5	0.683	0.829	14.1	126	0.632
2	0.659	0.925	10.8	158	0.535
3	0.635	1.02	7.51	215	0.384

3.4: Discussion

It was possible to extract SaO_2 trends with the custom FD-DOS system. During breath holds, both the FD-DOS and the pulse oximeter SaO_2 values tracked nicely with

each other, dropping below 90% for few seconds following a successful breath hold. However, the FD-DOS SaO_2 absolute values were typically higher than expected at baseline. SaO_2 was often greater than 100%, which is not physiological and is likely due in part to implementation of noise correction. Since SaO_2 at baseline is relatively high (~95%) and the measured blood was composed of almost entirely oxy[Hb], the μ_a cardiac peak at shorter wavelengths where deoxy[Hb] dominates (i.e., 658 and 690 nm) was often lower than the noise level, which after noise subtraction often caused slightly negative deoxy[Hb] values to be a better fit when calculating chromophores leading to SaO_2 values greater than 100%. The opposite is sometimes true without the use of noise correction. That is, the noise at the shorter wavelength was interpreted as a deoxy[Hb] signal and brought down the saturation. This trend can be seen in Figure 3-9 where many of the breath hold minimums are lower than the corresponding pulse oximeter values without noise correction. With noise correction, most of the FD-DOS values are higher than the matching pulse oximeter values. Even though there is slight discrepancy between the SaO_2 values, these results are promising. Pulse oximeters calculate SaO_2 differently than the methods shown here, often utilizing the ratio/ratio method which requires an empirical correction factor that is often proprietary [1], [49]. The fact that a similar magnitude of SaO_2 changes was seen to pulse oximetry without the use of empirical calibration or proprietary algorithms is a good sign for the FD-DOS's capability of measuring SaO_2.

Extracting SvO_2 was more challenging than SaO_2. For the healthy volunteer study, we tested the respiratory technique to extract SvO_2. Unfortunately, we could not compare it to a gold standard SvO_2 in humans since it would have required an invasive measurement

with a catheter that would cause unnecessary risk to the subjects. The respiratory signal was a difficult signal to measure in the healthy volunteers. Paced breathing at a fixed respiratory rate helped bring out this signal significantly, as seen on the right plots of Figure 3-11, but there were still inconsistencies in the signal. Previous groups encountered similar problems; one group was only able to use data from only 10 out of 22 patients citing low SNR as the main reason for these inconsistencies [32]. Furthermore, we encountered another problem in which the resulting SvO_2 values were higher than expected and only slightly lower than the SaO_2 measured at the cardiac frequencies. This was a puzzling observation, but our study had several key differences from prior work that may help to explain this result. One potential explanation is that the assumption that venous blood volume oscillates at the respiratory frequencies may not hold in all locations. We measured the fingers and thumb, which were not measured in previous studies. It is possible that some arterial blood oscillates in the fingers due to anastomoses between arteries and veins, and could affect venous blood oscillations [35]. Another possible explanation is that the fingers have a higher SvO_2 than other anatomic locations because they do not likely consume as much oxygen as other locations in the body.

Methods that extract oxygen saturation from oscillations at different frequencies (e.g., cardiac and respiratory) typically assume that blood flow contribution to the signal can be neglected. Previous work has suggested that while blood flow contribution is minimal when measuring the cardiac signal, this may not be true at respiratory frequencies in the brain [50]. Currently, it is unclear if this assumption holds for the fingers. We investigated the phase data at the cardiac frequencies during paced breathing with results

shown in Figure 3-12. This data showed that while all of the μ_a measurements at the different wavelengths were in phase, oxy[Hb] and deoxy[Hb] were approximately 180 degrees out of phase for this subject, which was a surprising finding. Additionally, the amplitude of the oscillations of μ_a at the shorter wavelengths (690 nm and especially 658 nm) were much smaller than the oscillations at the other wavelengths, and the resulting deoxy[Hb] oscillations were much smaller than oxy[Hb] oscillations. Since previous work suggests that the oscillations at the cardiac frequencies should be in phase [50], a likely explanation is that this phase flip is an artifact due to low SNR at the shorter wavelengths. When converting from absorption to chromophores using Beer's Law, if a negative value for deoxy[Hb] provides a better fit, then the phase of the deoxy[Hb] may flip, causing a ~180° phase shift (tested in simulation, data not shown). It is of note that the example shown in Figure 3-11 has one of the better (i.e. higher SNR) deoxy[Hb] signals among the data collected, and it is even more difficult to determine the phase of other deoxy[Hb] signals. Therefore, in order to determine the flow contributions of the respiratory oscillations in the finger, a higher SNR is likely necessary at the shorter wavelengths (658 and 690 nm).

To further investigate the phase difference between oxy[Hb] and deoxy[Hb], several follow-up measurements were recently taken using the box system (parameters described in chapter 4). The box system had higher SNR than the version of the cart system used to collect measurement in this chapter. An example of a thumb measurement in which oxy[Hb] and deoxy[Hb] are first in phase, and then undergo a 180° phase shift, is shown in Figures A-9 and A-10 (Appendix A-7). A further description of these measurements is

provided in the Appendix.

The rabbit study was used to test several methods for extracting SvO_2 and compare them to an invasive gold standard SvO_2 (venous blood draws). The respiratory signal was challenging to identify in the rabbit data so alternative methods were investigated. Using StO_2 as a surrogate for SvO_2 and comparing to the blood gas SvO_2 in the rabbits gave a surprising result. In general, one would expect StO_2 values to be higher than SvO_2 values since StO_2 includes some combination of both arterial and venous blood, which should have a higher oxygenation than SvO_2. However, looking at the results shown in Figure 3-13, this was not the case here. Most of these measurements had higher SvO_2 than StO_2. To explore this observation more fully, another similar method, the x-factor method was applied to the same data combining FD-DOS derived StO_2 values from the DC frequencies with SaO_2 values from the cardiac frequencies using a linear relationship (Equation 3-2) to estimate SvO_2. Given that the x-value represents the venous blood volume fraction and that prior sources have estimated this value to be between 0.6 and 0.8 in various locations in the body (see Table 3-1), one would expect that values within this range would give the best correlations to the venous blood gas measurements, however this was not the case. An x-value of 0.75 results in a correlation with an r^2 to the identity line of -2.19 which indicates that the identity line is not an appropriate fit for the data. The x-value that provided the best linear correlation was 1.10 and the x-value that provided the best correlation to the identity line was 1.38, but x-values greater than 1 do not have any physiological meaning under the current model. Values of x greater than 1 imply that more than 100% of the blood is the venous compartment, which does not make sense physiologically. There are a few possible

explanations for this puzzling result. First, it is possible that the instrumentation and signal processing methods needs to be improved to achieve a higher SNR either though improvements to the instrument or better noise correction and doing so may improve results. However, there are also potential physiological reasons for the results. Other research groups have reported that under some conditions, capillaries have lower oxygenation than larger veins [51]. Some explanations for potential reasons behind these observations include 1) arteriovenous shunts allow highly oxygenated blood to route directly into larger veins, 2) some oxygen diffusion into venules occurs from area with high PO_2, and 3) vessels with a slower blood flow, such as smaller capillaries, are likely to have a higher oxygen extraction leading to relatively lower saturation values [51]. Since capillaries are more superficial than larger vessels, they are likely contributing heavily to the absorption of the tissue being probed by NIR light. While a linear relationship that contains only SaO_2 and SvO_2 is likely a reasonable model for the hemodynamics of the entire body, this method may not be appropriate in the localized regions of tissue that are being probed by FD-DOS. Even with the low spatial resolution of FD-DOS, the region probed by the light is likely not large enough to include larger arteries and veins within a given tissue region. Therefore, a new, more complex, model that includes a capillary component may be necessary. Additionally, the model will likely have to be anatomic location specific as each location will have a different composition of arteries, capillaries, and veins all with their own location dependent oxygenations. These challenges will make it especially difficult to achieve an estimate for central SvO_2 from peripheral locations such as the fingers.

3.5: Conclusion

Our fast FD-DOS system was able to elaborate on past methods to extract SvO_2. With its increased speed, the system can extract a variety of different oxygen saturations from the cardiac and respiratory frequencies of μ_a as well as extract StO_2 from the DC frequency. One parameter that can greatly impact the resulting oxygen saturations is the measurement location, which affects the relative amounts of blood in arteries, veins, and capillaries probed. The impact of anatomic measurement location on methods to extract SvO_2 non-invasively is likely significant. We observed higher than expected SvO_2 values using the respiratory technique measured on fingers, which was a surprising result. It is unclear if volume oscillations at respiratory frequencies occur only in venous blood in all locations. Given our high saturation values on the finger, this might not be the case. Additionally, it is still unclear if there are blood flow contributions at the respiratory frequencies in the finger; a larger SNR at the shorter wavelengths is likely needed for further investigation.

Anatomic location is also critical for the using StO_2 as a surrogate for SvO_2, as well as using a linear combination of SaO_2 and StO_2. Both methods attempt to simplify SvO_2 extraction by making specific assumptions about the compositions of the blood being probed. In general, we were able to track relative changes in saturation, but the absolute values did not always match. Specifically, the x-value (venous blood volume fraction) is highly location dependent, and the model may need to be redefined to include blood from capillaries, which has a lower oxygenation than venous blood in certain situations.

Therefore, more work needs to be done to quantify the effects of location on the ability of these methods to extract SvO_2.

Finally, if peripheral measurements of SvO_2 can be consistently determined in a specific location, another potential challenge involves correlating peripheral SvO_2 to central SvO_2. Previous work has shown that these values do not always match, especially in cases of severe left heart failure and additional sepsis/septic shock [52]–[54]. Therefore, while measuring relative changes in SvO_2 is likely possible, it will likely require the additional challenge of implementing an empirical correction factor to calculate reasonable estimates for absolute central SvO_2.

CHAPTER 4: Hemodynamics of the Sternocleidomastoid Measured with Frequency Domain Near-infrared Spectroscopy Towards Non-invasive Monitoring During Mechanical Ventilation

4.1: Introduction

Mechanical ventilation (MV), which is used to assist or replace spontaneous breathing in critically ill patients, led to $27 billion in expenditures in the US in 2010, accounting for 12% of all hospital costs [55]. In that same year there were 2.7 episodes of MV per 1000 population, highlighting the enormous importance of this procedure [55]. The COVID-19 pandemic has substantially increased these numbers, although precise rates are not yet available [56]. MV is a cornerstone of critical care medicine [57], but Intensive Care Unit (ICU) stays greater than 7 days and older age are currently the best predictors of profound long-term cognitive and physical disability related to MV [58]. A key part of this problem stems from the fact that approximately 30–40% of critically ill patients in the ICU have difficulties becoming liberated from MV, accounting for ~40% of total ICU costs, and increased morbidity and mortality [58]–[60]. It is now known that inspiratory muscle dysfunction due to injury, disuse, and/or atrophy during MV plays a major role in outcomes for these patients. For example, prolonged MV is strongly correlated with dysfunction of primary (e.g. diaphragm) and accessory inspiratory muscles (e.g. sternocleidomastoid (SCM)); both have been linked to weaning failure [61]–[63]. More generally, longer ICU length of stay is in part attributable to respiratory muscle dysfunction [61], [64] and inspiratory muscle dysfunction are associated with ICU readmission [59].

MV is used, in part, to “unload”, or reduce the metabolic effort of respiratory

muscles in order to redirect oxygen delivery to vital organs. As the patients' conditions improve, key inspiratory muscles (e.g., diaphragm, scalenes, SCM, etc.) need to take over spontaneous breathing independent of the ventilator. This "reloading" is precarious due to muscle disuse atrophy, induced by unloading, compounded by oxidative stress and inflammation that accentuates their dysfunction [63], [65]. This is further complicated by other common conditions in the ICU, such as septic or cardiogenic shock, which can severely limit oxygen delivery independent of muscle status [66], [67]. Currently, there are no reliable means of establishing whether the inspiratory muscles are adequately or excessively unloaded when setting MV parameters.

Hemodynamic monitoring of the SCM may provide an important non-invasive and real-time means to monitor MV. The SCM is a muscle located in the neck and is primarily used during head movement, but also is an accessory muscle of inspiration that contributes during higher load of breathing such as those that require MV. Previous studies have shown that significant changes in oxygenation occur in the SCM during inspiratory threshold loading tests, which simulate distressed breathing [68]. Several prior works have used continuous wave near-infrared spectroscopy (CW-NIRS) techniques to measure relative changes in oxygenation of various inspiratory muscles including the SCM [68]–[73]. While CW systems are able to detect relative changes in oxygenation with an assumed differential pathlength factor (DPF), they cannot extract absolute tissue optical properties or chromophore concentrations, potentially leading to errors in estimates of muscle metabolic changes due to changes in the reduced scattering coefficient [74], [75].

FD-NIRS, also called frequency domain diffuse optical spectroscopy (FD-DOS),

uses temporally modulated light on the order of MHz to illuminate a tissue volume. The measured changes in amplitude and phase of the remitted light are used to calculate the tissue optical absorption coefficient (μ_a) and the reduced scattering coefficient (μ_s') [13]. When performed at multiple carefully chosen wavelengths, this method allows for the extraction of absolute concentrations of chromophores such as oxy and deoxyhemoglobin and myoglobin. FD-NIRS/FD-DOS has been previously used for breast cancer chemotherapy treatment monitoring [4], [5], [7], [76] and monitoring the hemodynamics of the brain [8]. There has also been prior work using FD-NIRS to measure the oxygenation of various muscles [77], [78], but to the best of our knowledge, FD-NIRS has not been used to monitor the SCM.

In this work, we first describe results from Monte Carlo simulations demonstrating that NIR light is sensitive to anticipated hemodynamic changes in the SCM. We then describe how our custom digital FD-NIRS measurement platform was adapted to provide two-wavelength high-SNR measurements of the SCM with a rapid data processing pipeline. We then describe the results of a healthy volunteer study in which subjects performed two different quasi-isometric neck flexions while monitored with FD-NIRS. Finally, we describe how FD and CS analyses of the same data set lead to different hemodynamic results, and describe the implications of this study for future work.

4.2: Methods

4.2.1: Monte Carlo Simulations

A multilayer model of the neck was created using Monte Carlo eXtreme (MCX), a Monte Carlo based photon transport simulator, in order to confirm that light from our FD-NIRS system can adequately probe the SCM [79]. The simplified multi-layer model is shown in Figure 1. The optical properties used for each layer in the simulation were estimated by using average properties found in the literature and are shown in Table 4-1 [80]–[89]. The SCM lies below two superficial layers: the skin containing the epidermis and the dermis which is typically 1-2 mm thick [90]; and the subcutaneous fat layer with a thickness that varies from person to person. The SCM itself is approximately 5 mm thick on average [91]. The tissue below the SCM contains connective tissue and other tissue types, which we simply refer to as “deep tissue”. Finally, the internal jugular vein (IJV) and the common carotid artery (CA) are deep to some parts of the SCM. Using prior work as well as our own ultrasound images, the IJV was modeled as a 5 mm radius cylinder right below the SCM and the CA was modeled as a 3.5 mm radius cylinder with the top being 3.5 mm below the SCM [92].These vessels contain a high concentration of blood, which is extremely absorbing relative to the surrounding tissue. The main absorbers of light in the near infrared wavelengths are water, lipids, hemoglobin in blood vessels, and myoglobin found in muscle cells. Since hemoglobin and myoglobin have very similar optical spectra in this wavelength range, they are difficult to separate optically and their combined concentrations will be presented as [Hb+Mb] [9].

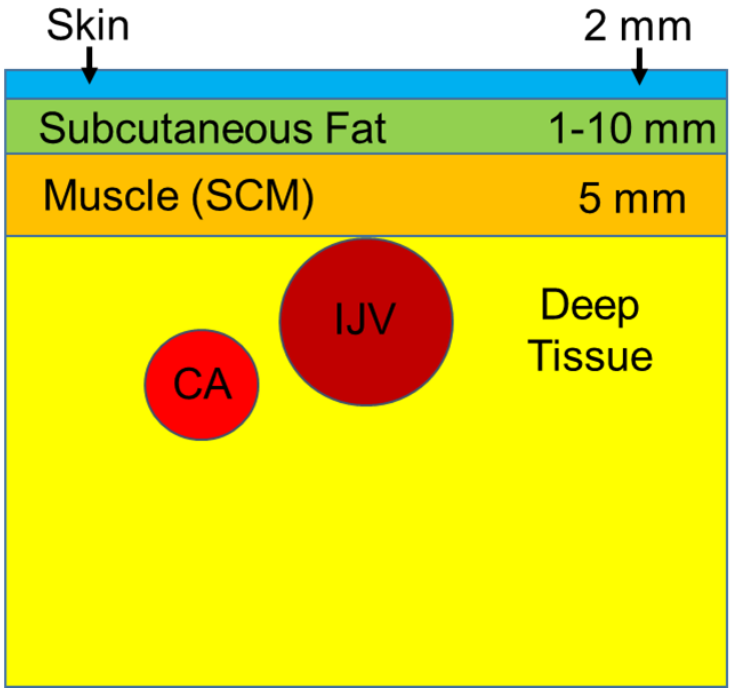

Figure 4-1. The geometry of the neck used for the Monte Carlo Simulations. The subcutaneous fat layer thickness was varied from 1- 10 mm and 3 different skin absorptions were used to simulate a variety of skin tones. The optical properties of the SCM were varied to simulate the effects of two different hemodynamic perturbations.

Table 4-1. The optical properties used for the Monte Carlo simulations at baseline. Three different optical properties were used for skin labeled skin 1 (lightest) to skin 3 (darkest). For the simulations that did not involve varying skin absorption, skin 2 optical properties were used. g is the anisotropy factor and n is the index of refraction.

Layer	μ_a (mm^{-1})		μ_s' (mm^{-1})		g		n	References
	730 nm	850 nm	730 nm	850 nm	730 nm	850 nm		
Skin 1	0.018	0.015	2.69	2.16	0.83	0.87	1.40	[80-83,85]
Skin 2	0.046	0.038	2.69	2.16	0.83	0.87	1.40	[80,81,83,85,86]
Skin 3	0.125	0.060	2.69	2.16	0.83	0.87	1.40	[80-82,85]
Fat (SubQ)	0.010	0.010	1.43	1.29	0.75	0.75	1.44	[81,82,87,88]
SCM	0.024	0.031	0.56	0.42	0.90	0.90	1.37	[81,82,84,88]
Deep Tissue	0.010	0.010	1.17	0.97	0.90	0.90	1.40	[81]
IJV	0.387	0.543	1.55	1.24	0.98	0.98	1.39	[89]
CA	0.258	0.607	1.61	1.29	0.98	0.98	1.39	[89]

The oxygen saturation (StO_2) and [Hb+Mb] of the muscle layer was varied in simulation in order to determine the optical sensitivity to hemodynamic changes in the SCM. The baseline total hemoglobin + myoglobin concentration (total[Hb+Mb]) was determined using Beer's Law by scaling previously reported muscle optical absorption values by the extinction spectrum of deoxyhemoglobin [82], [93]. This was done after subtracting the absorption due to water (assumed to be 62.5%) [85], [94]–[96]. The resulting baseline total[Hb+Mb] was 129 μM. The StO_2 at baseline was estimated to be 70%. The optical properties of the muscle layer were changed by varying both the total[Hb+Mb] as well as the StO_2. We simulated two different perturbations previously described in the literature: task failure during a neck flexion, which increased total[Hb+Mb] by 9.0 μM and decreased StO_2 by 2.03%, and task failure during an inspiratory threshold loading test, which increased total[Hb+Mb] by 20.7 μM and decreased StO_2 by 8.00 % [68]. We then calculated the difference in detected light between baseline and the two perturbations by simulating 10^9 photon packets in the Monte Carlo simulation for each scenario. The simulation outputs included the pathlength of each detected photon packet for each layer, which when weighted by the absorption coefficient (μ_a) in each layer gave the resulting detected photon weight. The overall sensitivity to the SCM was calculated by comparing the total detected photon weight of the different scenarios at 6 different source detector (SD) separations from 10-35 mm. We also investigated the effects of lipid layer thickness by varying the lipid layer from 1-10 mm and skin absorption by comparing the effects of 3 different skin absorption values found in the literature corresponding to range of skin tones [15][19].

4.2.2: Custom FD-NIRS System

We adapted our previous custom digital FD-NIRS system to take SCM measurements on the neck. A system block diagram is shown in Figure 2 and prior versions of this system are described in more detail elsewhere [17]–[19]. Briefly, direct digital synthesizers (DDS) were used to modulate two fiber coupled laser diodes at 730 and 850 nm (Blue Sky FMXL730-030YFGA, ThorLabs LP852-SF30). The lasers were modulated at 145/155 MHz respectively to allow temporal multiplexing. The detected light was measured by a fiber coupled avalanche photodiode (APD) (Hamamatsu S11519-30). The resulting signal was digitized by a 250 MHz analog to digital converter (ADC), where it was compared to a reference signal picked off from the DDS chips to determine the changes in amplitude and phase induced by the tissue. A calibration procedure was used to remove the instrument response function as previously described [18]. Amplitude and phase were computed in an Field-programmable gate array (FPGA) using the Goertzel Algorithm [33][34].

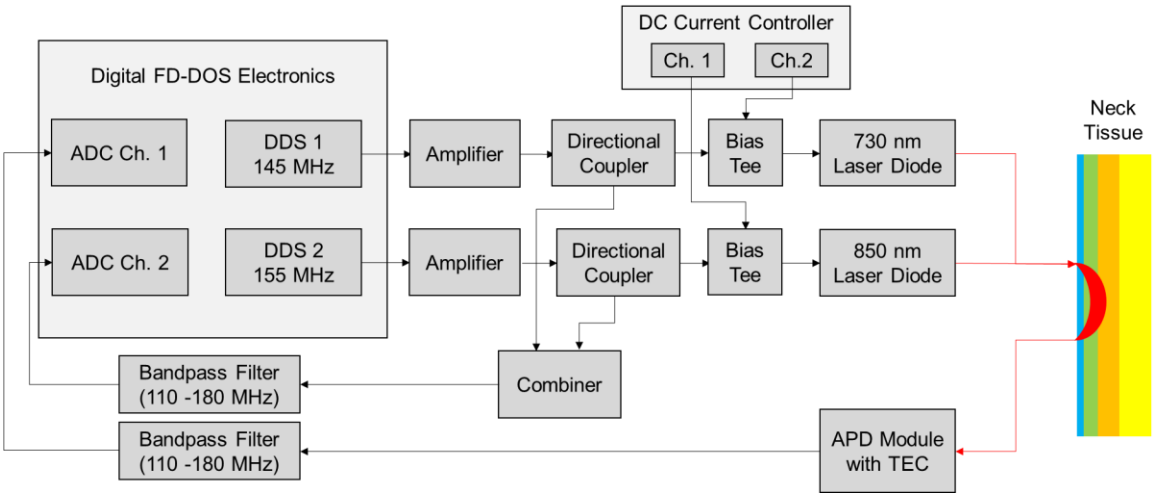

Figure 4-2. The system block diagram for our custom digital FD-NIRS system adapted for SCM measurements. DDS = Direct Digital Synthesizer, ADC = Analog to Digital Converter, APD = Avalanche Photodiode, TEC= Thermoelectric Cooler.

A number of parameters of the system were adapted in order to optimize the system for SCM measurements. Most importantly, the SCM is generally more absorbing than the tissue that has been measured previously by our system (e.g., breast, finger, forearm [18], [19], [97]), and so the system was optimized for maximum signal to noise ratio (SNR) while maintaining measurement speeds of at least 10 Hz, a rate commonly used by previous CW studies of the SCM [14][15]. The source and detector fibers were placed 25 mm away from each other, the largest source-detector separation that gave an adequate SNR through the SCM based on feasibility data. The DDS was amplified (11dBM and 1dBM for 730 nm and 850 nm respectively) to increase RF power to the lasers. A 110-180 MHz Bandpass filter was used to reduce background noise in the detected signal. Measurements were captured using 65,536 digital samples/modulation frequency, and 36 repetitions were averaged, resulting in an overall measurement rate of 10 Hz. The system SNR measured on a silicone optical phantom with similar optical properties to neck tissue (μ_a = 0.034,0.017 mm^{-1} and μ_s' = 0.51,0.50 mm^{-1} at 730, 850 nm) was 42.0 dB and 42.3 dB for 730 nm and 850 nm respectively. Both lasers' diodes were fiber coupled to 400-µm core diameter fibers bundled into a single ferrule to deliver light to the tissue. A 2.3-mm core diameter fiber bundle was used to collect remitted light. Both fibers were custom made by Fiberoptic System Inc. (Simi Valley, CA) and terminated at a right angle so they could lie flat against the neck. A custom fiber holder was 3D printed to hold the right angle source and detector fibers on the tissue.

4.2.3: Healthy Volunteer Study

FD-NIRS measurement were conducted on a group of healthy volunteers (N=10) in order to confirm the ability to measure changes in the SCM. The group of volunteers consisted of 5 males and 5 females, aged 26-38 years old. All measurements were conducted under an institutionally approved protocol (IRB 5618E). The exclusion criteria included anyone who was considered high risk for COVID-19. All participants were informed about the study virtually before consenting in person and subjected to the appropriate COVID-19 safety protocols.

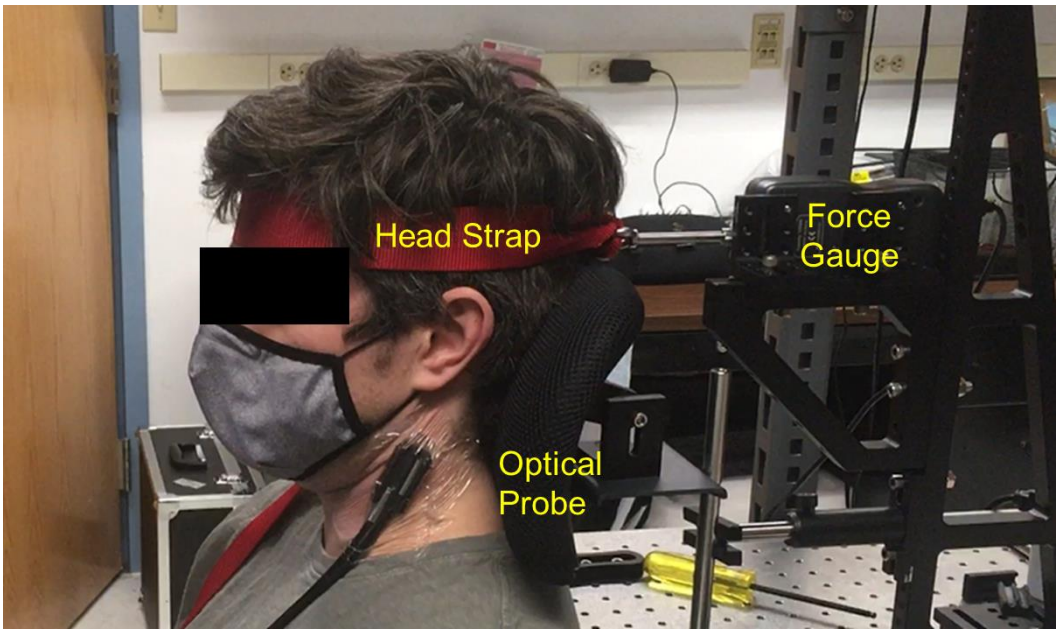

Figure 4-3. The system setup for the healthy volunteer study. The subjects performed quasi-isometric neck flexions by pushing their forehead against the head strap. A force gauge was used to measure the applied force, which was projected on a monitor in front of them.

Hemodynamic changes of the SCM were induced by performing a series of quasi-isometric neck flexions previously shown to affect the hemodynamics of the SCM [98].

The measurement setup is shown in Figure 4-3. Each volunteer was seated upright against a headrest with their forehead strapped to a force sensor (Shimpo FG-3009), which limited neck and head movement. The probe containing the source and detector fibers was placed over the skin above the SCM midway between its origin (manubrium and clavicle) and insertion (mastoid process) and secured using Tegaderm tape. In order to perform neck flexions, the subjects were instructed to push against the strap by flexing their neck at a force that was a specific percentage of their maximum force (determined at the start of the procedure). The force information was shown to the volunteer on a computer monitor in front of them. The volunteers each performed sets of sustained 30 second isometric contractions as well as repetitive intermittent isometric neck flexion contractions to more accurately simulate the muscle position/orientation as it is used during inspiration. The sets of flexion were separated by 3 minutes of rest. The sustained flexions consisted of contracting their SCM at 75% of their maximum force for a total of 30 seconds and the intermittent flexions consisted of by contracting and relaxing their SCM for 3 seconds at a time using a force of 60% of their maximum for a total of 10 minutes or until task failure. Task failure was defined as the point when the volunteer could no longer reach their target force for 3 consecutive attempts. Additionally, each subject's lipid layer thickness was measured using ultrasound (Vscan, General Electric) at the FD-NIRS measurement location.

4.2.4: Signal Processing and Data Analysis

An inverse model which utilized a Monte Carlo based Look up Table (LUT) was used to calculate μ_a and μ_s' in post processing for FD data [99]. Beer's Law was used to

calculate concentrations of oxyhemoglobin + oxymyoglobin (oxy[Hb + Mb]) and deoxyhemoglobin + deoxymyoglobin (deoxy[Hb + Mb]). A 20 % lipid fraction and 62.5 % water fraction were assumed [81], [85], [94]–[96]. At these wavelengths, water and lipid account for only a small, but measurable fraction (5-10%) of the total absorption, with the absorption due to water being an order of magnitude higher than the absorption due to lipids.

For the sustained flexions, a first order linear locally weighted scatterplot smoothing (LOWESS) filter with a 20 point (2 s) window was used in order to smooth the data. Differences in the chromophores were calculated between the onset of the flexion and maximum changes during the flexion (local maximum for deoxy[Hb + Mb] and total[Hb + Mb] and a local minimum for oxy[Hb + Mb]). Maximal points were manually selected to avoid obvious artifacts due to motion. For the intermittent flexions, a first order linear LOWESS filter with a 600 point (60 s) window was used in order to smooth the data to calculate the trend of the resulting signal while averaging the oscillations that occurs every 3 seconds while the subjects are contracting and relaxing their SCM. Oxy[Hb + Mb], deoxy[Hb + Mb], and total[Hb + Mb] were selected at three different timepoints: the onset of the flexion, the maximum of the early changes (defined as < 3 minutes after the onset of the flexion), and the end of flexion after 10 minutes or at task failure. The differences between the baseline and maximum early and late changes were also calculated. Mann-Whitney U Tests were used to compute the statistical significance of the resulting chromophore changes between males and females as well as between FD and constant scattering (significance level $p<0.05$). All data analysis and signal processing was

performed using Matlab (MathWorks, Natick, MA).

Amplitude data was also analyzed using the modified Beer-Lambert Law (equation 1) in order to compare FD results in which continuously updated μ_s' measurements are available, against a constant scattering (CS) scenario, which is often used with CW-NIRS analysis in muscle measurements studies [68]. For the CS scenario a DPF of 4 was used as in prior work [68]. Additionally, the first μ_a measurement for each experiment was used to obtain an estimate for the baseline values of the chromophores, and the modified Beer-Lambert Law was used to calculate changes in μ_a assuming a constant DPF of 4 through the experiment. Equations 4-1 and 4-2 were used to calculate $\Delta\mu_a$ as well as the DPF when it wasn't fixed. In these equations, d represents the source-detector separation (25 mm for this work).

$$\Delta\mu_a(\lambda) = \frac{1}{DPF(\lambda)*d} * ln(\frac{amp(\lambda,0)}{amp(\lambda,t)}) \quad \textbf{(4-1)}$$

$$DPF(\lambda) = \frac{1}{2}\sqrt{\frac{3\mu_s'(\lambda)}{\mu_a(\lambda)}}\left[1 - \frac{1}{(1+d\sqrt{3\mu_a(\lambda)\mu_s'(\lambda)})}\right] \quad \textbf{(4-2)}$$

4.3: Results

4.3.1: Monte Carlo Simulation Results

The two different simulated perturbations: neck flexions and an inspiratory threshold loading challenge, both resulted in a decrease of detected light at both wavelengths. A larger decrease at was observed at 730 nm compared to 850 nm due to the decrease in StO_2. Figure 4-4 shows the relative sensitivity of the SCM to the simulated

inspiratory threshold loading challenge at six source-detector separations (10–35 mm) and 10 lipid layer thicknesses (1–10 mm). In general, the sensitivity to the SCM increased as the source-detector separation increased, with longer source detector separations being more sensitive to hemodynamic changes in the SCM.

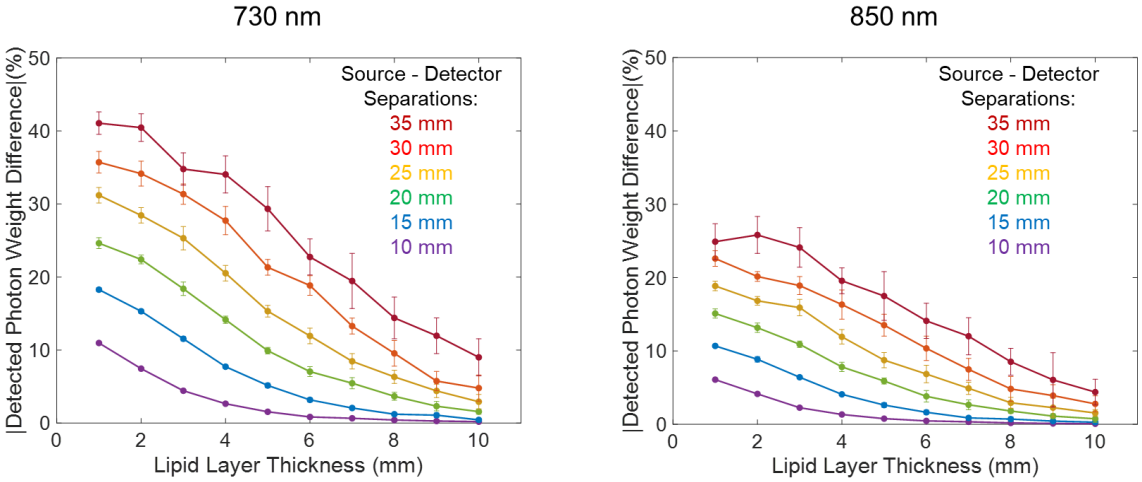

Figure 4-4. The sensitivity to a hemodynamic change in the SCM simulating an inspiratory threshold loading challenge. The simulations were run at 10 different lipid layer thicknesses (1-10 mm) and 6 different source detector separations (10–35 mm). The error bars represent the standard deviation of 10 simulations.

In general, sensitivity to the SCM decreased as the lipid layer thickness increases. Previous groups have excluded subjects with a lipid layer great than 10 mm citing a lack of SCM measurement sensitivity under those conditions [68]. These simulation results support this finding, especially for short source detector separations. The sensitivity to the perturbations were similar for the three skin absorptions tested, resulting in a less than a 3.0% difference between the 3 pairs of absorptions (see Figure A-6). However, it is important to note that the amount of detected light decreases as the skin gets more absorbing/darker results in a lower detected photon weights and lower measurement SNR,

which could make it more challenging to measure those individuals (See Figure A-7). Blood oxygenation changes of the IJV and internal CA were also tested to determine if these large vessels could affect measurements of the SCM. We found that oxygenation changes in these vessels had a minimal effect of the detected signal (<10%) for the SD separations tested and the geometry that we used (see Figure 4-1).

Based on these results, as well as the feasibility measurements described earlier, a SD separation of 25 mm was chosen for healthy volunteer measurements. This SD separation should provide substantial sensitivity to changes in expected SCM hemodynamics regardless of skin tone and for a wide range of adipose thicknesses.

4.3.2: Healthy Volunteer Study

At baseline, the average oxy[Hb + Mb] was 104.7 ± 36.3 μM, deoxy[Hb + Mb] was 56.6 ± 11.8 μM and total[Hb + Mb] was 161.4 ± 43.6 μM. Additionally baseline optical properties are shown in Table 4-S1. Large changes in the hemodynamics of the SCM were observed during flexions. Figure 4-5 shows changes in deoxy[Hb + Mb], oxy[Hb + Mb] and total[Hb + Mb] in a set of sample flexions. Figure 4-6 shows a summary of the observed changes across the group of volunteers.

For the sustained 30 second flexion, the majority of the subjects had an increase in deoxy[Hb + Mb], a decrease in oxy[Hb + Mb], and an increase in total[Hb + Mb]. The maximal change for these parameters typically occurred close to the end of the flexion. There was one subject that had an increase in oxy[Hb + Mb] during the flexion (rather than the more common decrease), and chromophore changes from the start to the end of the flexion were reported.

For the longer 10-minute intermittent flexion, there was typically a distinct early phase of hemodynamic changes that occurred within the first three minutes, followed by slower changes over the remainder of the measurement. The early changes typically presented as rapid increases in deoxy[Hb + Mb] and decreases in oxy[Hb + Mb]. The increases observed in total[Hb + Mb] are more complicated and followed one of two distinct patterns: In some subjects, the changes occurred in a sustained manner over the duration of the flexion while in others, total[Hb + Mb] reached a maximum in the early phase, similar to deoxy[Hb + Mb], followed by a gradual decrease. By the end of the intermittent flexion, deoxy[Hb + Mb] was typically higher than baseline and oxy[Hb + Mb] was typically lower than baseline, but to a lesser extent than at the early phase of the measurement. Total[Hb + Mb] typically ended higher than baseline.

Figure 4-6 also highlights the differences in the magnitude of the hemodynamic changes between males and females. The absolute changes for deoxy[Hb + Mb], oxy[Hb + Mb], and total[Hb + Mb] were approximately 2-2.5x larger in males compared to females for both sustained flexion and both early at later time points of the intermittent flexions. Statistical significance was observed in 6 out the 9 comparisons as indicated in the figure.

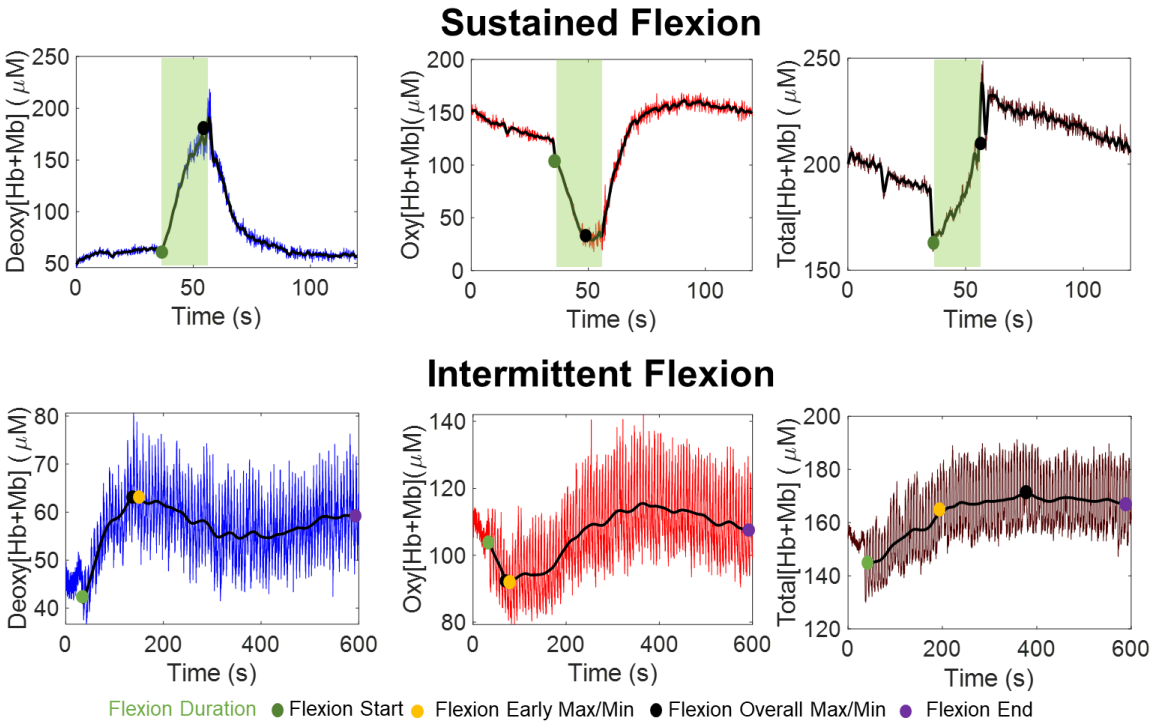

Figure 4-5. Sample chromophore data from the sustained flexions (top) and the intermittent flexions (bottom). The black line indicates the smoothed data. The colored points indicate the points of interest: the beginning of the flexion, the early maximum/minimum, and the end of the flexion.

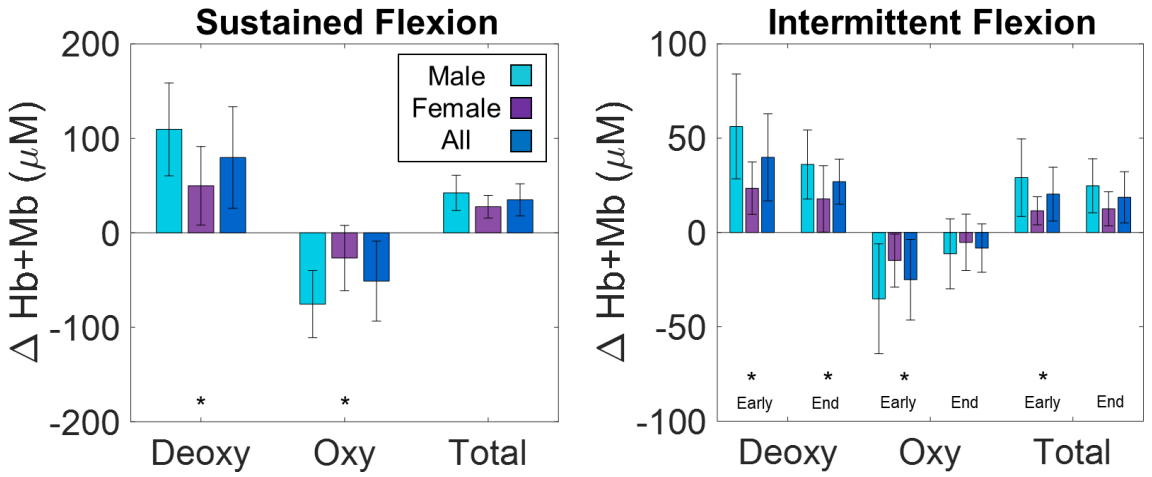

Figure 4-6. Summarized FD-NIRS results from the healthy volunteer study. The bars indicate the mean and the error bars indicate the standard deviation of the group or subset of volunteers. The asterisk indicates that the male and female values are significantly different using a Mann-Whitney U Test ($p < 0.05$).

4.3.3: Comparison between FD and CW analysis

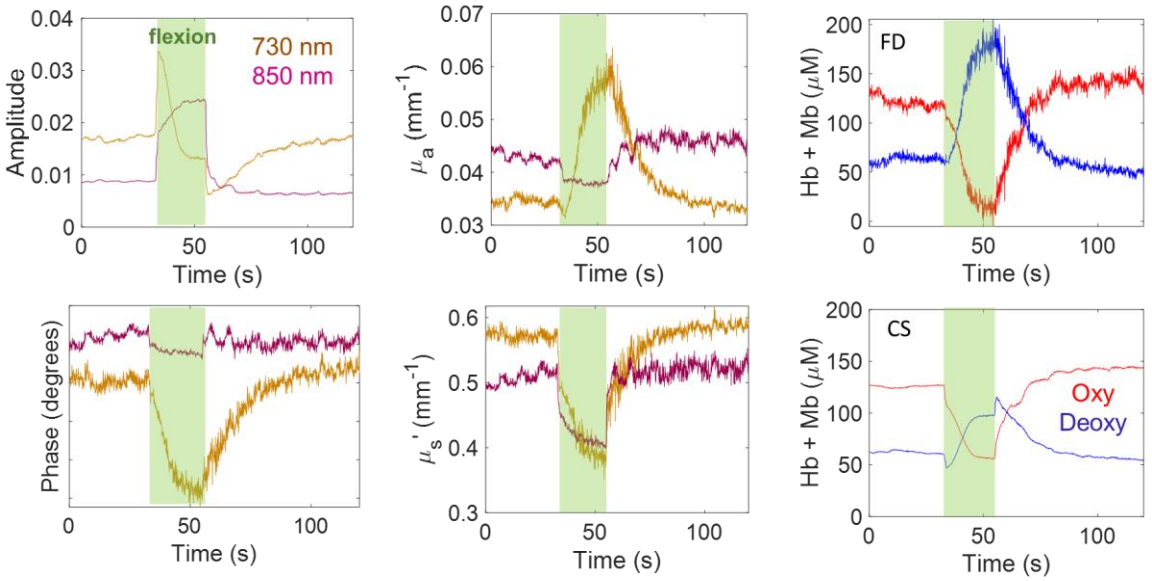

Figure 4-7. Sample amplitude, phase, μ_a and μ_s', and chromophore data from a sustained flexion. The rightmost column shows chromophore processed with FD (top) and CW (bottom).

Figure 4-7 shows an example of amplitude, phase, μ_a and μ_s' changes during a sustained flexion. Tables 4-S1 shows average changes in these parameters over all of the study subjects. In general, there were changes in both amplitude and phase, as well as μ_a and μ_s' during flexions. There were several notable differences when comparing FD and CS analyses of chromophore changes. An example of this is shown in Figure 4-7 (rightmost column), and the study averages are shown in Figure 4-8. FD analyses yielded magnitude of changes that were ~ 2–2.5x larger on average compared to CS analyses. These differences may be due in part to the observed changes in μ_s' during the flexions, which are not accounted for in the CS method, which assumes a constant DPF throughout the measurement. It is also of note that the DPF calculated using baseline FD-derived μ_a and μ_s' values was 3.28 ± 0.50 at 730 nm and 2.77 ± 0.61 at 850 nm across the study subjects.

These both differ from the assumed DPF of 4 used for CS processing [68], [69]. During the sustained flexion the DPF decreased by 0.70 ± 0.26 at 730 nm and 0.19 ± 0.39 at 850 nm.

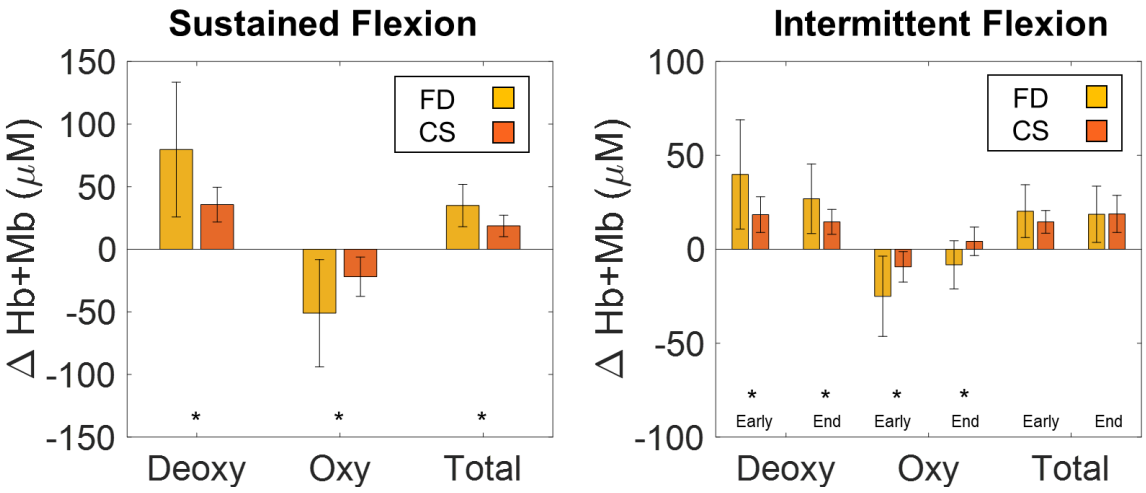

Figure 4-8. Summarized results from the healthy volunteer study comparing FD-NIRS analysis to constant scattering (CS) analysis. The bars indicate the mean and the error bars indicate the standard deviation of the group of volunteers. The asterisk indicates that the FD and CS values are significantly different using a Mann-Whitney U Test ($p < 0.05$).

4.4: Discussion

We have demonstrated here that quasi-isometric flexions of the SCM induce hemodynamic changes measurable with NIR FD-NIRS. Changes included rapid drops in oxy[Hb + Mb] and increases in deoxy[Hb + Mb] and total [Hb + Mb]. On average, these changes were larger in male volunteers than female volunteers. Additionally, FD analyses led to chromophore changes that were consistently of larger magnitude compared to CS analyses. These results help to confirm that the additional information provided by FD-NIRS could give valuable insight into the physiology of the SCM while providing more accurate measurements compared with CW-NIRS.

The MC simulation results confirmed that expected hemodynamic changes in the SCM induce large (>10%) changes in detected optical signals for SD separations of at least 25 mm. This was true up to about a 5 mm adipose layer thickness, after which changes decayed rapidly, especially for 850 nm. The average measured skin + adipose thickness for the volunteers in this study was 3.59 ± 0.74 mm, which suggests that the FD-NIRS measurements of these volunteers were likely capable of detecting SCM hemodynamic changes. Skin tone had a relatively small effect on the relative detected signal changes in simulation, but darker skin decreased the overall detected signal amplitude substantially, which is an important factor when measuring a diverse patient population. The average optical properties measured from the healthy volunteers matched well to the optical properties of the muscle layer used in the MC simulations ($\mu_s' = 0.50 \pm 0.07$ mm^{-1} in volunteers vs 0.42 mm^{-1} in simulation for 850 nm). This serves as a validation that the optical properties used in the simulations were reasonable estimates for the measured tissue and is also a good indication that detected light traveled to the muscle layer. Since the top layers (skin and subcutaneous fat) have an approximate 2.5-5x higher μ_s' than the SCM layer, one would expect the measured μ_s' to match these upper layers rather than the deeper SCM layer if there was insufficient measurement depth. We did not observe any statistically significant correlations between the measured adipose layer thicknesses and the magnitude of chromophores changes in volunteers. However, the measured volunteers were generally young (26-38 years old) and physically fit, and it is likely that inclusion of future subjects with thicker adipose layers may substantially attenuate measured SCM changes.

There were notable patterns in hemodynamic responses across subjects. For example, in the intermittent flexions, there was typically a substantial increase in deoxy[Hb + Mb] and a decrease in oxy[Hb + Mb] near the onset of the flexion. This is consistent with a rapid increase or overshoot in tissue oxygen extraction, which has been observed in prior works [9]. These changes are followed by a more gradual increase in total[Hb + Mb], an observation that is consistent with prior work that suggests a delayed increase in oxygen delivery to the muscle, likely due to the control mechanisms that the body uses to increase delivery in response to increased oxygen consumption the muscle (e.g. Increased nitric oxide signaling to trigger vasodilation) [9], [100]. It is also important to note that in some cases the measured tissue μ_s' values were less than 10x the μ_a values, which violates an assumption of the diffusion approximation [10]. For this reason, we opted to use a Monte Carlo based LUT to calculate the optical properties instead of a more traditional analytical model.

Large differences in the baseline chromophores as well as the magnitude of chromophore changes during flexions were observed between males and females. It has previously been observed that males, on average, have a higher hemoglobin content in blood measured from capillary and venous blood draws [101]. Our previous work using a similar FD-NIRS instrument has also observed large chromophore concentration difference between the sexes for bony anatomic locations [102]. One limitation of this work was a small sample size, and a larger sample size would help to better characterize these differences. Regardless, these results strongly suggest that sex is an important factor to consider in future studies.

An advantage of FD-NIRS is the ability to quantify both μ_a and μ_s'. Conversely, CW-NIRS methods typically assume constant scattering and do not consider differences in optical properties at different wavelengths, inter-subject differences, or changes in μ_s' during dynamics (see supplementary tables). We observed μ_s' changes during flexions in this study of approximately 10.9% for 730 nm and 4.6% for 850 nm. Other groups have also observed μ_s' changes during exercise in the forearms and the quadriceps [74], [75]. Additionally, these prior studies also showed that μ_s' changes affected the resulting chromophores changes. However, unlike these previous studies, we observed larger changes in oxy[Hb+Mb] and deoxy[Hb+Mb] when using FD compared to CS during flexions, which was the opposite of what was previously reported. One possible explanation of this discrepancy is the relationship between the actual measured baseline optical properties (as measured with FD-NIRS) compared to the assumed DPF for CS analysis. While this study and the prior studies all assumed a DPF of 4 for the CS method, our subjects had a measured DPF at baseline of less than 4, while the prior studies had a measured DPF greater than 4. Following the Modified Beer-Lambert Law, lower DPF values lead to larger $\Delta\mu_a$ changes and larger subsequent chromophore changes, potentially explaining why our FD data showed larger chromophore changes. Additionally, decreases in μ_s' were observed during many flexions, especially at 730 nm, which decrease the DPF even further and lead towards larger chromophore changes. The results from prior work has been mixed, but generally show slight increases in scattering after exercise which was attributed to also an increase in total[Hb + Mb], which should lead to more red blood cells in the measured volume and potentially higher μ_s' [74] as well as the accumulation of

metabolic by-products and hormones which could also increase μ_s' [74], [75], [103]. Therefore our decrease in scattering is surprising, given that we also saw an increase in total[Hb + Mb] during the same time period. Possible explanations for this discrepancy include changes in muscle configuration leading to changes in the partial volume probed by light, which mostly occurs during the onset of the flexion but can also occur during the flexion to a lesser extent. Additionally, deoxy[Hb] is slightly less scattering than oxy[Hb], which previous sources have noticed that it can in some cases counteract the increase in scattering due to the increases in total[Hb + Mb] if the decrease in saturation is significant enough [74], [89], [103]. It is also of note that the measured hemodynamic changes on healthy volunteers here was substantially larger than prior published CW measurements on the SCM [68]. For example, the average measured changes in total [Hb + Mb] were 18.6 ± 15.0 μM at the end of the intermittent flexions in this study, compared to a change of 9.0 μM for similar flexions in prior work. These differences could be due in part to differences in FD versus CW processing and the assumptions related to the DPF, as well as differences in study procedures and subject populations.

Going forward, although substantial hemodynamic changes were observed in this study using an inverse model that assumes homogeneous tissue optical properties, a multilayer inverse model accounting for skin, subcutaneous adipose tissue, and muscle may improve sensitivity to the deeper SCM tissue. Additionally, some groups have now combined FD-NIRS with Diffuse Correlation Spectroscopy to calculate a blood flow index (BF_i) and muscle metabolic rate of oxygen (MRO_2) tissue metabolism, which provide a more complete picture of muscle metabolism [77], [104], [105]. SCM measurements

would also likely benefit from this combination of techniques in future work.

4.5: Conclusion

We have shown that FD-NIRS is sensitive to hemodynamic changes in the SCM through both MC simulations and measurements on healthy volunteers. A custom digital FD-NIRS system was used to measure these changes. Although the flexions performed by the healthy volunteers may not perfectly represent the hemodynamic changes that might be present in patients that require MV, these experiments are a first step in evaluating the feasibly for using FD-DOS in the SCM Based on these results, we hypothesize that FD-NIRS measurements of the SCM may provide an important new means to monitor patients during MV, potentially assisting with guiding appropriate use and weaning from MV.

4.6: Supplementary Information

Table 4-S1. Healthy volunteer data measured at baseline. All optical values calculated using FD data.

			Baseline μ_a (mm^{-1})		Baseline μ_s' (mm^{-1})		Baseline Chromophores (μM)				Skin+Lipid Layer (mm)	DPF	
Subject	Sex	Max Force (N)	730 nm	850 nm	730 nm	850 nm	Oxy (Hb+Mb)	Deoxy (Hb+Mb)	Total (Hb+Mb)	StO_2	Ultrasound	730 nm	850 nm
1	M	103	0.026	0.035	0.62	0.55	102.5	42.6	145.1	70.6	3.78	3.57	2.93
2	M	95	0.032	0.041	0.57	0.49	119.1	55.2	174.3	68.3	3.48	3.17	2.46
3	M	94	0.034	0.041	0.53	0.46	114.3	64.1	178.4	64.0	3.40	2.94	2.43
4	M	84	0.042	0.059	0.49	0.38	189.3	62.4	251.7	75.1	2.29	2.50	1.77
5	F	95	0.024	0.026	0.6	0.54	60.9	50.5	111.4	54.6	3.95	3.75	3.89
6	F	57	0.025	0.03	0.62	0.55	81.1	48.2	129.3	62.7	3.63	3.59	3.07
7	M	178	0.041	0.049	0.47	0.38	133.8	78.5	212.3	63.0	3.67	2.56	2.01
8	F	73	0.024	0.027	0.62	0.57	61.5	52.8	114.3	53.8	3.16	3.71	3.32
9	F	79	0.035	0.04	0.56	0.52	103.4	72.0	175.4	58.9	3.28	2.96	2.57
10	F	113	0.023	0.029	0.68	0.58	81.5	40.0	121.5	67.1	5.23	4.00	3.24
Male	**Mean**	**110.8**	**0.035**	**0.045**	**0.54**	**0.45**	**131.8**	**60.6**	**192.4**	**68.2**	**3.33**	**2.95**	**2.32**
	SD	38.2	0.007	0.009	0.06	0.07	34.0	13.1	40.8	5.0	0.60	0.44	0.45
Female	**Mean**	**83.4**	**0.026**	**0.030**	**0.62**	**0.55**	**77.7**	**52.7**	**130.4**	**59.4**	**3.85**	**3.60**	**3.22**
	SD	21.4	0.005	0.006	0.04	0.02	17.5	11.8	26.1	5.6	0.83	0.39	0.48
All	**Mean**	**97.1**	**0.031**	**0.038**	**0.58**	**0.50**	**104.7**	**56.6**	**161.4**	**63.8**	**3.59**	**3.28**	**2.77**
	SD	32.6	0.007	0.011	0.07	0.07	38.28	12.48	46.0	6.80	0.74	0.52	0.64

Table 4-S2. Summary of amplitude, phase, μ_a, μ_s', and DPF changes during the sustained flexion.

		Sustained Flexion Changes									
		Amplitude (%)		Phase (deg)		μ_a (mm^{-1})		μ_s' (mm^{-1})		DPF	
		730 nm	850 nm	730 nm	850 nm	730 nm	850 nm	730 nm	850 nm	730 nm	850 nm
Males	**Mean**	**-62.1**	**-19.0**	**-4.5**	**-0.4**	**0.025**	**0.003**	**-0.090**	**-0.037**	**-0.84**	**-0.23**
	SD	12.2	14.5	0.7	0.3	0.010	0.002	0.025	0.126	0.42	0.57
Females	**Mean**	**-45.7**	**-14.7**	**-3.1**	**-0.8**	**0.011**	**0.003**	**-0.036**	**-0.008**	**-0.56**	**-0.15**
	SD	13.2	21.6	1.5	0.8	0.008	0.002	0.045	0.032	0.29	0.12
All	**Mean**	**-53.9**	**-16.9**	**-3.8**	**-0.6**	**0.018**	**0.003**	**-0.063**	**-0.023**	**-0.70**	**-0.19**
	SD	15.0	18.0	1.4	0.6	0.012	0.002	0.045	0.091	0.26	0.39

CHAPTER 5: A Miniature Frequency Domain Diffuse Optical Optode for Quantitative Wearable Oximetry.

Note: This work was published in an SPIE conference paper:

Istfan, R., LaRochelle, S., Chaudury, R., & Roblyer, D. (2019, March). A miniature frequency domain diffuse optical optode for quantitative wearable oximetry. In *Optical Tomography and Spectroscopy of Tissue XIII* (Vol. 10874, p. 108742B). International Society for Optics and Photonics. DOI: https://doi.org/10.1117/12.2509885

5.1: Disclaimer

The following work performed in chapter 5 was performed before the work performed in chapters 3 or 4. The source and detectors described here are promising, but were not optimal for use in those system. Challenges to further miniaturize FD-DOS system into a wearable remain. Specifically, there are two major challenges regarding the use of APDs as detectors. The first is temperature control especially if the APD is in direct contact with tissue. Using a proper TEC and TEC controller to control the temperature is bulky and takes up a significant amount of space, which would be challenging to implement in a self–contained wearable device. The other challenge is that the high voltage necessary for powering APDs can be a safety concern. These two reasons are the main reasons why fiber coupled source and detectors were chosen for use in chapters 3 and 4.

5.2: Introduction

The last 10 years have seen dramatic growth in both the research and consumer spaces for wearable technologies with integrated optical components, and there is a growing interest in applying these techniques for a wider range of medical diagnostic and prognostic applications [2], [3], [106]. The most common optically measured physiological signal in wearables is heart rate, measured with single wavelength photoplethysmography (PPG). Optical PPG is robust, utilizes readily available visible wavelength light emitting diodes (LEDs), and there are dedicated hardware and software solutions for minimizing motion artifact and sensor position and displacement [107]. Multi-wavelength pulse oximetry, which provides indications of arterial oxygen saturation, is also becoming increasingly available in wearable formats [108], [109]. Both optical PPG and pulse oximetry provide important and actionable biological feedback, but are generally limited in their ability to monitor all but the most superficial tissue layers, and in their ability to extract additional quantitative parameters such as total tissue oxygen saturation and absolute hemoglobin concentrations, both of which have been shown to provide relevant diagnostic and prognostic information for disease states ranging from cardio-pulmonary conditions to cancer [11]. The next generation of optical wearables will need to integrate these and other quantitative parameters in order make a substantial impact on patient outcomes.

Quantitative deep-tissue optical multi-wavelength techniques have a long history in a number of application areas, but have not yet been integrated into wearable technologies. For example, Near-Infrared Spectroscopy (NIRS) is a well-established

method for monitoring hemodynamics in the human cerebral cortex [110]. NIRS systems measure absorption changes due to local hemodynamics in the brain. Diffuse Optical Spectroscopy (DOS) is a similar technique that has been used for monitoring breast tumors [4], [5], [7], arthritis [111], peripheral artery disease [112], and others. NIRS and DOS systems generally utilize fiber-coupled near-infrared laser light sources and detectors in both reflectance and transmission geometries. These systems utilize different measurement strategies to extract different levels of quantitative information from tissue. For example, NIRS systems generally utilize continuous-wave (CW) measurements, which provide relative changes in hemoglobin concentrations over time, whereas frequency-domain (FD) and time-domain (TD) DOS systems are capable of extracting absolute optical properties and chromophore concentrations, providing opportunities to define diagnostic and prognostic thresholds [113], [114]. Both FD and TD methods have requirements that mandate high performance optical sources and detectors, representing challenges for miniaturization and portability. In this work, we focus on FD DOS as the relevant optical components are generally more amenable to miniaturization since time-correlated photon counting is not required.

FD-DOS utilizes intensity-modulated light in the RF frequency range (50 MHz - 1 GHz) to generate so-called photon density waves that travel through tissue as a coherent phase front [11]. The amplitude and phase of these photon density waves is altered by tissue, providing a means to separate the effects of absorption and scattering. Analytic and Monte-Carlo based inverse models are well described in the literature, and can be used to relate optical properties (coefficient of absorption, μ_a and the reduced coefficient of

scattering, μ_s') to changes in amplitude and phase measured at the detector [13], [14]. Absorption determined at multiple wavelengths can be used to extract chromophore concentrations using Beer's Law. The ability to accurately measure low-light levels (nW) and phase shifts with accuracy of approximately 1° is key to these measurements [115]. In the past, this has limited both the optical sources and detectors used for these systems to banks of separate fiber-coupled edge-emitting lasers and either avalanche photodiodes (APDs) or photomultiplier tubes (PMTs). These components are generally too bulky to be used for wearable probes, and incorporate high voltage (HV) supplies, external preamplifiers, thermoelectric cooling, and RF shielding that contribute to device size. There has been limited prior work in developing miniaturized FD-DOS through smaller optical sources and detectors. Several groups have explored the use of vertical cavity surface emitting lasers (VCSELs) for FD-DOS measurements, as they provide several advantages in their device size and ability to modulate at relevant frequencies [11], [116], [117]. To the best of our knowledge, there has been no prior work in exploring miniaturized high sensitivity FD-DOS detectors that could be used as part of a wearable probe. This is due, in part, to the lack of suitable detectors that meet the demands of FD-DOS, especially in compact formats. FD-DOS requires high gain (> 100) and detector sensitivity, low noise, large modulation bandwidths (i.e., up to hundreds of MHz), and linearity over a wide dynamic range to account for different tissue types. The work presented here is enabled both by alleviating detector sensitivity requirements through fiberless direct tissue contact, and by the recent development of improved detectors that combine the above features in a miniaturized format.

The goal of this work was to demonstrate the feasibility of fiberless direct tissue contact FD-DOS with components that are suitable for a highly portable and wearable probe. To accomplish this goal, a miniaturized single source-detector optode (miniOptode) was fabricated using a multi-wavelength near-infrared VCSEL and a new small format APD/transimpedance amplifier module. The performance of this miniOptode was compared to previously described fiber-based laser sources and a large active area detector [13], [17], [18]. Here we describe the miniaturized sources and detectors, the probe design, and then outline the probe testing procedure and key performance metrics based on *in vitro* and *in vivo* measurements. We conclude by describing some of the major opportunities and challenges for quantitative frequency-domain wearables.

5.3: Methods

5.3.1: MiniOptode Components

The optical source used for the miniOptode is a custom multi-element Vertical Cavity Surface Emitting Laser (VCSEL) array (Vixar Inc., Plymouth, MN), which emits light at 4 different wavelengths (660, 680, 775, 795 nm). The VCSEL package is shown in Figure 5-1a. Two elements were devoted to 660 nm and operated in parallel due to the relatively low optical power output at this wavelength. For these wavelengths, the VCSEL achieves optical powers of 1.20, 7.84, 2.24, and 1.47 mW at operating currents of 10, 15, 5, and 10 mA respectively. An advantage of this VCSEL array over commonly used edge emitting laser diodes is the single compact 5 mm TO46 packaging, which reduces overall device footprint. Additionally, prior work has demonstrated excellent modulation at

frequencies relevant to frequency-domain diffuse optics (i.e. 50 MHz – 1 GHz), and low thermal coefficients [118].

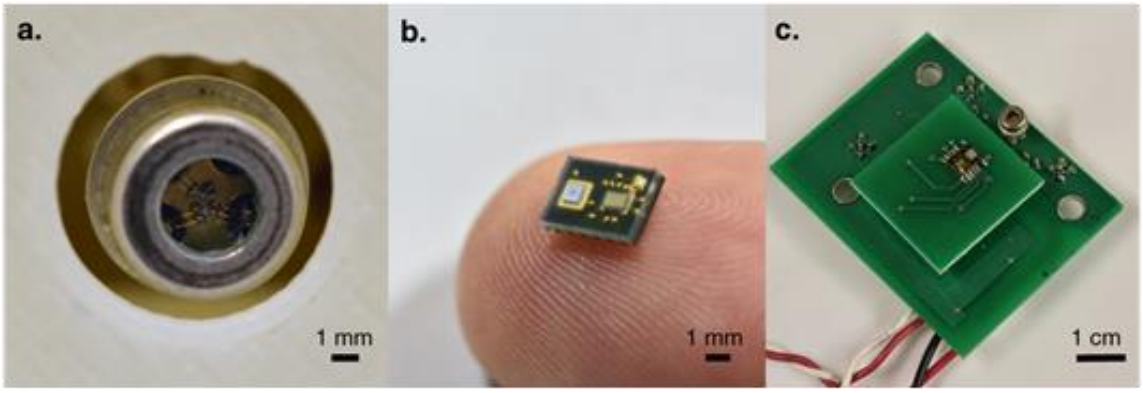

Figure 5-1. a.) The VCSEL contains five elements that emit four different near-infrared wavelengths: 660 nm, 680 nm, 775 nm, and 795 nm. b.) The APD and transimpedance amplifier are contained in a 5.3 mm x 3.0 mm x 1.2 mm surface mount package. c.) The VCSEL and APD as part of a custom designed miniaturized optode (miniOptode).

The detector utilized for this work is a newly available miniature avalanche photodiode (miniAPD) module (Hamamatsu S13282-01CR), shown in Figure 5-1b. This module contains an APD with an active area diameter of 0.2 mm and a transimpedance amplifier, both encased within a 5.3 x 3.0 x 1.2 mm surface mount package. Both the active area and overall detector package size are substantially smaller than commonly used detectors for FD-DOS. The light-collection ability of the small active area is compensated for by both direct tissue contact, as well as the integration of the transimpedance amplifier into the detector package, which reduces noise compared to external amplification. The gain of the APD is adjustable from approximately 100 to 200 depending on bias voltage and temperature, and the transimpedence amplifier provides an additional 20x gain. The typical breakdown bias voltage is 160 Volts at room temperature, and the package also requires an

additional 3.3V supply voltage.

Table 5-1. A comparison of the different commonly used avalanche photodiode detectors used in frequency domain DOS instruments. The detector used in this work was the Hamamatsu S13282-01CR, shown in the rightmost detector column.

Avalanche Photodiode		S12060-10	S6045-03	S11519-30	S3884	S13282-01CR	[unit]
QE (approx)	660nm	84	83	63	84	83	%
	680nm	84	84	63	84	86	%
	775nm	80	75	64	83	88	%
	795nm	75	73	64	82	88	%
Dark Current	Typ.	0.2	0.2	9	0.5	0.1	nA
Gain	Typ.	100-200	100-200	100-400	50-100	100-200	
Active Area (dia)		1	1	3	1.5	0.2	mm
Active Area (mm^2)		0.79	0.79	7.1	1.77	0.031	mm^2
Package		TO-18	TO-18	TO-8	TO-5	IC	
Bandwidth		600	600	230	400	180	MHz
Breakdown Voltage		200	200	350	150	160	Volts
Cost		$$	$$	$$	$$	$	
References		O'Sullivan et al. [23]	Pham et al. [16] Bevilacqua et al. [24] Yazdi et al. [25]	Jung et al. [27] Torjesen et al. [28]	Chen et al. [26]	current manuscript	

Table 5-1 shows a comparison of this APD module (right most column) to other APDs commonly used for clinical FD-DOS applications[13], [17], [18], [118]–[121]. The miniAPD has comparable or superior quantum efficiency, gain, and dark current compared to other APDs. Importantly, the overall footprint of the miniAPD was dramatically reduced compared to other APDs, which generally require external preamplification, necessitating dedicated housing modules for operation. The manufacturer specified bandwidth is smaller than other comparable APDs, with a cutoff frequency of 180 MHz, however our results demonstrate substantially larger usable bandwidth in phantom experiments (see Table 5-2 and Signal-to-Noise results in Section 5.3.1). Notably, the miniAPD was less expensive than other APDs (approximately 40 USD at the time of purchase, compared to several

hundred USD for other APDs).

5.3.2: Integration of miniOptode into an Existing FD-DOS System

Both a TEC cooled and a non-TEC cooled miniOptode were fabricated. The non-TEC cooled miniOptode is shown in Figure 5.1c, and has an overall dimensions of 6 x 4 x 1 cm. This miniOptode was designed with a smaller overall format and was used for in vivo SNR measurements. The TEC cooled version was fabricated using two custom printed circuit boards (PCBs) designed to accommodate the VCSEL array and APD separately, and was larger, with dimensions of 24 x 8 x 4 cm. The TEC-cooled miniOptode was fabricated for maximum flexibility during testing, and small format was not a goal for this design. The circuit schematic was equivalent for both miniOptodes and the SNR measured on the same phantom was within 4.1 dB for both, averaged over all modulation frequencies. The TEC-cooled miniOptode was used for accuracy, precision, linearity, thermal testing, and in vivo cuff occlusion measurements, although active cooling was used only for precision, thermal tests, and cuff measurements. The source-detector separation between the VCSEL and APD was adjustable, but for most experiments it was kept at 13 mm. For both miniOptodes, a 2 mm thick glass optical window was positioned directly above the source and the detector for in vivo measurements to provide a barrier between the electronics and optical components and the measured sample. This window helped minimize RF interference, especially when the miniOptode was placed near tissue.

The miniOptode was tested as part of a network analyzer-based FD-DOS system. The general setup of this FD-DOS system has been previously described [13], [17], [18]. Briefly, the core of the system is a network analyzer (Agilent, E5061B), which generated

RF modulation sweeps at a constant output power of 10dBm. RF signals were routed to an RF switch (Honeywell, HRF-SW1030-E) and then to a bank of four Bias-Tees (Mini Circuits, ZFBT-4R2GWX). DC current was supplied to each Bias Tee with a multi-channel current controller (ILX, LDC-3908). The output of each Bias Tee was routed to each of the four wavelength channels of the VCSEL array. A high voltage source was used to provide APD bias (Stanford Research Systems Inc., PS 325/2500V-25W). After optical detection with the APD, the resulting RF signal was routed to the second channel of the network analyzer, which computed amplitude and phase of the detected signal compared to the generated signal.

5.3.3: Calibration and Optical Property Extractions

Details of the calibration and optical property extraction methods have been previously described in detail [13]. Briefly, a silicone phantom with known optical properties was used to calibrate the system. To accomplish this, a measurement of the calibration phantom was taken and compared to the amplitude and phase predicted by a forward model of light propagation in the diffuse optical regime. A correction factor for both amplitude and phase was calculated from the difference between the measured versus predicted results, and used to remove the instrument response from subsequent measurements. For general phantom and tissue measurements, calibrated data were fit to an inverse model to extract optical properties. The forward model used was a well-described solution to the P1 approximation to the radiative transfer equation in semi-infinite homogenous geometry in the frequency domain [122]. An iterative least squares fitting algorithm was used to solve the inverse problem. For *in-vivo* measurements, Beer's

Law was used to calculate the concentrations of relevant chromophores (i.e. oxyhemoglobin and deoxyhemoglobin).

5.4: Results

An overall summary of the miniOptode performance is shown in Table 5-2. The details of each testing procedure and results are described below. For all measurements, the 4 VCSEL wavelengths (660, 680, 775, 795 nm) were swept sequentially from 50-500 MHz in increments of 1.12 MHz with a source-detector separation of 13 mm.

5.4.1: Signal-to-noise and Linearity

Signal-to-noise (SNR) measurements were conducted on a tissue-simulating phantom with an absorption coefficient of 0.0232 mm^{-1} and a reduced scattering coefficient of 0.746 mm^{-1} measured at 658 nm. For noise measurements, a highly absorbing black rubber piece was placed over the miniOptode. The SNR of the miniOptode at all 4 wavelengths was determined over a modulation frequency range of 50-500 MHz and results are shown in Figure 5-2a. A moving average filter of width 28 MHz was used to smooth the SNR data. An SNR threshold for usable bandwidth was set at 10 dB, providing an overall usable bandwidth of approximately 50 – 400 MHz for the system. At SNR values below 10 dB we have found calculated optical properties to be inaccurate. The dynamic range was determined by taking the amplitude value measured at 50 MHz on at low attenuation optical phantom (μ_a of 0.0064 mm^{-1} and μ_s' 0.5450 mm^{-1} measured at 658 nm) and comparing it to the noise floor measurement at 50 MHz. The dynamic range was determined to be 54.4 dB.

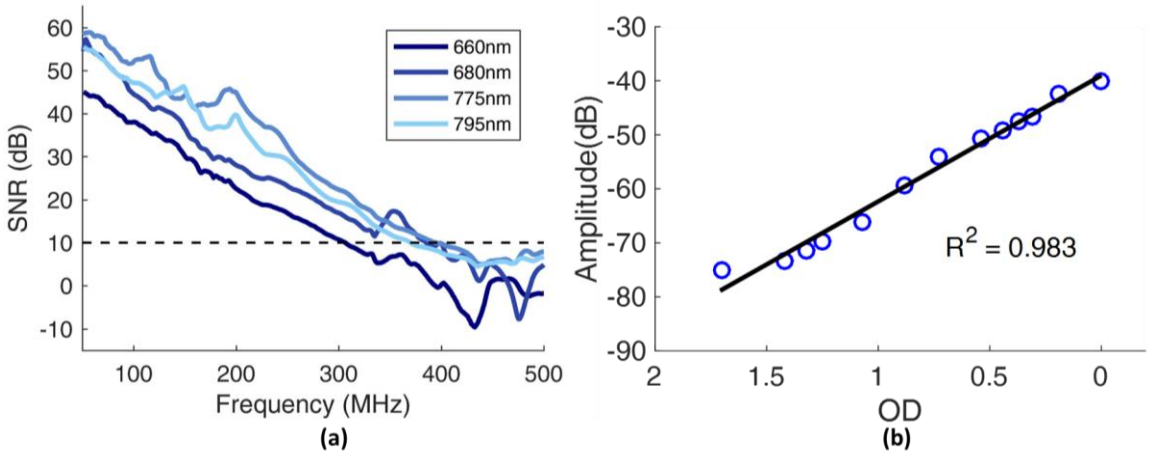

Figure 5-2. (a). The signal-to-noise ratio (SNR) of the miniOptode for each wavelength at modulation frequencies from 50 to 500 MHz. The average of 6 noise measurements were taken and smoothed using a moving average filter with a width of 25 MHz. The dashed line marks the threshold for usable bandwidth (10 dB). (b). Linearity of the miniOptode at 680 nm at a modulation frequency of 50 MHz. A set of six neutral density filters was used to alter the optical density (OD) of attenuation of light reaching the detector.

Linearity over a wide range of optical power is essential for proper calibration and optical property extractions when measuring different tissue types with different overall optical attenuation. The linearity of the miniOptode was determined by incorporating a set of neutral density (ND) filters in the path of light between the VCSEL and the phantom, altering the incident optical illumination power in a controlled manner. Six ND filters were used in combination to achieve 13 different optical densities from 0 to 2. The linearity in amplitude at 680 nm is shown in Figure 2b. Linear regression with least squares fitting was used to fit the data. The linear fit at 50 MHz averaged over all 4 wavelengths was found to have an r^2 of 0.984 and a max error of 4.53%.

5.4.2: Thermal Stability

The thermal stability of the miniOptode was measured using a tissue simulated optical phantom heated from room temperature (22°C) to skin temperature (~ 32°C) and then cooled again to room temperature. The phantom was heated by partially submerging it in a water bath warmed by a temperature-controlled heat plate. Two digital thermometer probes were positioned as close as possible to the miniOptode, and the average temperature of these two probes was used to track miniOptode temperature. After calibration, miniOptode measurements were taken every minute for 5.0 hours, and optical property extractions were calculated at each timepoint. Substantial changes in amplitude, phase, and optical properties were observed over this temperature range. Figure 5-3 shows changes in absolute amplitude and optical properties measured at 775 nm over a temperature change of one degree Celsius near room temperature. This temperature range was used to determine thermal coefficients as it matches the anticipated operating temperature in practice, and because thermal changes were linear in this range. At higher and lower temperatures, amplitude changes were large and often caused calibration and fitting algorithms to fail during optical property extractions. Table 4-2 shows the thermal coefficient of these changes averaged over all four wavelengths computed using least square fitting. This experiment was repeated by isolating the thermal response of the VCSEL and APD separately using fiber-coupled light sources and detectors as controls, and it was determined that the APD dominated the observed thermal changes.

To better control miniOptode temperature, a 16 by 16 mm thermoelectric cooler (TEC) (Thorlabs, TEC3-2.5) was positioned on the backside of the PCB, directly

underneath the APD. The TEC was adhered to the PCB using double-sided thermal tape, and a heat sink and fan were used to dissipate thermal energy. A computer-controlled TEC driver (Thorlabs, 415TE) was used to maintain a constant temperature on the cool side of the TEC of 22°C with a target temperature deviation of less than 0.1°C. The thermal stability experiment was repeated with the use of the TEC with dramatically improved results, as shown in Figure 3 and Table 2. The TEC was used for subsequent precision and *in vivo* cuff occlusion measurements.

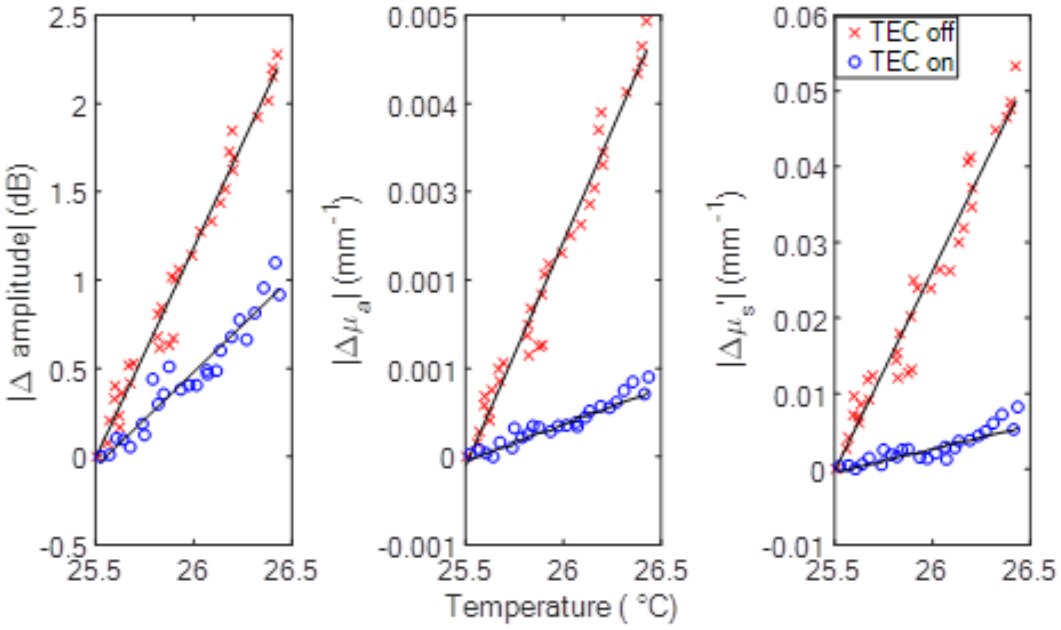

Figure: 5-3. Changes in amplitude (left), μ_a (center) and μ_s' (right) as the temperature drops one degree Celsius with and without the use of a thermoelectric cooler (TEC). Least squares fitting was used to determine the thermal coefficient.

5.4.3: Accuracy and Precision

The accuracy in optical property extractions of the miniOptode were compared to measurements taken with fiber coupled optical components. A previously validated instrument [119] with a combination of modulated laser diodes and CW white light was used to determine optical properties from 650 nm to 1000 nm in 1 nm increments. A bank of six edge emitting laser diodes at 658, 690, 785, 808, 830, 850 nm were used for FD measurements in combination with a CW broadband reflectance measurement to achieve optical property extractions at the four miniOptode VCSEL wavelengths based on a previously described method [119]. Each of the six edge emitting laser diodes was operated in a thermoelectrically cooled housing (Thorlabs, LDM9T) and fiber coupled to the sample with a 400 µm optical fiber. For these measurements, a large active area (3 mm diameter) fiber coupled avalanche photodiode (Hamamatsu, S11519-30, see Table 5-1) with a custom preamplifier module was used for FD detection. Broadband light was provided by a tungsten halogen lamp (Ocean Optics, HL-2000-FHSA) and measured with a near-infrared spectrometer (Avantes, Avaspec-HS2048).

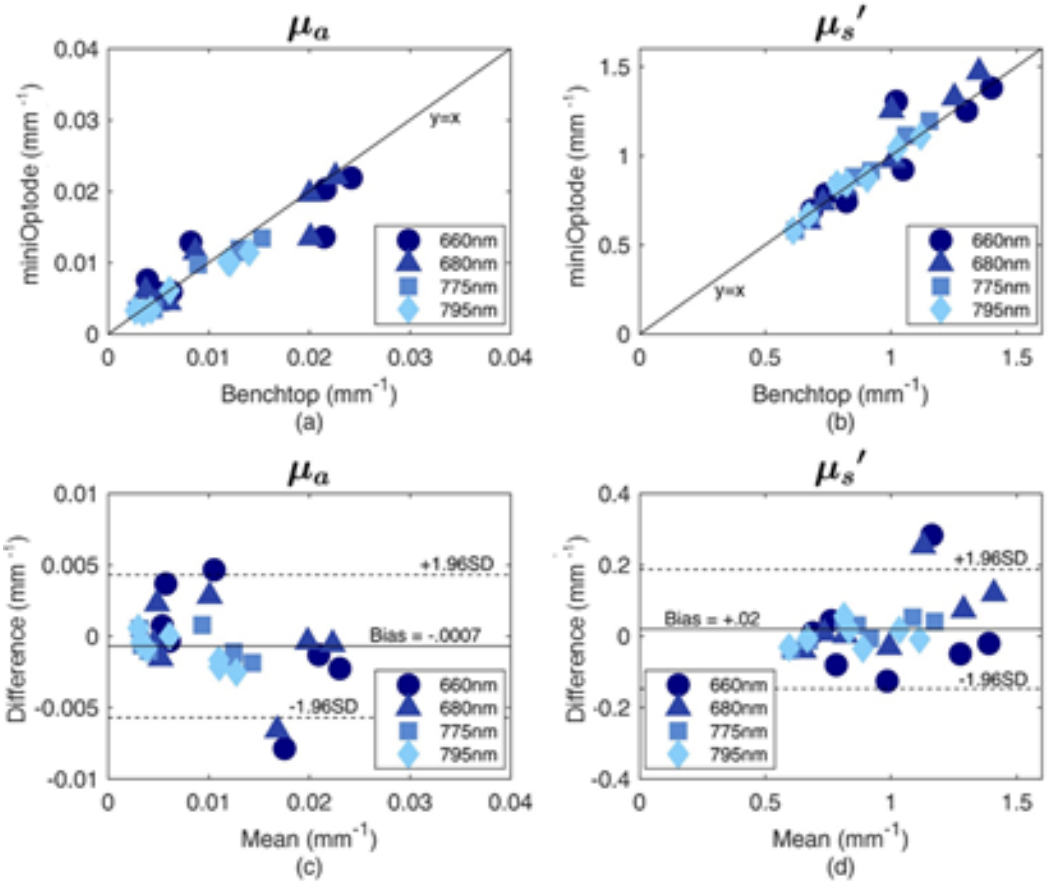

Figure 5-4. Accuracy of the miniOptode compared to the gold standard. Linearity plots are shown in (a) and (b). Bland-Altman plots are shown in (c) and (d). The average accuracy is 0.0018 mm^{-1} and 0.0547 mm^{-1} for μ_a and μ_s' respectively.

Optical property extractions with both the miniOptode and the fiber-coupled components were taken on a set of 8 silicone optical phantoms with optical properties spanning a wide range. The optical properties of both systems were compared using correlation and Bland-Altman analysis (Figure 5-4). The average accuracy, calculated as the average difference between the miniOptode and gold standard, was 0.0018 mm^{-1} and 0.0547 mm^{-1} for μ_a and μ_s' respectively (Table 5-2). The Bland-Altman plots show the differences between optical properties measured with the miniOptode and gold standard

on the y-axis versus the averaged optical properties from both systems on the x-axis. The mean biases between the systems were small, with the miniOptode estimating μ_a values with a bias of -0.0007 mm^{-1} compared to the gold standard, and μ_s' with a bias of 0.02 mm^{-1} compared to the gold standard. Together, this data indicates excellent agreement between the miniOptode and the gold standard.

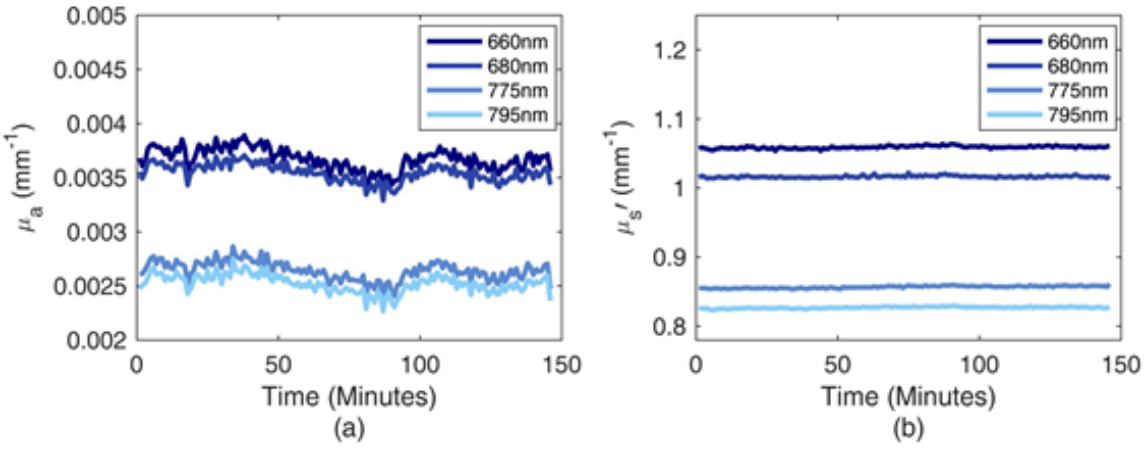

Figure 5-5. Results of a 2.5-hour drift test for absorption (a) and scattering (b). The precision, as measured as the standard deviation of the values measured over the 2.5-hour test, was 0.00008 mm^{-1} and 0.0015 mm^{-1} for μ_a and μ_s' respectively. A TEC was used to keep the temperature stable at 22°C.

The precision in optical property extractions of the miniOptode was evaluated by performing a drift test. Repeat measurements were taken on an optical phantom every 60 seconds for a total of 2.5 hours. Precision results are shown in Figure 5-5 and Table 5-2. Precision values were determined using two methods to better capture the stability of the system and the presence of outliers. The precision, as determined by the difference between the maximum and minimum values measured over the 2.5-hour test, was 0.00048 mm^{-1} and 0.0082 mm^{-1} for μ_a and μ_s' respectively. The precision, as measured as the standard deviation of the values measured over the 2.5-hour test, was 0.00008 mm^{-1} and 0.0015 mm^{-1}

[1] for μ_a and μ_s' respectively. Both of these precision metrics demonstrated a high degree of stability over time.

Table 5-2. Performance specifications of the miniOptode

miniOptode Performance Summary	
Wavelengths	660, 680, 775, 795 [nm]
Optical Power	1.20, 7.84, 2.24, 1.47 [mW]
Accuracy	μ_a: 0.0018 [mm^{-1}] (21.3%), μ_s': 0.0547 [mm^{-1}](5.71%)
Precision (max-min)	μ_a: 0.00048 [mm^{-1}] (16.1 %), μ_s': 0.0082 [mm^{-1}](0.87%)
Precision (standard deviation)	μ_a: 0.00008 [mm^{-1}] (2.94 %), μ_s': 0.0015 [mm^{-1}](0.16%)
SNR @ 50 MHz	53.5 [dB]
Dynamic Range	54.4 [dB]
Bandwidth	50 - 400 [MHz]
Linearity	r^2: 0.984, Max error: 4.53%
Thermal Stability (w/o TEC)	μ_a: 0.0038 [mm^{-1}/°C] μ_s': 0.0603 [mm^{-1}/°C]
Thermal Stability (w/ TEC)	μ_a: 0.0008[mm^{-1}/°C] μ_s': 0.0031[mm^{-1}/°C]

5.4.4: In vivo Measurements

In vivo measurements were taken on nine different anatomic sites using the miniOptode to demonstrate the versatility of the device, and to evaluate SNR for different tissues. Measurements were taken on the thumb, palm, wrist, lower arm, bicep, neck, forehead, and calf of a 35-year-old male with a source-detector separation of 10 mm. For each anatomic location, three repeat measurements were acquired, and the SNR was calculated. Table 5-3 shows the SNR and bandwidth averaged over all wavelengths. The SNR (calculated at 50 MHz) was highest on the thumb (48.5 dB) and lowest on the

forehead (29.1 dB). The bandwidth was at least 249 MHz for all measurements, demonstrating that the miniOptode can be used to collect data from a variety of anatomic locations.

Table 5-3. SNR measurements at different anatomic locations with the miniOptode.

Location	SNR at 50 MHz (dB)	Usable Bandwidth (MHz)
Forehead	29.1	249
Neck	34.2	278
Calf	34.2	286
Chest	34.6	281
Palm	36.5	314
Bicep	37.4	310
Lower Arm	40.4	356
Wrist	42.8	380
Thumb	48.5	416

A cuff occlusion test was performed to demonstrate in vivo direct tissue contact measurements during dynamic physiology. Measurements were taken on the middle finger

of the same 35-year-old male with a miniOptode source-detector separation of 10 mm. Measurements were repeated every 11 seconds. Baseline measurements were taken for 2.0 minutes, after which a sphygmomanometer cuff positioned on the upper arm was inflated to a pressure of 140 mmHg for a duration of 2.0 minutes. After release, measurements were taken for an additional 5.0 minutes during recovery. Figure 5-6 shows the hemodynamic changes during and after occlusion. As expected, oxyhemoglobin levels decrease and deoxyhemoglobin increase during occlusion, and rebound after cuff pressure release, agreeing with prior observations [18], [123].

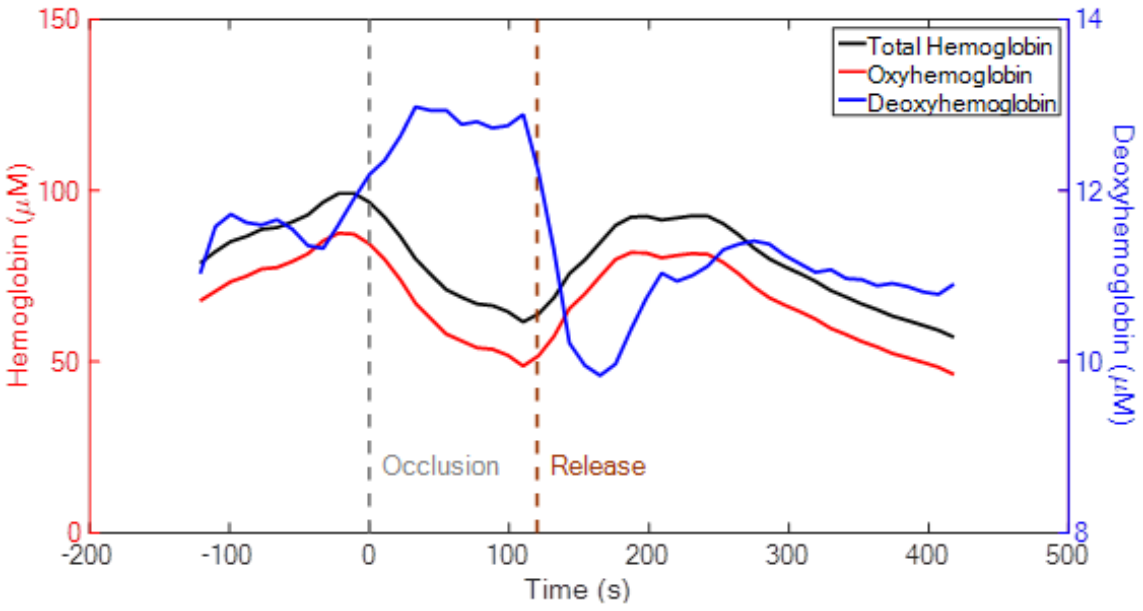

Figure 5-6. Forearm cuff occlusion test. Measurements were taken every 11s on the subject's finger. A three point moving average was used to plot the changes in each chromophore.

5.5: Discussion and Conclusions

This work demonstrates, to the best of our knowledge, the smallest FD diffuse optical optode to date. The miniOptode had high SNR, dynamic range, linearity, and when

combined with FD DOS electronics, demonstrated reasonable accuracy and precision in extraction of optical properties during direct contact (i.e., fiberless) measurements. Additionally, the miniOptode was shown to be capable of tracking in vivo hemodynamics during a cuff occlusion test. The unique combination of a multi-element VCSEL, integrated APD and transimpedance amplifier, and direct-tissue contact enabled the high performance of this device while substantially reducing overall footprint. While several technical challenges were identified, this work significantly advances FD-DOS wearables towards use for portable non-invasive in vivo monitoring.

Optical PPG and pulse oximetry are increasingly common in wearable formats, but are generally limited in their information content to heart rate and arterial oxygen saturation. Additionally, there have been a number of recent reports describing continuous wave optical wearables for cerebral monitoring [124], breast measurements [125], [126], and exercise physiology [127]. Each of these systems utilized LED illumination and simple photodiodes for detection, allowing for relatively small device footprints. Continuous wave methods, however, cannot separate absorption from scattering effects and so can only provide relative concentration changes of oxyhemoglobin, deoxyhemoglobin, and oxygen saturation based on the assumption of time-invariant scattering. This limits their ability to define quantitative diagnostic thresholds. Alternatively, in FD-DOS, absolute concentrations of oxyhemoglobin and deoxyhemoglobin are extracted, allowing measurements to be quantitatively compared over time or between patients.

Development of FD fiberless quantitative optical wearables would provide a range of opportunities for real-time monitoring of healthy and disease states that extend the

capabilities of current wearables. For example, our recent work described dynamic changes in oxyhemoglobin concentrations in breast tumors measured with clinical FD DOS which are correlated with chemotherapy response as early as 24 hours after the start of treatment [4]. FD-DOS wearables could be utilized to explore these and other timepoints during treatment, potentially providing a means to track chemotherapy response continuously, providing real-time treatment guidance. FD-DOS wearables could also find use for monitoring chronic cardiopulmonary and vascular conditions, providing actionable real-time indications of perfusion and oxygenation changes. Additionally, the miniOptode could also be used as a building block for high-density diffuse optical tomographic systems, which would provide three-dimensional depth resolved information, allowing for reconstruction of deep tissue structures including tumors.

The direct contact miniOptode presented here had largely equivalent performance, and minimal bias compared to a gold standard fiber-based system as demonstrated through Bland-Altman analysis. The accuracy of the miniOptode is comparable to other published systems using larger area detectors. For example, Pham et al. reported an accuracy of 5% and 3% for μ_a and μ_s', respectively using a 1 mm active area fiber coupled APD (S6045-03, see Table 5-1) [13]. The miniOptode system had an accuracy of 0.0018 mm^{-1} and 0.0547 mm^{-1} for μ_a and μ_s' respectively, corresponding to 21.3% and 5.71% when represented as a percentage. However, it should be noted that percent errors in μ_a extractions are highly influenced by the small absolute values of μ_a, and accuracy values in Pham et al. were reported for a μ_a range of 0.005 mm^{-1} to 0.05 mm^{-1}. If we restrict our accuracy calculations to the same range, our μ_a accuracy improves to 15.6%. Importantly,

the miniOptode was shown to provide a useable bandwidth of at least 50 to 249 MHz for nine different anatomic sites, and could be used to track dynamic physiology during a cuff occlusion. This is remarkable considering that the detector active area for the miniOptode is approximately 25 times smaller than 1 mm detectors commonly used for FD-DOS, and 230 times smaller than the 3 mm detector used for fiber-coupled gold standard measurements in this study. The small active area is compensated for by direct-tissue contact and additional preamplification of the integrated transimpedance amplifier.

Further development of miniaturized FD sources and detectors is needed to make deeper tissue FD-DOS wearables. For example, the miniOptode presented here has an SNR of 53.5 dB at 13 mm source-detector separations, but this degraded rapidly at longer separations, limiting the ability to monitor deeper tissue layers. This may require the development of larger active area detectors in package formats similar to the compact APD module used in the work. Thermal considerations are also key to stable performance for FD-DOS detectors, and the miniOptode required TEC cooling for stable in vivo measurements. While the additional TEC element and control electronics represent a possible barrier to miniaturization, the miniOptode had high performance when kept near room temperature, which minimizes power consumption and demands on the TEC.

FD-DOS measurements also require accurate measurements of amplitude and phase of photon density waves, and typically utilize analog RF electronics. Most backend electronics described in literature are relatively large, and measurements taken with the miniOptode for this work were electrically tethered to benchtop equipment, restricting subject mobility. Tethered measurements would have utility in the primary care, intensive

care, and research settings, but limit the ability of subject to travel with the probe for longer-term monitoring or sports physiology. However, recent developments by our group and others have demonstrated simpler and more compact digital FD systems [18], [19], [128], [129], and single IC FD solutions have been described, providing a potential pathway for compact and portable devices [130], [131].

In summary, this work demonstrates the performance of a new miniOptode for FD-DOS measurements. While additional developments will accelerate the adoption of robust wearable FD systems, this work provides an important step towards next generation optical wearables by demonstrating that vastly more quantitative information (e.g., optical properties and molar concentrations of hemoglobin) can be extracted from tissue using small format optical components.

APPENDIX

A.1: Silicone Optical Phantoms

A large number of silicone optical phantoms were created to mimic the optical properties of a variety of tissue types. These phantoms are the basis for testing the optical systems in the lab, including the different versions of the digital FD-DOS system. The three components of the phantom are the silicone base, titanium dioxide (TiO_2) as a scatterer, and nigrosin as an absorber. The silicone base is chosen for its chemical stability and hydrophobicity greatly extending the life of the phantom for several years. Additionally, it can be molded into a variety of shapes including rectangular slabs to model the semi-infinite geometry that is most commonly used, as well as cylinders and other more complicated geometries. Examples of phantoms are shown in Figure A-1.

In order to control the absorption and scattering of the phantom, the concentrations of TiO_2 and nigrosin can be adjusted. However, it is worth noting that the nigrosin absorption spectrum has the opposite slope compared to oxyhemoglobin from 650 - 900 nm, which is the primary absorber for the majority of tissue types in this wavelength range. As a result, these phantoms aren't a perfect replica of tissue, but they work well for testing the various instruments with optical properties that are similar to tissue. A large group of silicone phantoms with a wide range of optical properties, spanning the range of properties found in tissue were used to test all iterations of the FD-DOS system in the lab.

Figure A-1. Examples of optical phantoms that were created to test the digital FD-DOS system. The large rectangular slabs were used to test reflectance on semi-infinite media while the various other shapes (small slabs and cylinders) were used to test other geometries such as transmission.

A.2: The Effect of Probe Pressure

Probe pressure is an important parameter to consider in order to maximize the amplitude and SNR of the cardiac signal. This parameter was measured using a force sensor (Interlinks Electronics 30-49649) attached to the front of the probe and connected to voltage divider circuit to measure the variable resistance of the sensor. The circuit is shown in Figure A-2. With little to no force, the oscillations at the cardiac frequency can be difficult to observe and measure. However, if the pressure is too high, the vessels may constrict and the amplitude of the cardiac signal decreases rapidly. Therefore, there is some range of pressures that are ideal for each individual in order to maximize the amplitude and SNR of these oscillations. A series of LEDs was added to the force sensor setup as

indicators to help the healthy volunteers to stay within an ideal force range and was controlled using an Arduino. Ideal forces were often observed with pressure range of 10 - 15 kPa which corresponds to a voltage range of ~1.5 – 2.0 V under the current setup. An example of the different signals generated using a wide range of pressures is shown in Figure A-3.

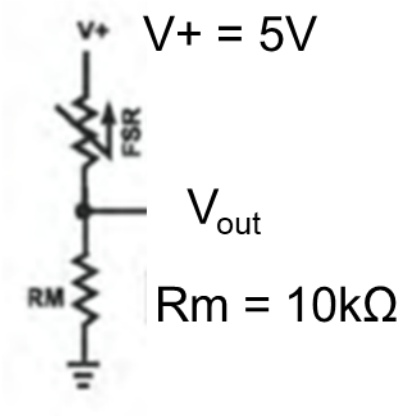

Figure A-2. A simple voltage diver circuit that was used for the force sensor. V_{out} was routed to the analog input of an Arduino where a simple program was used to turn on different color LEDs (using the digital outputs of the Arduino) to indicate whether or not the applied force was in an appropriate range to produce oscillations

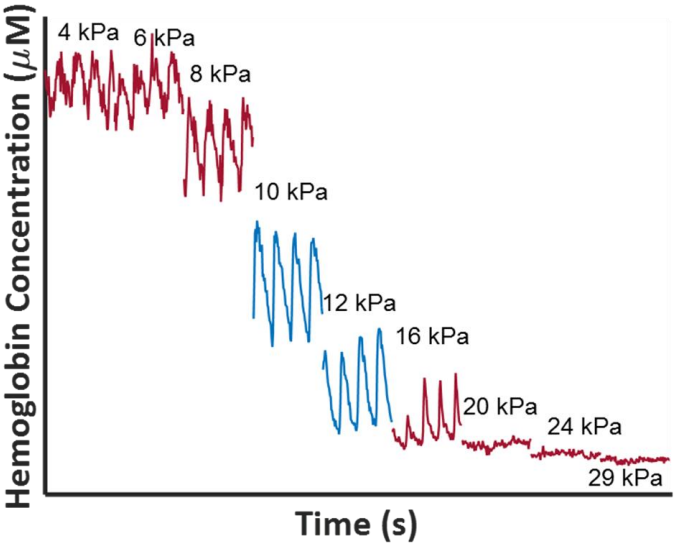

Figure A-3. The effect of probe pressure on FD-DOS measurements. Different cardiac pulse signals generated using a wide range of probe pressures on the finger. Pressures that are not too high or low give the largest sinusoidal signals.

A.3: Depth Sensitivity of the Cart System

In order to quantify the depth sensitiy of the cart system, simulations were run to calculate the photon hitting density on a point halfway between the source and detector using the standard diffusion equation (code from Virtual Tissue Simulator, Beckman Laser Instituite, UCI). The source-detector separation was 10 mm which was what was used in the healthy volunteer study and rabbit study discussed in chapter 3. The optical properies of the tissue simulated were $\mu_a = 0.019\ mm^{-1}$ and $\mu_s' = 0.95\ mm^{-1}$, and the anisotropy factor (g) = 0.9. The results are shown in Figure A-4. With these parameters, the peak depth penetration is 1.9 mm which is at a similar depth to the smaller blood vessels of the lower dermis indicating that most of the light reaches the superficial vessels while some light reaches the larger, deeper vessels.

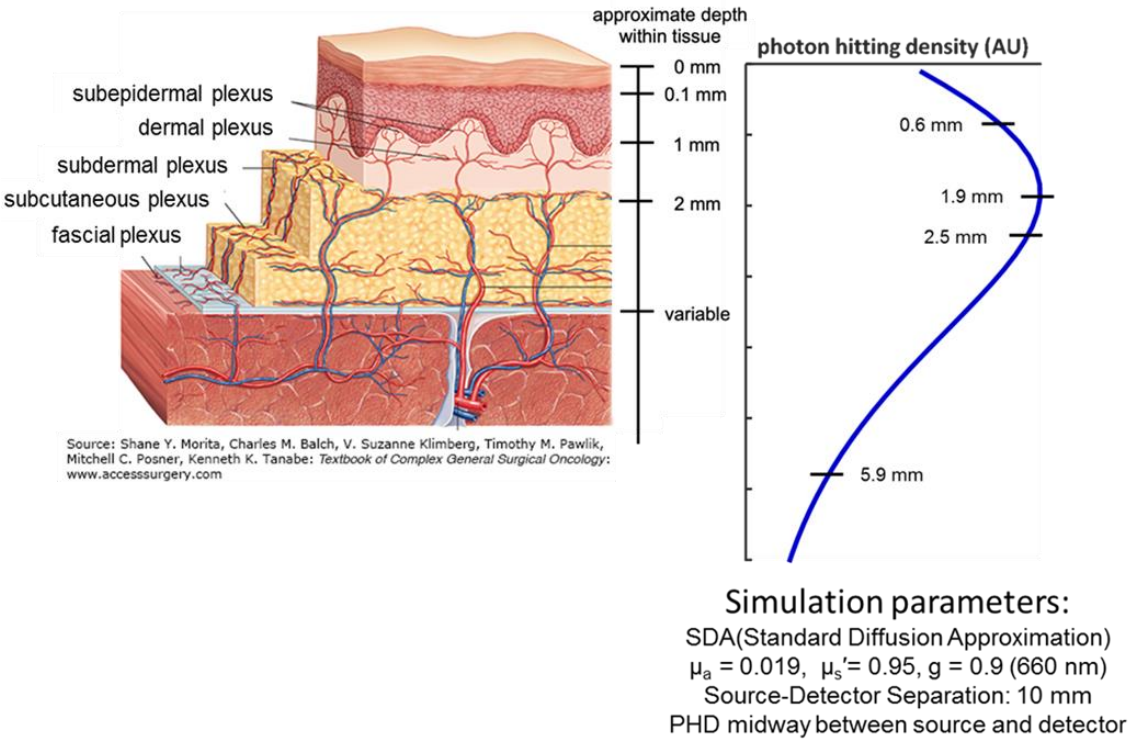

Figure A-4. (left) a schematic of the vessels beneath the skin. Source: Shane Y Morita, et. al. Textbook of complex General Surgical Oncology: www.accesssurgery.com (right) results of photon hitting density simulations. Depths are 10% = 0.6 mm, peak = 1.9 mm, median (50%) = 25 mm and 90% = 5.9 mm.

A.4: Rabbit Study: Cyanide Experiment

A cyanide experiment was performed on each rabbit (n=3) as part of the rabbit study in chapter 3. The rabbit was given cyanide at x=0 min. The rabbit was started on 100% O_2 and after 30 min the rabbit was switched to room air (21% O_2), lowering all of the resulting saturations. DOS measurements were taken every 5 min and both arterial and venous blood draws were taken at x = 10, 25, 35 minutes. An antidote was added at some later time point, and those points were not shown. The hemoglobin concentration results are shown in Figure A-5 and the oxygen saturation results are shown in Figure A-6.

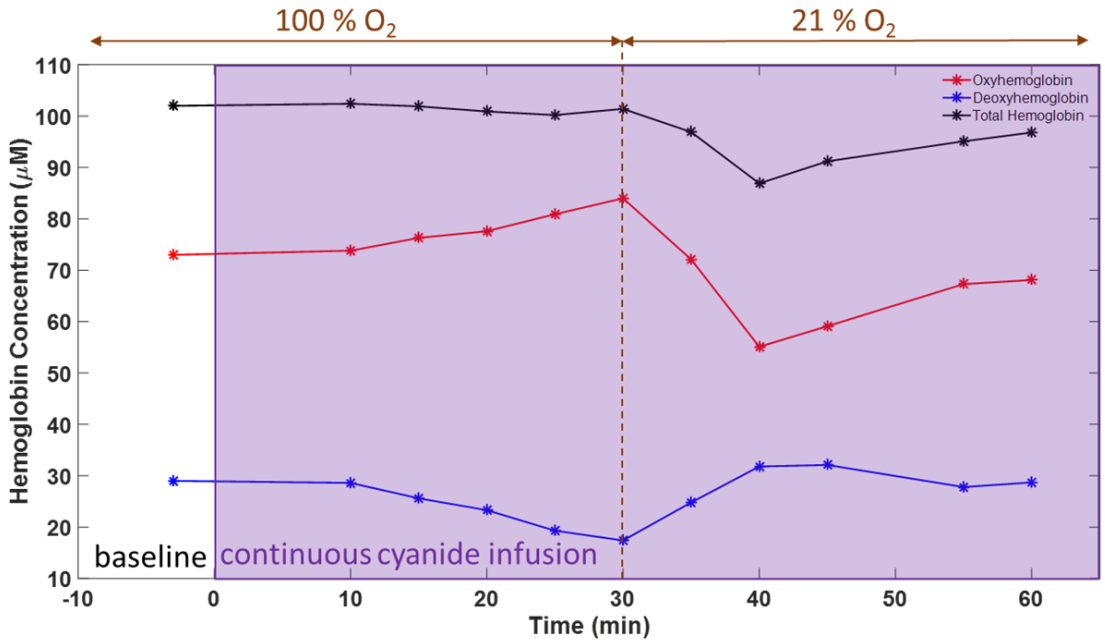

Figure A-5. Hemoglobin results of a rabbit administered cyanide. The cart FD-DOS system was used to collect these measurements.

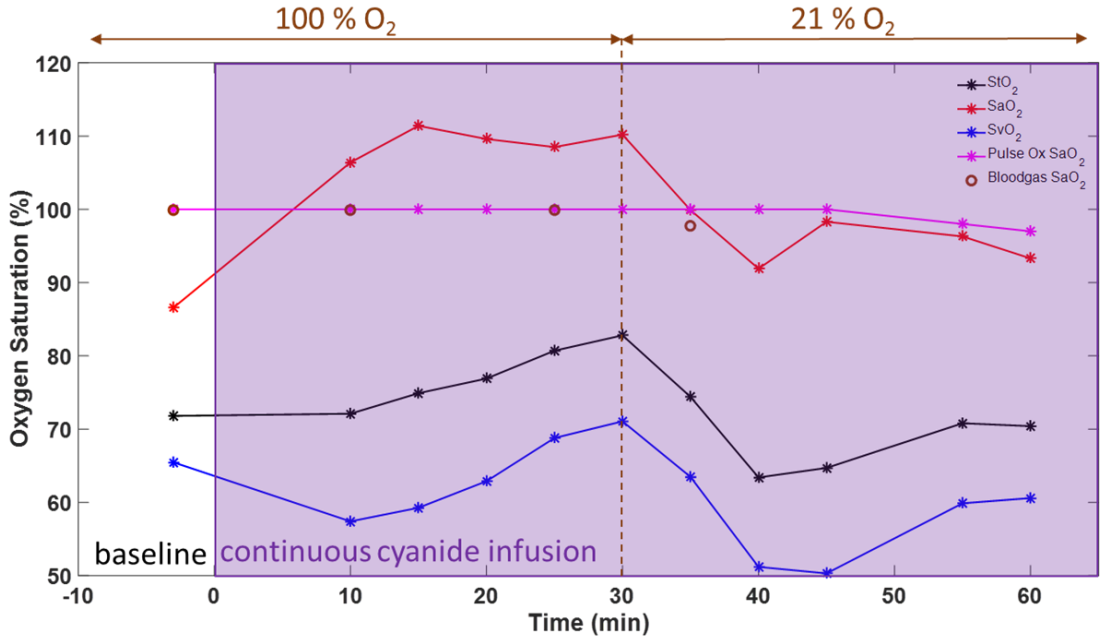

Figure A-6. Oxygen saturation results of a rabbit administered cyanide. SaO_2 was calculated using arterial frequencies, StO_2 was calculated using DC frequencies, and SvO_2 was calculated using the x-factor method where x = 0.7.

A.5: Monte Carlo Simulations of the Internal Jugular Vein

The Internal Jugular Vein (IJV) is a large vessel that runs alongside the neck to transport venous blood from the brain back into the right heart. It is fairly superficial at an average depth of ~10 mm below the surface of the skin [92]. Since this vessel is large, fairly superficial, and rich in venous blood, some groups have taken optical measurements of the area near the IJV in order to try to extract SvO_2 by using StO_2 as a surrogate for SvO_2 [37]–[39]. We performed MCX simulations to assess the sensitivity of optical measurements to changes in IJV oxygen saturation. The geometry of the simulations and the optical properties of each layer are the same as the simulations performed in chapter 4.2.1. A lipid layer thickness of 3 mm, baseline (70%) SCM saturation, and skin absorption 2 were used in the simulations (see Figure 4-1 and Table 4-1). In order to measure the sensitivity to changes in the IJV, the oxygen saturation of the SCM was varied from 70% to 50%. The overall sensitivity to the IJV was calculated by comparing the total detected photon weight of the different scenarios at 6 different source detector (SD) separations from 10–35 mm. The results are shown in Figure A-7. There is minimal sensitivity to changes in the IJV at low SD separations and only a slight sensitivity at higher SD separations where light travels deeper in tissue. Additionally, the error bars (standard deviation of 10 simulations) are large indicating that there is low amount of detected light. Since blood is very absorbing relative to tissue in NIR wavelengths, much of the light that reaches a large vessel such as the IJV is likely absorbed which reduces the sensitivity to changes in the IJV as well as the total detected light making it challenging to measure the oxygenation of the IJV. These results show a lack of sensitivity to the IJV indicating that

optical measurements are likely measuring upper layers of tissue much more than the IJV.

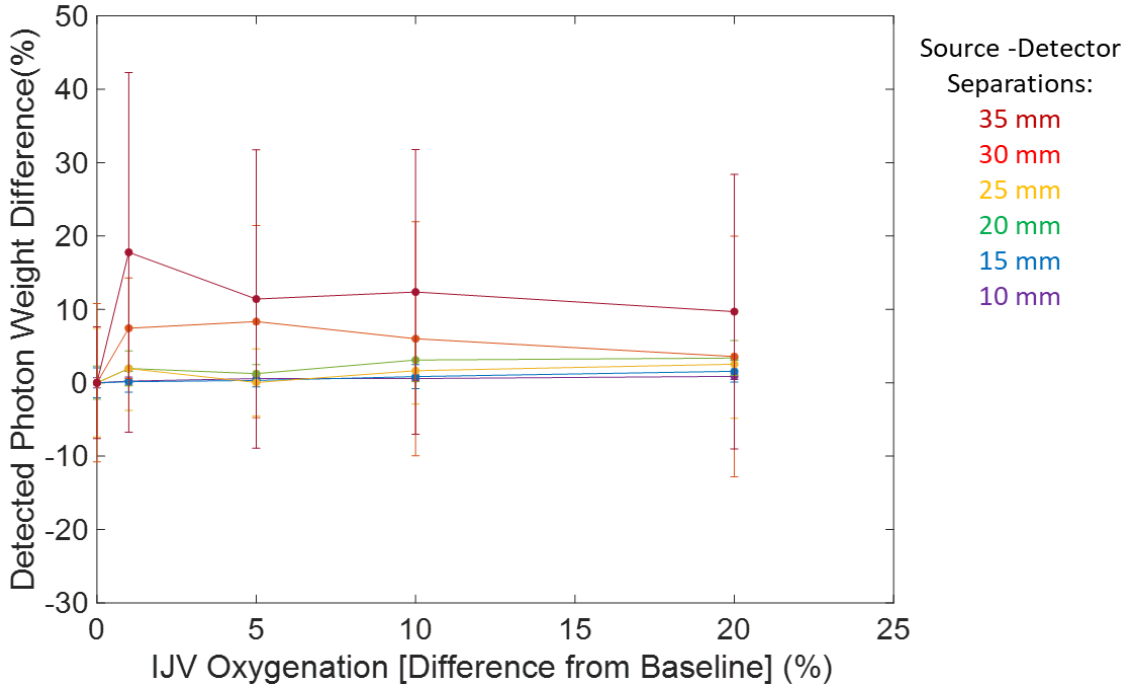

Figure A-7. Simulation results showing the sensitivity to changes in the IJV simulating a 5-20% change in oxygen saturation in the IJV. The simulations were run at 6 different source detector separations (10-35 mm). The error bars represent the standard deviation of 10 simulations.

A.6: Monte Carlo Simulations of the SCM with varying Skin Absorption

Figures A-8 and A-9 show the simulation results with different skin absorptions. The sensitivity to the perturbations were similar for the three skin absorptions tested (skin 1, skin 2, and skin 3 in Figure 4-1), resulting in a less than a 3.0% difference between the 3 pairs of absorptions. However, it is important to note that the amount of detected light decreases as the skin gets more absorbing (darker) resulting in almost an order of magnitude lower detected photon weights and lower measurement SNR. This result indicates that it is likely more challenging to measure darker-skinned individuals with FD-DOS.

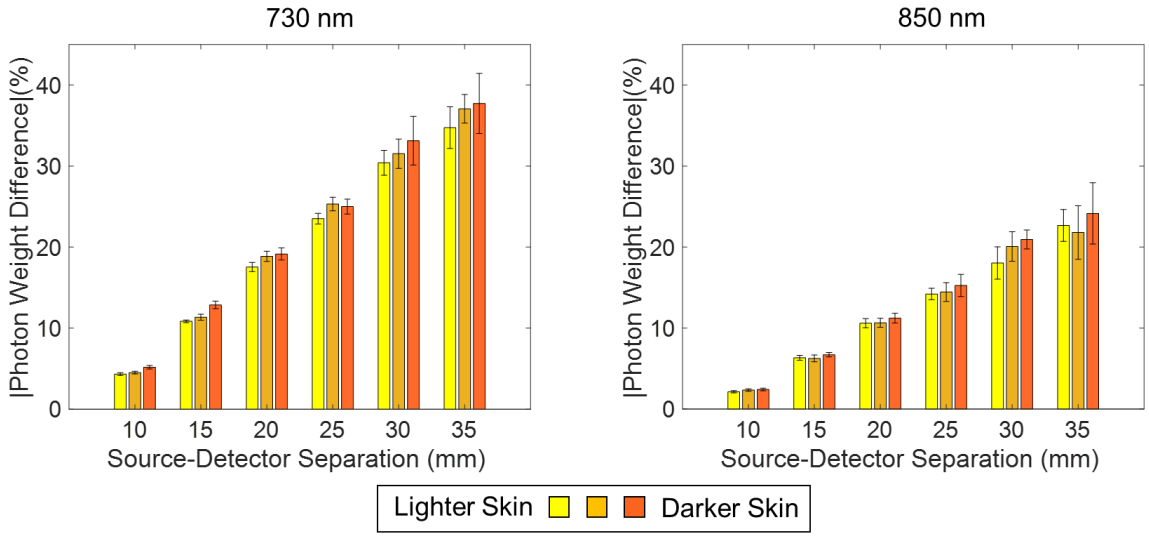

Figure A-8. The sensitivity to a hemodynamic change in the SCM simulating an inspiratory threshold loading challenge (see chapters 4.2.1 and 4.3.1). The simulations were run at 3 different skin absorptions, Skin1 –Skin3 (see Table 4.1) and 6 different source detector separations (10-35 mm). The error bars represent the standard deviation of 10 simulations.

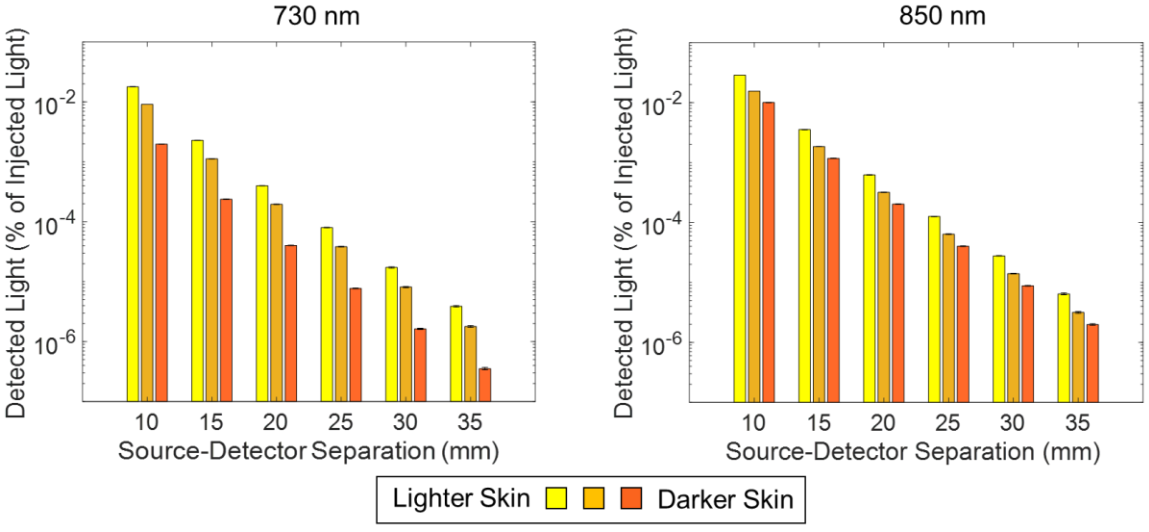

Figure A-9. The total percentage of light detected in Monte Carlo simulations of the SCM (see chapters 4.2.1 and 4.3.1). The simulations were run at 3 different skin absorptions, Skin1 – Skin3 (see Table 4.1) and 6 different source detector separations (10-35 mm). The error bars represent the standard deviation of 10 simulations.

A.7: Finger Measurements and Relative Phase of Oxy- and Deoxyhemoglobin

An updated version of box FD-DOS system (described in chapter 4) was used to acquire measurements on the thumb of a healthy subject. This system was chosen for its higher SNR compared to the cart system which was originally used to take finger measurements. Example time traces are shown in Figure A-10 and frequency domain analysis is shown in Figure A-11. This measurement is an example of an 180-degree phase shift that is sometimes observed between oxy[Hb] and deoxy[Hb] in the cardiac frequencies. During this measurement, the oxy[Hb] and deoxy[Hb] traces start out in phase at the cardiac frequency, but after 8 seconds, they become approximately 180 degrees out of phase at the cardiac frequency. In the case of the 180 degrees phase difference, Beer's law uses a negative deoxy[Hb] as the best value to fit for the resulting μ_a oscillations at the two wavelengths (730 and 850 nm). This observation is worthy of additional analysis.

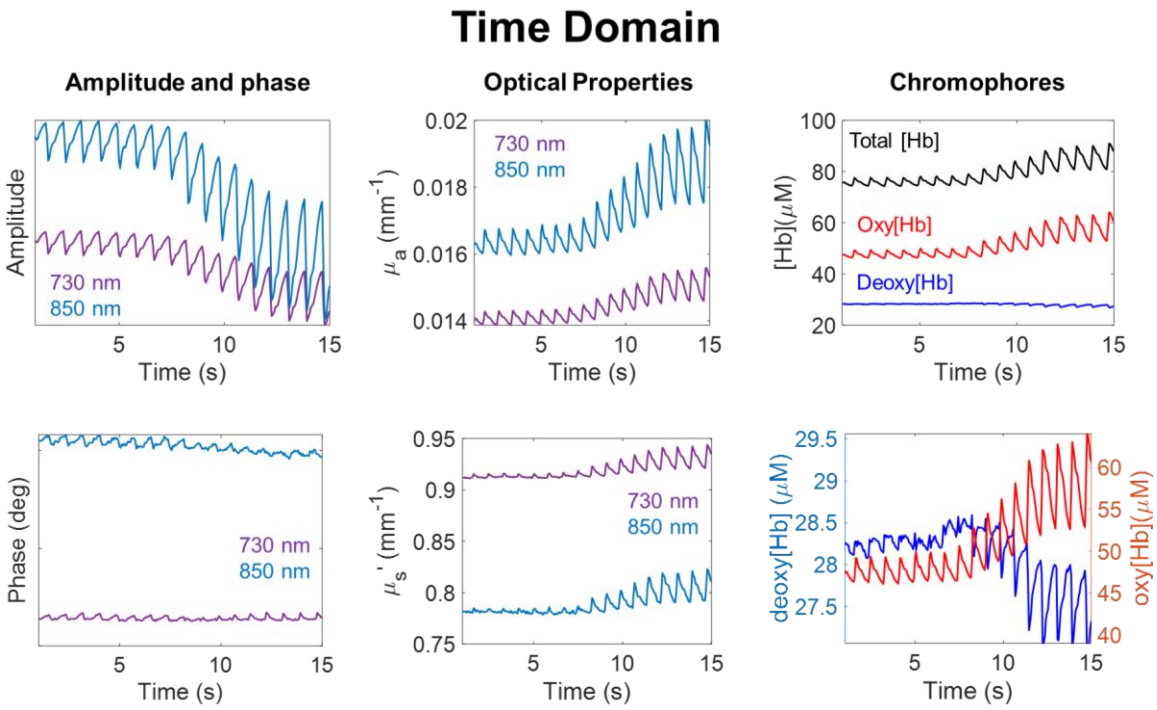

Figure A-10. Time domain data for the first 15 seconds of a finger measurement. Amplitude (top left), phase (bottom left), μ_a (top middle) μ_s' (bottom middle), oxy[Hb], deoxy[Hb], total[Hb] (right) are shown.

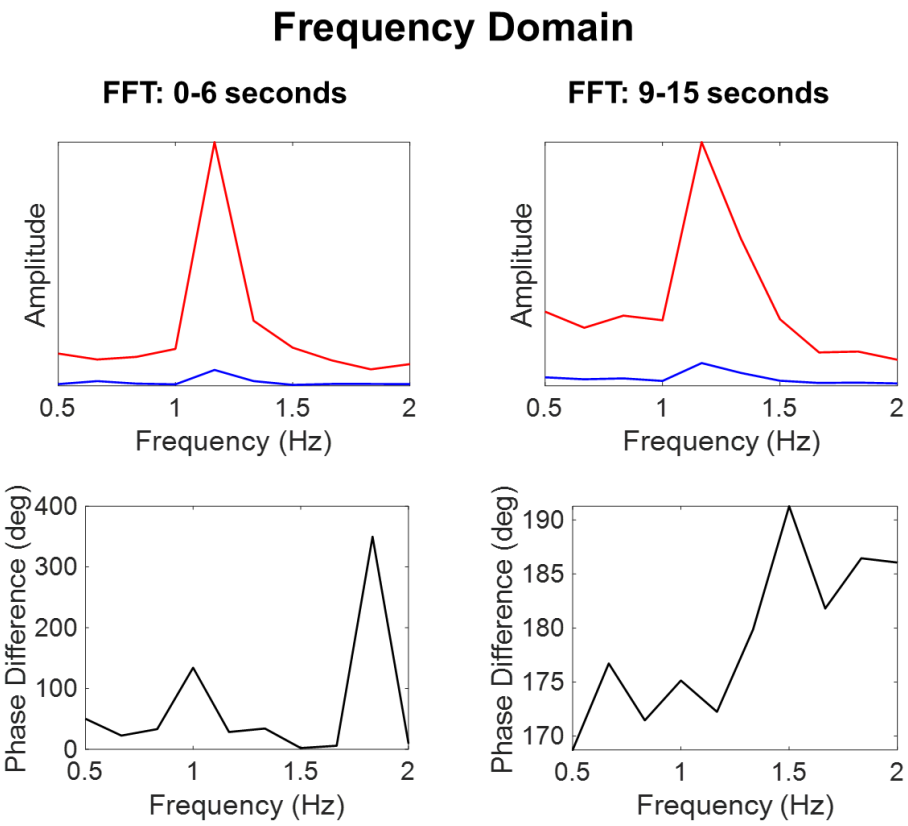

Figure A-11. Frequency domain data for two different periods from the first 15 seconds of a finger measurement. The left side shows the FFT amplitude and phase of the first 6 seconds where oxy and deoxy are in phase at the cardiac frequency, and the right side shows the FFT amplitude and phase of a later period (9-15s) where oxy and deoxy are out of phase at the cardiac frequency.

A.8: APD Preamplifier Schematic

Figure A-12 presents the schematic of the circuit that was used to amplify the signal from the 3 mm APD (Hamamatsu S11519-30). This circuit was designed, updated, and fabricated by a combination of efforts from the Tromberg Lab at the University of California, Irvine, the Roblyer Lab at Boston University (Applegate, Lin), and the Electronics Design Facility at Boston University.

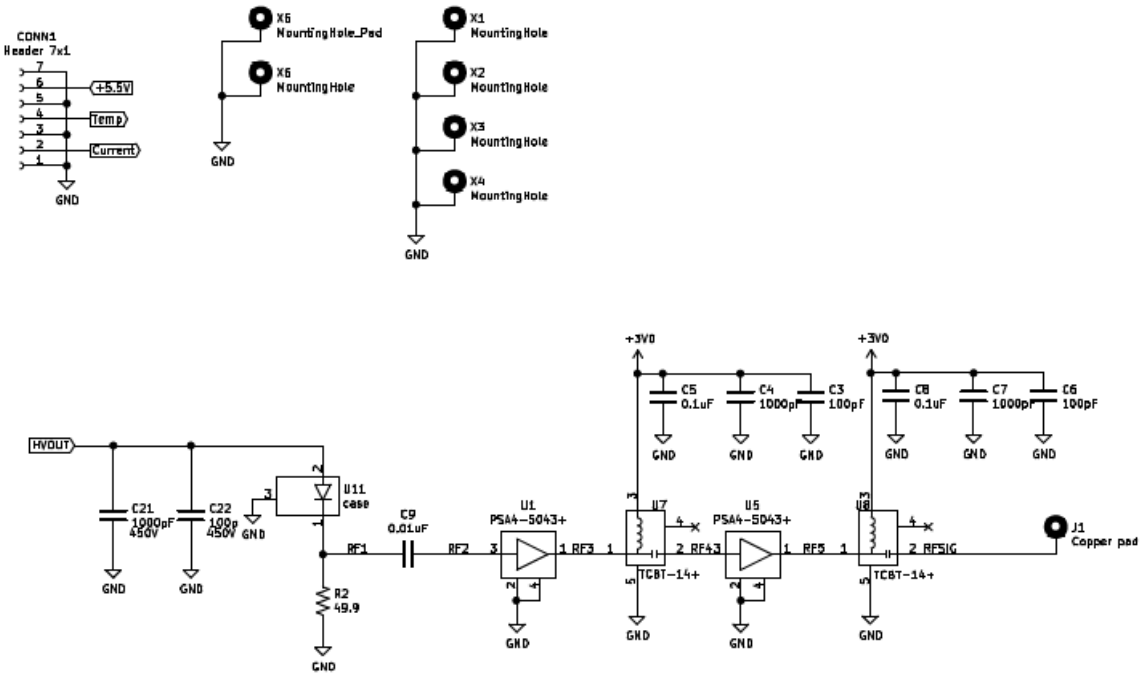

Figure A-12. The schematic of the circuit that was used the amplify the signal from the 3 mm APD (Hamamatsu S11519-30).

BIBLIOGRAPHY

[1] J. E. Sinex, “Pulse oximetry: Principles and limitations,” *American Journal of Emergency Medicine*, vol. 17, no. 1, pp. 59–66, 1999, doi: 10.1016/S0735-6757(99)90019-0.

[2] E. Gibney, “The inside story on wearable electronics,” *Nature*, 2015, doi: 10.1038/528026a.

[3] R. R. Kroll, J. G. Boyd, and D. M. Maslove, “Accuracy of a wrist-Worn wearable device for monitoring heart rates in hospital inpatients:A prospective observational study,” *Journal of Medical Internet Research*, 2016, doi: 10.2196/jmir.6025.

[4] D. Roblyer *et al.*, “Optical imaging of breast cancer oxyhemoglobin flare correlates with neoadjuvant chemotherapy response one day after starting treatment,” *Proceedings of the National Academy of Sciences of the United States of America*, vol. 108, no. 35, pp. 14626–14631, Aug. 2011.

[5] B. J. Tromberg *et al.*, “Predicting Responses to Neoadjuvant Chemotherapy in Breast Cancer: ACRIN 6691 Trial of Diffuse Optical Spectroscopic Imaging,” *Cancer Research*, vol. 76, no. 20, pp. 5933–5944, 2016, doi: 10.1158/0008-5472.CAN-16-0346.

[6] A. Cerussi, N. Shah, D. Hsiang, A. Durkin, J. Butler, and B. J. Tromberg, “In vivo absorption, scattering, and physiologic properties of 58 malignant breast tumors determined by broadband diffuse optical spectroscopy,” *Journal of Biomedical Optics*, vol. 11, 2006, doi: 10.1117/1.2337546.

[7] A. Tank *et al.*, “Diffuse optical spectroscopic imaging reveals distinct early breast tumor hemodynamic responses to metronomic and maximum tolerated dose regimens,” *Breast Cancer Research*, vol. 22, no. 1, pp. 1–10, 2020, doi: 10.1186/s13058-020-01262-1.

[8] S. Fantini and A. Sassaroli, “Frequency-Domain Techniques for Cerebral and Functional Near-Infrared Spectroscopy,” *Frontiers in Neuroscience*, vol. 14, no. April, pp. 1–18, 2020, doi: 10.3389/fnins.2020.00300.

[9] B. Grassi and V. Quaresima, “ Near-infrared spectroscopy and skeletal muscle oxidative function in vivo in health and disease: a review from an exercise physiology perspective ,” *Journal of Biomedical Optics*, vol. 21, no. 9, p. 091313, 2016, doi: 10.1117/1.jbo.21.9.091313.

[10] I. J. Bigio and S. Fantini, *Quantitative Biomedical Optics*. 2016.

[11] T. D. O'Sullivan, "Diffuse optical imaging using spatially and temporally modulated light," *Journal of Biomedical Optics*, vol. 17, p. 71311, 2012, doi: 10.1117/1.JBO.17.7.071311.

[12] A. Villringer, J. Planck, C. Hock, L. Schleinkofer, and U. Dirnagl, "Near infrared spectroscopy (NIRS): A new tool to study hemodynamic changes during activation of brain function in human adults," *Neuroscience Letters*, 1993, doi: 10.1016/0304-3940(93)90181-J.

[13] T. H. Pham, O. Coquoz, J. B. Fishkin, E. Anderson, and B. J. Tromberg, "Broad bandwidth frequency domain instrument for quantitative tissue optical spectroscopy," *Review of Scientific Instruments*, vol. 71, no. 6, pp. 2500–2513, 2000, doi: 10.1063/1.1150665.

[14] C. K. Hayakawa *et al.*, "Perturbation Monte Carlo methods to solve inverse photon migration problems in heterogeneous tissues," *Optics Letters*, 2001, doi: 10.1364/ol.26.001335.

[15] D. Roblyer *et al.*, "Optical imaging of breast cancer oxyhemoglobin flare correlates with neoadjuvant chemotherapy response one day after starting treatment," *Proceedings of the National Academy of Sciences of the United States of America*, vol. 108, no. 35, pp. 14626–14631, 2011, doi: 10.1073/pnas.1013103108.

[16] F. Bevilacqua, a J. Berger, a E. Cerussi, D. Jakubowski, and B. J. Tromberg, "Broadband absorption spectroscopy in turbid media by combined frequency-domain and steady-state methods.," *Applied Optics*, vol. 39, no. 34, pp. 6498–6507, 2000, doi: 10.1364/AO.39.006498.

[17] J. Jung, R. Istfan, and D. Roblyer, "Note: A simple broad bandwidth undersampling frequency-domain digital diffuse optical spectroscopy system," *Review of Scientific Instruments*, vol. 85, no. 7, p. 076108, Jul. 2014, doi: 10.1063/1.4890669.

[18] A. Torjesen, R. Istfan, and D. Roblyer, "Ultrafast wavelength multiplexed broad bandwidth digital diffuse optical spectroscopy for in vivo extraction of tissue optical properties," *Journal of Biomedical Optics*, vol. 22, no. 3, p. 036009, Mar. 2017, doi: 10.1117/1.JBO.22.3.036009.

[19] Y. Zhao, M. B. Applegate, R. Istfan, A. Pande, and D. Roblyer, "Quantitative real-time pulse oximetry with ultrafast frequency-domain diffuse optics and deep neural network processing," *Biomedical Optics Express*, vol. 9, no. 12, p. 5997, Dec. 2018, doi: 10.1364/BOE.9.005997.

[20] R. N. Pittman, "Regulation of Tissue Oxygenation," *Colloquium Series on Integrated Systems Physiology: From Molecule to Function*, 2011, doi: 10.4199/c00029ed1v01y201103isp017.

[21] M. Nitzan, A. Romem, and R. Koppel, “Pulse oximetry: Fundamentals and technology update,” *Medical Devices: Evidence and Research*. 2014, doi: 10.2147/MDER.S47319.

[22] R. M. Pearse and A. Rhodes, “Mixed and Central Venous Oxygen Saturation,” in *Yearbook of Intensive Care and Emergency Medicine 2005*, 2005.

[23] K. M. White, “Using continuous SVO2 to assess oxygen supply/demand balance in the critically ill patient.,” *AACN Clinical Issues in Critical Care Nursing*, 1993, doi: 10.1097/00044067-199302000-00011.

[24] F. Bloos and K. Reinhart, “Venous oximetry,” *Intensive Care Medicine*, vol. 31, no. 7, pp. 911–913, 2005, doi: 10.1007/s00134-005-2670-9.

[25] Y. Mendelson, “Pulse oximetry: Theory and applications for noninvasive monitoring,” *Clinical Chemistry*, vol. 38, no. 9, pp. 1601–1607, 1992, doi: 10.1093/clinchem/38.9.1601.

[26] J. L. Vincent, “Understanding cardiac output,” *Critical Care*, 2008, doi: 10.1186/cc6975.

[27] A. Fick, “Über die Messung des Blutquantums in den Herzventrikeln,” *Verhandlungen der Physikalisch-Medizinische Gesellschaft zu Würzburg*, Neue Folge (new series), vol. 2, pp. XVI–XVII, 1870.

[28] G. J. Dehmer, B. G. Firth, and L. D. Hillis, “Oxygen consumption in adult patients during cardiac catheterization,” *Clinical Cardiology*, 1982, doi: 10.1002/clc.4960050803.

[29] C. G. Lafarge and O. S. Miettinen, “The estimation of oxygen consumption,” *Cardiovascular Research*, 1970, doi: 10.1093/cvr/4.1.23.

[30] A. Bergstra, R. B. Van Dijk, H. L. Hillege, K. I. Lie, and G. A. Mook, “Assumed oxygen consumption based on calculation from dye dilution cardiac output: An improved formula,” *European Heart Journal*, 1995, doi: 10.1093/oxfordjournals.eurheartj.a060976.

[31] M. A. Franceschini *et al.*, “Near-infrared spiroximetry: Noninvasive measurements of venous saturation in piglets and human subjects,” *Journal of Applied Physiology*, 2002, doi: 10.1152/jappl.2002.92.1.372.

[32] J. M. Lynch *et al.*, “Noninvasive Optical Quantification of Cerebral Venous Oxygen Saturation in Humans,” *Academic Radiology*, vol. 21, no. 2, pp. 162–167, 2014, doi: 10.1016/j.acra.2013.10.013.

[33] J. Menssen, W. Colier, J. Hopman, D. Liem, and C. De Korte, “A method to calculate arterial and venous saturation from near infrared spectroscopy (NIRS),” *Advances in Experimental Medicine and Biology*, vol. 645, pp. 135–140, 2009, doi: 10.1007/978-0-387-85998-9_21.

[34] C. W. Yoxall, A. M. Weindling, N. H. Dawani, and I. Peart, “Measurement of cerebral venous oxyhemoglobin saturation in children by near-infrared spectroscopy and partial jugular venous occlusion,” *Pediatric Research*, vol. 38, no. 3, pp. 319–323, 1995, doi: 10.1203/00006450-199509000-00008.

[35] M. Nitzan, A. Babchenko, B. Khanokh, and H. Taitelbaum, “Measurement of oxygen saturation in venous blood by dynamic near infrared spectroscopy,” *Journal of Biomedical Optics*, vol. 5, no. 2, p. 155, 2000, doi: 10.1117/1.429982.

[36] T. A. Tortoriello *et al.*, “A noninvasive estimation of mixed venous oxygen saturation using near-infrared spectroscopy by cerebral oximetry in pediatric cardiac surgery patients,” *Paediatric Anaesthesia*, vol. 15, no. 6, pp. 495–503, 2005, doi: 10.1111/j.1460-9592.2005.01488.x.

[37] D. A. Colquhoun, J. M. Tucker-Schwartz, M. E. Durieux, and R. H. Thiele, “Non-invasive estimation of jugular venous Oxygen saturation: A comparison between near infrared spectroscopy and transcutaneous venous oximetry,” *Journal of Clinical Monitoring and Computing*, vol. 26, no. 2, pp. 91–98, 2012, doi: 10.1007/s10877-012-9338-0.

[38] T. Li, M. Duan, K. Li, G. Yu, and Z. Ruan, “Bedside monitoring of patients with shock using a portable spatially-resolved near-infrared spectroscopy,” *Biomedical Optics Express*, vol. 6, no. 9, p. 3431, 2015, doi: 10.1364/boe.6.003431.

[39] Z. S. Ruan *et al.*, “Monitoring tissue blood oxygen saturation in the internal jugular venous area using near infrared spectroscopy,” *Genetics and Molecular Research*, vol. 14, no. 1, pp. 2920–2928, 2015, doi: 10.4238/2015.March.31.23.

[40] D. M. Hueber *et al.*, “Non-invasive and quantitative near-infrared haemoglobin spectrometry in the piglet brain during hypoxic stress, using a frequency-domain multidistance instrument,” *Physics in Medicine and Biology*, vol. 46, no. 1, pp. 41–62, 2001, doi: 10.1088/0031-9155/46/1/304.

[41] P. B. Benni, D. MacLeod, K. Ikeda, and H. M. Lin, “A validation method for near-infrared spectroscopy based tissue oximeters for cerebral and somatic tissue oxygen saturation measurements,” *Journal of Clinical Monitoring and Computing*, vol. 32, no. 2, pp. 269–284, 2018, doi: 10.1007/s10877-017-0015-1.

[42] C. Blakemore and S. Jennett (eds.), *The Oxford Companion to the Body*. Oxford University Press, 2001.

[43] S. Elad, David Einav, “Physical and Flow Properties of Blood,” in M. Kutz (ed.) *Standard Handbook of Biomedical Engineering and Design*, McGraw-Hill Companies, Inc., 2004.

[44] R. Boushel, H. Langberg, J. Olesen, J. Gonzales-Alonzo, J. Bülow, and M. Kjær, “Monitoring tissue oxygen availability with near infrared spectroscopy (NIRS) in health and disease,” *Scandinavian Journal of Medicine and Science in Sports*, 2001, doi: 10.1034/j.1600-0838.2001.110404.x.

[45] V. Pollard, D. S. Prough, A. Eric DeMelo, D. J. Deyo, T. Uchida, and H. F. Stoddart, “Validation in volunteers of a near-infrared spectroscope for monitoring brain oxygenation in vivo,” *Anesthesia and Analgesia*, vol. 82, no. 2, pp. 269–277, 1996, doi: 10.1097/00000539-199602000-00010.

[46] H. M. Watzman, C. D. Kurth, L. M. Montenegro, J. Rome, J. M. Steven, and S. C. Nicolson, “Arterial and venous contributions to near-infrared cerebral oximetry,” *Anesthesiology*, 2000, doi: 10.1097/00000542-200010000-00012.

[47] G. I. Mchedlishvili, *Arterial behavior and blood circulation in the brain*. Plenum Publishing Corporation, 1986.

[48] D. T. Delpy, M. Cope, P. Van Der Zee, S. Arridge, S. Wray, and J. Wyatt, “Estimation of optical pathlength through tissue from direct time of flight measurement,” *Physics in Medicine and Biology*, 1988, doi: 10.1088/0031-9155/33/12/008.

[49] J. F. Kelleher, “Pulse Oximetry,” *Journal of Clinical Monitoring*, vol 5, no. 1, pp. 37–62, 1989, doi: 10.1007/BF01618369.

[50] J. M. Kainerstorfer, A. Sassaroli, and S. Fantini, “Optical oximetry of volume-oscillating vascular compartments: contributions from oscillatory blood flow,” *Journal of Biomedical Optics*, vol. 21, no. 10, p. 101408, 2016, doi: 10.1117/1.jbo.21.10.101408.

[51] S. Sakadžić *et al.*, “Large arteriolar component of oxygen delivery implies a safe margin of oxygen supply to cerebral tissue,” *Nature Communications*, vol. 5, 2014, doi: 10.1038/ncomms6734.

[52] M. Podbregar and H. Možina, “Skeletal muscle oxygen saturation does not estimate mixed venous oxygen saturation in patients with severe left heart failure and additional severe sepsis or septic shock,” *Critical Care*, vol. 11, no. 1, pp. 1–8, 2007, doi: 10.1186/cc5153.

[53] H. Možina and M. Podbregar, “Near-infrared spectroscopy during stagnant ischemia estimates central venous oxygen saturation and mixed venous oxygen saturation

discrepancy in patients with severe left heart failure and additional sepsis/septic shock," *Critical Care*, vol. 14, no. 2, 2010, doi: 10.1186/cc8929.

[54] S. J. Shepherd and R. M. Pearse, "Role of central and mixed venous oxygen saturation measurement in perioperative care," *Anesthesiology*, vol. 111, no. 3, pp. 649–656, 2009, doi: 10.1097/ALN.0b013e3181af59aa.

[55] H. Wunsch, W. T. Linde-Zwirble, D. C. Angus, M. E. Hartman, E. B. Milbrandt, and J. M. Kahn, "The epidemiology of mechanical ventilation use in the United States," *Critical Care Medicine*, vol. 38, no. 10, pp. 1947–1953, 2010, doi: 10.1097/CCM.0b013e3181ef4460.

[56] H. Wunsch, "Mechanical Ventilation in COVID-19: Interpreting the Current Epidemiology," *American Journal of Respiratory and Critical Care Medicine*, 2020, doi: 10.1164/rccm.202004-1385ed.

[57] A. B. Mehta, S. N. Syeda, R. S. Wiener, and A. J. Walkey, "Epidemiological trends in invasive mechanical ventilation in the United States: A population-based study," *Journal of Critical Care*, vol. 30, no. 6, pp. 1217–1221, 2015, doi: 10.1016/j.jcrc.2015.07.007.

[58] M. S. Herridge *et al.*, "The RECOVER program: Disability risk groups and 1-year outcome after 7 or more days of mechanical ventilation," *American Journal of Respiratory and Critical Care Medicine*, vol. 194, no. 7, pp. 831–844, 2016, doi: 10.1164/rccm.201512-2343OC.

[59] D. Adler, E. Dupuis-Lozeron, J. C. Richard, J. P. Janssens, and L. Brochard, "Does inspiratory muscle dysfunction predict readmission after intensive care unit discharge?," *American Journal of Respiratory and Critical Care Medicine*. 2014, doi: 10.1164/rccm.201404-0655LE.

[60] E. Damuth, J. A. Mitchell, J. L. Bartock, B. W. Roberts, and S. Trzeciak, "Long-term survival of critically ill patients treated with prolonged mechanical ventilation: A systematic review and meta-analysis," *The Lancet. Respiratory Medicine*, vol. 3, no. 7, pp. 544–553, 2015, doi: 10.1016/S2213-2600(15)00150-2.

[61] M. Dres and A. Demoule, "Diaphragm dysfunction during weaning from mechanical ventilation: an underestimated phenomenon with clinical implications," *Critical Care*, vol. 22, no. 1, p. 73, Dec. 2018, doi: 10.1186/s13054-018-1992-2.

[62] M. Dres *et al.*, "Coexistence and impact of limb muscle and diaphragm weakness at time of liberation from mechanical ventilation in medical intensive care unit patients," *American Journal of Respiratory and Critical Care Medicine*, vol. 195, no. 1, pp. 57–66, 2017, doi: 10.1164/rccm.201602-0367OC.

[63] M. Dres *et al.*, “Usefulness of Parasternal Intercostal Muscle Ultrasound during Weaning from Mechanical Ventilation,” *Anesthesiology*, pp. 1114–1125, 2020, doi: 10.1097/ALN.0000000000003191.

[64] E. C. Goligher *et al.*, “Diaphragmatic myotrauma: a mediator of prolonged ventilation and poor patient outcomes in acute respiratory failure,” *The Lancet Respiratory Medicine*, vol. 7, no. 1. pp. 90–98, 2019, doi: 10.1016/S2213-2600(18)30366-7.

[65] J. Batt, C. C. Dos Santos, J. I. Cameron, and M. S. Herridge, “Intensive care unit-acquired weakness clinical phenotypes and molecular mechanisms,” *American Journal of Respiratory and Critical Care Medicine*, vol. 187, no. 3, pp. 238–246, 2013, doi: 10.1164/rccm.201205-0954SO.

[66] M. Aubier, T. Trippenbach, and C. Roussos, “Respiratory muscle fatigue during cardiogenic shock,” *Journal of Applied Physiology. Respiratory Environmental and Exercise Physiology*, vol. 51, no. 2, pp. 499–508, 1981, doi: 10.1152/jappl.1981.51.2.499.

[67] S. Magder, “Bench-to-bedside review: ventilatory abnormalities in sepsis.,” *Critical Care*, vol. 13, no. 1. p. 202, 2009, doi: 10.1186/cc7116.

[68] B. Shadgan, J. A. Guenette, A. W. Sheel, and W. D. Reid, “Sternocleidomastoid muscle deoxygenation in response to incremental inspiratory threshold loading measured by near infrared spectroscopy,” *Respiratory Physiology and Neurobiology*, vol. 178, no. 2, pp. 202–209, 2011, doi: 10.1016/j.resp.2011.06.001.

[69] N. Basoudan, B. Shadgan, J. A. Guenette, J. Road, and W. D. Reid, “Effect of acute hypoxia on inspiratory muscle oxygenation during incremental inspiratory loading in healthy adults,” *European Journal of Applied Physiology*, vol. 116, no. 4, pp. 841–850, 2016, doi: 10.1007/s00421-016-3334-x.

[70] T. Tanaka *et al.*, “Deoxygenation of inspiratory muscles during cycling, hyperpnoea and loaded breathing in health and disease: a systematic review,” *Clinical Physiology and Functional Imaging*, vol. 38, no. 4, pp. 554–565, 2018, doi: 10.1111/cpf.12473.

[71] A. Rodrigues *et al.*, “Differences in Respiratory Muscle Responses to Hyperpnea or Loaded Breathing in COPD,” *Medicine and Science in Sports and Exercise*, vol. 52, no. 5, pp. 1126-1134, 2020, doi: 10.1249/MSS.0000000000002222.

[72] K. Katayama *et al.*, “Hypoxia exaggerates inspiratory accessory muscle deoxygenation during hyperpnoea,” *Respiratory Physiology and Neurobiology*, vol. 211, pp. 1–8, 2015, doi: 10.1016/j.resp.2015.02.005.

[73] P. B. Dominelli *et al.*, “Effects of respiratory muscle work on respiratory and locomotor blood flow during exercise,” *Experimental Physiology*, vol. 102, no. 11, pp. 1535–1547, 2017, doi: 10.1113/EP086566.

[74] L. F. Ferreira, D. M. Hueber, and T. J. Barstow, “Effects of assuming constant optical scattering on measurements of muscle oxygenation by near-infrared spectroscopy during exercise,” *Journal of Applied Physiology*, vol. 102, no. 1, pp. 358–367, 2007, doi: 10.1152/japplphysiol.00920.2005.

[75] S. M. Hammer *et al.*, “Effect of assuming constant tissue scattering on measured tissue oxygenation values during tissue ischemia and vascular reperfusion,” *Journal of Applied Physiology*, vol. 127, no. 1, pp. 22–30, 2019, doi: 10.1152/japplphysiol.01138.2018.

[76] A. E. Cerussi, V. W. Tanamai, R. S. Mehta, D. Hsiang, J. Butler, and B. J. Tromberg, “Frequent optical imaging during breast cancer neoadjuvant chemotherapy reveals dynamic tumor physiology in an individual patient,” *Academic Radiology*, vol. 17, no. 8, pp. 1031–1039, doi: S1076-6332(10)00254-0 [pii]10.1016/j.acra.2010.05.002.

[77] V. Quaresima *et al.*, “Diffuse correlation spectroscopy and frequency-domain near-infrared spectroscopy for measuring microvascular blood flow in dynamically exercising human muscles,” *Journal of Applied Physiology*, vol. 127, no. 5, pp. 1328–1337, 2019, doi: 10.1152/japplphysiol.00324.2019.

[78] M.-L. Chuang, I.-F. Lin, and M.-J. Hsieh, “More Impaired Dynamic Ventilatory Muscle Oxygenation in Congestive Heart Failure than in Chronic Obstructive Pulmonary Disease,” *Journal of Clinical Medicine*, vol. 8, no. 10, p. 1641, 2019, doi: 10.3390/jcm8101641.

[79] Q. Fang and D. A. Boas, “Monte Carlo Simulation of Photon Migration in 3D Turbid Media Accelerated by Graphics Processing Units,” *Optics Express*, vol. 17, no. 22, p. 20178, 2009, doi: 10.1364/oe.17.020178.

[80] M. J. C. Van Gemert, S. L. Jacques, M. Sterenborg, and W. M. Star, “Skin Optics,” *IEEE Transactions on Bio-medical Engineering*, vol. 36, no. 12, pp. 1146–1154, 1989.

[81] S. L. Jacques, “Erratum: Optical properties of biological tissues: A review (Physics in Medicine and Biology (2013) 58),” *Physics in Medicine and Biology*, vol. 58, no. 14, pp. 5007–5008, 2013, doi: 10.1088/0031-9155/58/14/5007.

[82] C. R. Simpson, M. Kohl, M. Essenpreis, and M. Cope, “Near-infrared optical properties of ex vivo human skin and subcutaneous tissues measured using the Monte Carlo inversion technique,” *Physics in Medicine and Biology*, vol. 43, no. 9,

pp. 2465–2478, 1998, doi: 10.1088/0031-9155/43/9/003.

[83] J. Lai, Z. Li, C. Wang, and A. He, “Experimental measurement of the refractive index of biological tissues by total internal reflection,” *Applied Optics*, vol. 44, no. 10, pp. 1845–1849, 2005, doi: 10.1364/AO.44.001845.

[84] J. C. Lai, Y. Y. Zhang, Z. H. Li, H. J. Jiang, and A. Z. He, “Complex refractive index measurement of biological tissues by attenuated total reflection ellipsometry,” *Applied Optics*, vol. 49, no. 16, pp. 3235–3238, 2010, doi: 10.1364/AO.49.003235.

[85] A. N. Bashkatov, E. A. Genina, and V. V. Tuchin, “Optical properties of skin, subcutaneous, and muscle tissues: A review,” *Journal of Innovative Optical Health Sciences*, vol. 4, no. 1, pp. 9–38, 2011, doi: 10.1142/S1793545811001319.

[86] A. N. Bashkatov, E. A. Genina, V. I. Kochubey, and V. V. Tuchin, “Optical properties of human skin, subcutaneous and mucous tissues in the wavelength range from 400 to 2000 nm,” *Journal of Physics D: Applied Physics*, vol. 38, no. 15, pp. 2543–2555, 2005, doi: 10.1088/0022-3727/38/15/004.

[87] I. Meglinski and A. Doronin, “Monte Carlo modeling of photon migration for the needs of biomedical optics and biophotonics,” in *Advanced Biophotonics: tissue optical sectioning*, 2013, pp. 1–58.

[88] G. Roggan, A., Dorschel, K., Minet, O., Wolff, D., Muller, “The optical properties of biological tissue in the near infrared wavelength range – review and measurments,” in *Laser-Induced Interstitial Thermotherapy, Institute series, Is13*, 1995.

[89] N. Bosschaart, G. J. Edelman, M. C. G. Aalders, T. G. Van Leeuwen, and D. J. Faber, “A literature review and novel theoretical approach on the optical properties of whole blood,” *Lasers in Medical Science*, vol. 29, no. 2, pp. 453–479, 2014, doi: 10.1007/s10103-013-1446-7.

[90] K. Chopra *et al.*, “A comprehensive examination of topographic thickness of skin in the human face,” *Aesthetic Surgery Journal*, vol. 35, no. 8, pp. 1007–1013, 2015, doi: 10.1093/asj/sjv079.

[91] H.-J. Lee and J.-M. Song, “Deep Neck Flexor and Sternocleidomastoid Muscle Thickness Change in Persons with No Current Neck Pain using Rehabilitative Ultrasonograpic Imaging,” *The Journal of Korean Physical Therapy*, vol. 28, no. 6, pp. 349–354, 2016, doi: 10.18857/jkpt.2016.28.6.349.

[92] B. S. Lin, C. W. Kong, D. C. Tarng, T. P. Huang, and G. J. Tang, “Anatomical variation of the internal jugular vein and its impact on temporary haemodialysis vascular access: An ultrasonographic survey in uraemic patients,” *Nephrology*

Dialysis Transplantation, vol. 13, no. 1, pp. 134–138, 1998, doi: 10.1093/ndt/13.1.134.

[93] W. G. Zijlstra, A. Buursma, and O. W. van Assendelft (eds.), *Visible and Near Infrared Absorption Spectra of Human and Animal Haemoglobin: Determination and Application*. Utrecht, Boston: VSP, 2000.

[94] G. Nishimura, I. Kida, and M. Tamura, "Characterization of optical parameters with a human forearm at the region from 1.15 to 1.52 μm using diffuse reflectance measurements," *Physics in Medicine and Biology*, vol. 51, no. 11, pp. 2997–3011, 2006, doi: 10.1088/0031-9155/51/11/021.

[95] P. Ballard, D. E. Leahy, and M. Rowland, "Prediction of in vivo tissue distribution from in vitro data 1. Experiments with markers of aqueous spaces," *Pharmaceutical Research*, vol. 17, no. 6, pp. 660–663, 2000, doi: 10.1023/A:1007565828856.

[96] L. Kou, D. Labrie, and P. Chylek, "Refractive indices of water and ice in the 065- to 25-μm spectral range," *Applied Optics*, vol. 32, no. 19, p. 3531, 1993, doi: 10.1364/ao.32.003531.

[97] M. B. Applegate and D. Roblyer, "Multi-distance diffuse optical spectroscopy with a single optode via hypotrochoidal scanning," *Optics Letters*, vol. 43, no. 4, p. 747, 2018, doi: 10.1364/OL.43.000747.

[98] A. Derbakova *et al.*, "Neck and Inspiratory Muscle Recruitment during Inspiratory Loading and Neck Flexion," *Medicine and Science in Sports and Exercise*, 2020, doi: 10.1249/MSS.0000000000002271.

[99] M. B. Applegate, C. A. Gómez, and D. Roblyer, "Modulation frequency selection and efficient look-up table inversion for frequency domain diffuse optical spectroscopy," *Journal of Biomedical Optics*, vol. 26, no. March, pp. 1–15, 2021, doi: 10.1117/1.JBO.26.3.036007.

[100] I. Heinonen, S. Koga, K. K. Kalliokoski, T. I. Musch, and D. C. Poole, "Heterogeneity of Muscle Blood Flow and Metabolism: Influence of Exercise, Aging, and Disease States," *Exercise and Sport Sciences Reviews*, 2015, doi: 10.1249/JES.0000000000000044.

[101] W. G. Murphy, "The sex difference in haemoglobin levels in adults - Mechanisms, causes, and consequences," *Blood Reviews*, vol. 28, no. 2, pp. 41–47, 2014, doi: 10.1016/j.blre.2013.12.003.

[102] H. M. Peterson *et al.*, "Characterization of bony anatomic regions in pediatric and adult healthy volunteers using diffuse optical spectroscopic imaging," *Journal of Biomedical Optics*, vol. 25, no. 08, p. 1, 2020, doi: 10.1117/1.jbo.25.8.086002.

[103] B. Chance, Q. Luo, S. Nioka, D. C. Alsop, and J. A. Detre, “Optical investigations of physiology: A study of intrinsic and extrinsic biomedical contrast,” *Philosophical Transactions of the Royal Society B: Biological Sciences*, 1997, doi: 10.1098/rstb.1997.0053.

[104] S. A. Carp, P. Farzam, N. Redes, D. M. Hueber, and M. A. Franceschini, “Combined multi-distance frequency domain and diffuse correlation spectroscopy system with simultaneous data acquisition and real-time analysis,” *Biomedical Optics Express*, vol. 8, no. 9, p. 3993, 2017, doi: 10.1364/boe.8.003993.

[105] D. Tamborini, P. Farzam, B. Zimmermann, K.-C. Wu, D. A. Boas, and M. A. Franceschini, “Development and characterization of a multidistance and multiwavelength diffuse correlation spectroscopy system,” *Neurophotonics*, vol. 5, no. 01, p. 1, 2017, doi: 10.1117/1.nph.5.1.011015.

[106] B. M. Quandt, L. J. Scherer, L. F. Boesel, M. Wolf, G. L. Bona, and R. M. Rossi, “Body-Monitoring and Health Supervision by Means of Optical Fiber-Based Sensing Systems in Medical Textiles,” *Advanced Healthcare Materials*, 2015, doi: 10.1002/adhm.201400463.

[107] J. Song, D. Li, X. Ma, G. Teng, and J. Wei, “A robust dynamic heart-rate detection algorithm framework during intense physical activities using photoplethysmographic signals,” *Sensors (Switzerland)*, 2017, doi: 10.3390/s17112450.

[108] J. Kim *et al.*, “Oximetry: Miniaturized Battery-Free Wireless Systems for Wearable Pulse Oximetry (Adv. Funct. Mater. 1/2017),” *Advanced Functional Materials*, 2017, doi: 10.1002/adfm.201770007.

[109] M. Kramer, A. Lobbestael, E. Barten, J. Eian, and G. Rausch, “Wearable pulse oximetry measurements on the torso, arms, and legs: A proof of concept,” *Military Medicine*, 2017, doi: 10.7205/MILMED-D-16-00129.

[110] A. Devor *et al.*, “Frontiers in optical imaging of cerebral blood flow and metabolism,” *Journal of Cerebral Blood Flow and Metabolism*. 2012, doi: 10.1038/jcbfm.2011.195.

[111] A. H. Hielscher *et al.*, “Frequency-domain optical tomographic imaging of arthritic finger joints,” *IEEE Transactions on Medical Imaging*, 2011, doi: 10.1109/TMI.2011.2135374.

[112] M. A. Khalil *et al.*, “Dynamic diffuse optical tomography imaging of peripheral arterial disease,” *Biomedical Optics Express*, 2012, doi: 10.1364/boe.3.002288.

[113] B. J. Tromberg *et al.*, “Non-invasive in vivo characterization of breast tumors using photon migration spectroscopy,” *Neoplasia*. 2000, doi: 10.1038/sj.neo.7900082.

[114] S. Ueda *et al.*, “Baseline tumor oxygen saturation correlates with a pathologic complete response in breast cancer patients undergoing neoadjuvant chemotherapy,” *Cancer Research*, 2012, doi: 10.1158/0008-5472.CAN-12-0056.

[115] B. Chance, M. Cope, E. Gratton, N. Ramanujam, and B. Tromberg, “Phase measurement of light absorption and scatter in human tissue,” *Review of Scientific Instruments*, 1998, doi: 10.1063/1.1149123.

[116] A. D. Mora *et al.*, “Towards next-generation time-domain diffuse optics for extreme depth penetration and sensitivity,” *Biomedical Optics Express*, vol. 6, no. 5, p. 1749, 2015, doi: 10.1364/BOE.6.001749.

[117] E. Sultan, L. Najafizadeh, A. H. Gandjbakhche, K. Pourrezaei, and A. Daryoush, “Accurate optical parameter extraction procedure for broadband near-infrared spectroscopy of brain matter,” *Journal of Biomedical Optics*, 2013, doi: 10.1117/1.jbo.18.1.017008.

[118] T. D. O’Sullivan, “Vertical-cavity surface-emitting laser sources for gigahertz-bandwidth, multiwavelength frequency-domain photon migration,” *Journal of Biomedical Optics*, 2017, doi: 10.1117/1.jbo.22.10.105001.

[119] F. Bevilacqua, A. J. Berger, A. E. Cerussi, D. Jakubowski, and B. J. Tromberg, “Broadband absorption spectroscopy in turbid media by combined frequency-domain and steady-state methods,” *Applied Optics*, vol. 39, no. 34, p. 6498, 2000, doi: 10.1364/ao.39.006498.

[120] H. S. Yazdi *et al.*, “Mapping breast cancer blood flow index, composition, and metabolism in a human subject using combined diffuse optical spectroscopic imaging and diffuse correlation spectroscopy,” *Journal of Biomedical Optics*, 2017, doi: 10.1117/1.jbo.22.4.045003.

[121] N. G. Chen, M. Huang, H. Xia, D. Piao, E. Cronin, and Q. Zhu, “Portable near-infrared diffusive light imager for breast cancer detection,” *Journal of Biomedical Optics*, 2004, doi: 10.1117/1.1695410.

[122] R. C. Haskell, L. O. Svaasand, T.-T. Tsay, T.-C. Feng, B. J. Tromberg, and M. S. McAdams, “Boundary conditions for the diffusion equation in radiative transfer,” *Journal of the Optical Society of America A*, 1994, doi: 10.1364/josaa.11.002727.

[123] T. D. O’Sullivan, “Vertical-cavity surface-emitting laser sources for gigahertz-bandwidth, multiwavelength frequency-domain photon migration,” *Journal of Biomedical Optics*, vol. 22, no. 10, p. 1, 2017, doi: 10.1117/1.jbo.22.10.105001.

[124] D. Chitnis *et al.*, “Towards a wearable near infrared spectroscopic probe for monitoring concentrations of multiple chromophores in biological tissue in vivo,” *Review of Scientific Instruments*, 2016, doi: 10.1063/1.4954722.

[125] M. L. Flexman, H. K. Kim, R. Stoll, M. A. Khalil, C. J. Fong, and A. H. Hielscher, “A wireless handheld probe with spectrally constrained evolution strategies for diffuse optical imaging of tissue,” *Review of Scientific Instruments*. 2012, doi: 10.1063/1.3694494.

[126] F. Teng *et al.*, “Wearable near-infrared optical probe for continuous monitoring during breast cancer neoadjuvant chemotherapy infusions,” *Journal of Biomedical Optics*, 2017, doi: 10.1117/1.jbo.22.1.014001.

[127] G. Hu, Q. Zhang, V. Ivkovic, and G. E. Strangman, “Ambulatory diffuse optical tomography and multimodality physiological monitoring system for muscle and exercise applications,” *Journal of Biomedical Optics*, 2016, doi: 10.1117/1.jbo.21.9.091314.

[128] B. B. Zimmermann and S. A. Carp, “Frequency domain near-infrared multiwavelength imager design using conversion,” *Journal of Biomedical Optics*, 2016, doi: 10.1117/1.JBO.21.1.016010.

[129] K.-S. No, R. Kwong, P. H. Chou, and A. Cerussi, “Design and testing of a miniature broadband frequency domain photon migration instrument,” *Journal of Biomedical Optics*, 2008, doi: 10.1117/1.2998473.

[130] C. C. Sthalekar and V. J. Koomson, “A CMOS sensor for measurement of cerebral optical coefficients using non-invasive frequency domain near infrared spectroscopy,” *IEEE Sensors Journal*, 2013, doi: 10.1109/JSEN.2013.2260651.

[131] C. C. Sthalekar, Y. Miao, and V. J. Koomson, “Optical Characterization of Tissue Phantoms Using a Silicon Integrated fdNIRS System on Chip,” *IEEE Transactions on Biomedical Circuits and Systems*, 2017, doi: 10.1109/TBCAS.2016.2586103.

CURRICULUM VITAE

Raeef E. Istfan
raeef@bu.edu | (617) 759-0513 | Brookline MA, 02446
Linked In: https://www.linkedin.com/in/raeef-istfan-836997b0

Education:

Boston University College of Engineering, Boston MA — Expected in May 2021
Doctor of Philosophy in Biomedical Engineering

Boston University College of Engineering, Boston MA — 2012
Bachelor of Science in Biomedical Engineering; Minor in Electrical Engineering; Concentration in Nanotechnology, *Summa Cum Laude*

Honors:

- Quantitative Biology and Physiology Training Fellowship — 2014–2015
- Tau Beta Pi Honor Society (Treasurer 2011- 2012)
- Alpha Eta Mu Beta Honor Society
- Boston University Undergraduate Research Opportunities Program (UROP) — 2011
- Eagle Scout — 2008

Publications:

1. Zhao, Y., Deng, Y., Bao, F., Peterson, H., **Istfan, R**., & Roblyer, D. (2018). Deep learning model for ultrafast multifrequency optical property extractions for spatial frequency domain imaging. *Optics letters*, *43*(22), 5669-5672.
2. Zhao, Y., Applegate, M. B., **Istfan, R**., Pande, A., & Roblyer, D. (2018). Quantitative real-time pulse oximetry with ultrafast frequency-domain diffuse optics and deep neural network processing. *Biomedical optics express*, *9*(12), 5997-6008.
3. Torjesen, A., **Istfan, R**. and Roblyer, D., 2017. Ultrafast wavelength multiplexed broad bandwidth digital diffuse optical spectroscopy for in vivo extraction of tissue optical properties. *Journal of Biomedical Optics*, *22*(3), pp.036009-036009.
4. Teng, F., Cormier, T., Sauer-Budge, A., Chaudhury, R., Pera, V., **Istfan, R**., Chargin, D., Brookfield, S., Ko, N.Y. and Roblyer, D.M., 2017. Wearable near-infrared optical probe for continuous monitoring during breast cancer neoadjuvant chemotherapy infusions. *Journal of biomedical optics*, *22*(1), pp.014001-014001.
5. Tabassum, S., Zhao, Y., **Istfan, R**., Wu, J., Waxman, D.J. and Roblyer, D., 2016. Feasibility of spatial frequency domain imaging (SFDI) for optically characterizing a preclinical oncology model. *Biomedical optics express*, *7*(10), pp.4154-4170.
6. Diep, P., Pannem, S., Sweer, J., Lo, J., Snyder, M., Stueber, G., Zhao, Y., Tabassum, S., **Istfan, R**., Wu, J. and Erramilli, S., 2015. Three-dimensional printed optical phantoms with customized absorption and scattering properties. *Biomedical optics express*, *6*(11), pp.4212-4220.
7. Greening, G.J., **Istfan, R**., Higgins, L.M., Balachandran, K., Roblyer, D., Pierce, M.C. and Muldoon, T.J., 2014. Characterization of thin poly (dimethylsiloxane)-based tissue-simulating phantoms with tunable reduced scattering and absorption coefficients at visible and near-infrared wavelengths. *Journal of biomedical optics*, *19*(11), pp.115002-115002.
8. Jung, J., **Istfan, R**. and Roblyer, D., 2014. Note: A simple broad bandwidth undersampling frequency-domain digital diffuse optical spectroscopy system. *Review of Scientific Instruments*, *85*(7), p.076108.

Posters/Presentations:

1. **R. Istfan**, M. Applegate C Gomez, A Pande, D. Roblyer, "*Non-invasive estimation of arterial and venous oxygen saturation using ultra-fast frequency-domain oximetry (UFO),"* SPIE Photonics West, Proc. SPIE 11215-23, Diagnostic and Therapeutic Application of Light in Cardiology 2020, February 2, 2020.
2. **Istfan, R**., LaRochelle, S., Chaudury, R., & Roblyer, D. (2019, March). A miniature frequency domain diffuse optical optode for quantitative wearable oximetry. In *Optical Tomography and Spectroscopy of Tissue XIII* (Vol. 10874, p. 108742B). International Society for Optics and Photonics.
3. **Istfan, R.,** Torjesen, A., Chaudhury, R., Roblyer, D. "A Wearable and Ultrafast Diffuse Optical Spectroscopic Imaging System"
4. **Istfan, R.**, A'amar, O., and Bigio, I., "Analysis of Mechanical Properties of Individual Cells Using Acoustical-optical Methods" (Poster presentation at the BMES conference in 2011)

Research Experience:

Graduate Research Assistant 2015–Present
Biomedical Optical Technologies Lab, Boston University, Boston

- Contributed to a variety of projects utilizing the lab's custom designed digital Diffuse Optical Spectroscopy System (dDOS) and miniaturized and tested several iterations of the system
- Investigated smaller light sources and detectors for our dDOS system
- Investigated various methods of extracting venous oxygenation saturation non-invasively using dDOS
- Ran simulations using Monte Carlo Extreme to model the light propagation in the neck
- Designed and conducted a study on healthy volunteers to measure the oxygenation of the Strenocleidomastoid muscle in the neck

Research Assistant 2012–2014
Biomedical Optical Technologies Lab, Boston University, Boston

- Helped start up the lab by fabricating and programming the major equipment and instrumentation for the group
- Took test images on tissue phantoms
- Conducted a mouse study using Spatial Frequency Domain Imaging (SFDI)
- Mentored undergraduate students by helping them get used to the equipment in the lab

Undergraduate Research Assistant Summers 2009–2011
Biomedical Optics Lab, Boston University, Boston

- Designed new stainless nozzle for use in an optical-acoustical device
- Ran tests using polystyrene spheres to test nozzle implementation in device
- Presented summer research as a poster presentation at the BMES conference in October 2011

Volunteer Experience:

Boston University OSA/SPIE Student Chapter 2017–Present
Boston University, Boston

- Vice Present (2017-2020)
- Helped plan the chapter's events including the Boston Photonics Conference that we hosted in 2018 as well as various socials and student seminars
- Volunteered at various events around Boston showing off optics demos to children

Student Association of Graduate Engineers (SAGE) 2015–Present
Boston University, Boston

- Biomedical Engineering Representative (2015-2020)
- Helped organize and plan various events including our yearly 120-person ski trip (5 years), beach trip, and red sox games

Volunteer 2013–2014
New England Baptist Hospital, Boston

- Helped out in a Nursing Floor 4 West
- Helped Nurses, responded to phone calls, discharged patients

Skills:
Languages: fluent in English, Levantine Arabic, a little bit of Spanish
Computer Languages: Matlab, Labview, a little bit of C++
Lab Skills: IR spectroscopy, ECG, Oscilloscope, Function Generator, Network Analyzer, Soldering, ImageJ, Silicone Phantoms, Solidworks, 3D Printing